UNIVERSIDADE DO ESTADO DE SANTA CATARINA – UDESC
CENTRO DE CIÊNCIAS TECNOLÓGICAS – CCT
PROGRAMA DE PÓS GRADUAÇÃO EM ENGENHARIA ELÉTRICA – PPGEEL

RAFAEL JULIANO SCHOLTZ

DATA-DRIVEN CONTROL APPLIED TO SINGLE-PHASE HIGH POWER FACTOR BOOST RECTIFIERS

JOINVILLE
2025

UNIVERSIDADE DO ESTADO DE SANTA CATARINA – UDESC
CENTRO DE CIÊNCIAS TECNOLÓGICAS – CCT
PROGRAMA DE PÓS GRADUAÇÃO EM ENGENHARIA ELÉTRICA – PPGEEL

RAFAEL JULIANO SCHOLTZ

CONTROLE BASEADO EM DADOS APLICADO A RETIFICADORES BOOST MONOFÁSICOS COM ELEVADO FATOR DE POTÊNCIA

JOINVILLE
2025

RAFAEL JULIANO SCHOLTZ

DATA-DRIVEN CONTROL APPLIED TO SINGLE-PHASE HIGH POWER FACTOR BOOST RECTIFIERS

Master's thesis presented to the Graduate Program in Electrical Engineering of the Santa Catarina State University, as a requirement for the obtention of the title of Master in Electrical Engineering, concentration area of Electronic Systems.

Supervisor: Prof. Yales Rômulo de Novaes, Dr.
Co-supervisor: Chrystian Lenon Remes, Dr.

Joinville

2025

Ficha catalográfica elaborada pelo programa de geração automática da

Biblioteca Universitária Udesc,

com os dados fornecidos pelo(a) autor(a)

Scholtz, Rafael Juliano
Data-Driven Control Applied to Single-Phase High Power Factor Boost Rectifiers / Rafael Juliano Scholtz. -- 2025.
87 p.

Orientador: Yales Rômulo de Novaes
Coorientador: Chrystian Lenon Remes
Dissertação (mestrado) -- Universidade do Estado de Santa Catarina, Centro de Ciências Tecnológicas, Programa de Pós-Graduação em Engenharia Elétrica, Joinville, 2025.

1. Data-driven control. 2. Power electronics. 3. Power Factor Correction. 4. High Power Factor Rectifier. I. Novaes, Yales Rômulo de. II. Remes, Chrystian Lenon. III. Universidade do Estado de Santa Catarina, Centro de Ciências Tecnológicas, Programa de Pós-Graduação em Engenharia Elétrica. IV. Titulo.

RAFAEL JULIANO SCHOLTZ

DATA-DRIVEN CONTROL APPLIED TO SINGLE-PHASE HIGH POWER FACTOR BOOST RECTIFIERS

Master's thesis presented to the Graduate Program in Electrical Engineering of the Santa Catarina State University, as a requirement for the obtention of the title of Master in Electrical Engineering, concentration area of Electronic Systems.
Supervisor: Prof. Yales Rômulo de Novaes, Dr.
Co-supervisor: Chrystian Lenon Remes, Dr.

EXAMINATION BOARD

Prof. Yales Rômulo de Novaes, Dr.
Santa Catarina University State (UDESC) –
Board's president / Supervisor

Members:

Prof. Aurelio Tergolina Salton, Dr.
Federal University of Rio Grande do Sul
(UFRGS)

Felipe Joel Zimann, Dr.
Santa Catarina University State (UDESC)

Joinville, 19th November, 2025

ACKNOWLEDGEMENTS

First, I thank UDESC, CAPES and FAPESC for the financial support that enabled the continuity of this research.

I thank all the professors of NPEE and from UDESC master's program, for every class and opportunity to learn that was given to me.

I also thank my lab colleagues who made every day of research a tiny bit easier. A special thanks to: Lucas Costacurta Zuchi, Lucas Bona Ruckl, Erick Kupas, Henrique Thomaselli Teichert, Paulo Alves Feller, Paulo Roberto Pereira Junior, Luan Souza de Oliveira and Vitória Martins Michels.

A huge thanks to my personal friends for being who you are.

I'm specially grateful to my family for supporting me in the path I chose.

Finally, I am deeply grateful to my supervisors Yales Rômulo de Novaes and Chrystian Lenon Remes, for all the knowledge, discussions and critique shared with me during the time of this work. I hope we can continue to collaborate in both scientific research and friendship in the future.

ABSTRACT

This thesis presents a data-driven method to tune a cascade structure designed to control rectifiers of the boost power factor correction family. While data-driven control has already been explored in the context of DC-DC converters, it's proposed to utilize the Virtual Reference Feedback Tuning technique to design controllers for this family of rectifiers. In this way, it's possible to control the converter without the process of obtaining its exact model, simplifying the design. Guidelines concerning the data-collection, choice of reference models and controller classes are given. By separating the design of both internal and external control loops, two experiments are required to derive the required controllers, which comes as a cost in order to adapt the method to this linear time varying case. Furthermore, stability guarantees are given in case the external loop reference model is tuned to a bandwidth lower than the electric grid frequency. The proposed method is validated through both simulation and through experimental results with a 300 W prototype, and a quantitative comparison shows that it's superior to other classic model-based design techniques considering robustness and performance. Moreover, simulations with additive gaussian white noise in the current measurements show that the proposed method returns unbiased controller gains as noise power increases, demonstrating that the proposed method's estimation process is consistent.

Keywords: Data-driven control. Power electronics. Power Factor Correction. High power factor rectifier.

RESUMO

Esta dissertação apresenta um método baseado em dados para sintonizar uma estrutura em cascata projetada para controlar retificadores para correção ativa do fator de potência dentro da família de conversores Boost. Embora o controle baseado em dados já tenha sido explorado no contexto de conversores CC-CC, propõe-se utilizar a técnica de Ajuste de Realimentação por Referência Virtual para calcular controladores lineares para esta família de retificadores. Dessa maneira, é possível controlar o conversor sem passar pelo processo de obter seu modelo exato, facilitando o projeto. Diretrizes relativas à coleta de dados, escolha de modelos de referência e classes de controladores são sugeridas. Ao separar o projeto das malhas de controle interna e externa, dois experimentos são necessários para retornar os controladores necessários, o que representa um compromisso entre o número de experimentos exigido e a adaptação do método a este caso linear variante no tempo. Além disso, garantias de estabilidade são fornecidas caso o modelo de referência da malha externa seja sintonizado para uma largura de banda inferior à frequência da rede elétrica. O método proposto é validado por meio de simulação e experimentalmente com um protótipo de 300 W, tal que uma comparação quantitativa mostra que ele é superior a outras técnicas clássicas de projeto baseadas em modelo, considerando robustez e desempenho. Além disso, simulações com ruído branco gaussiano aditivo nas medições de corrente mostram que o design proposto retorna ganhos de controlador não-polarizados à medida que a potência do ruído aumenta, demonstrando que o processo de estimativa dos ganhos do projeto apresentado é consistente.

Palavras-chave: Controle baseado em dados. Eletrônica de potência. Correção do fator de potência. Retificador com elevado fator de potência.

LIST OF FIGURES

LIST OF TABLES

LIST OF ABBREVIATIONS AND ACRONYMS

AC	Alternate Current
AI	Artificial Intelligence
CBT	Correlation Based Tuning
CCM	Continuous Conduction Mode
CPL	Constant Power Load
DC	Direct Current
DDC	Data-Driven Control
DeePC	Data Enabled Model Predictive Control
DD-LQR	Data-Driven Linear Quadratic Regulator
DD-MPC	Data-Driven Model Predictive Control
EMC	Electromagnetic Compatibility
GM	Gain Margin
IV	Instrumental Variable
LMI	Linear Matrix Inequality
LPF	Low Pass Filter
LPV	Linear Parameter Varying
LTV	Linear Time Varying
MA	Moving Average
MCU	Microcontroller Unit
MFAC	Model Free Adaptive Control
MIMO	Multiple-Input Multiple-Output
MMC	Modular Multilevel Converter
MR	Model Reference
MRC	Model Reference Control
NN	Neural Network

PF	Power Factor
PFC	Power Factor Correction
PI	Proportional Integral
PLL	Phase Locked Loop
PM	Phase Margin
PPD	Pseudo Partial Derivative
PRBS	Pseudo-Random Binary Signal
PWM	Pulse Width Modulation
QMI	Quadratic Matrix Inequality
RL	Reinforcement Learning
RMS	Root Mean Square
SISO	Single-Input Single-Output
SNR	Signal to Noise Ratio
UPS	Uninterruptible Power Supply
VRFT	Virtual Reference Feedback Tuning

LIST OF SYMBOLS

f	Frequency
$G(z)$	Transfer function of a discretized process
$C(z)$	Transfer function of a controller
$C_i(z)$	Transfer function of the internal controller
$C_e(z)$	Transfer function of the external controller
$T(z)$	Closed-loop transfer function
$S(z)$	Sensitivity transfer function
$S_{di}(z)$	Associated internal sensitivity transfer function
$S_{de}(z)$	Associated external sensitivity transfer function
$\|\| \cdot \|\|$	Norm operator
$C_d(z)$	Ideal controller
$T_d(z)$	Reference model
$T_{di}(z)$	Internal reference model
$T_{de}(z)$	External reference model
J^{VR}	VRFT cost function
J^{MR}	MR cost function
J_r	Quadratic error cost function
$\mathscr{C}$	Controller class
ρ	Gains of a linearly parametrized controller
ρ_i	Gains of the internal controller
ρ_e	Gains of the external controller
$L(z)$	VRFT filter for controller class mismatch
$x_L(k)$	Signal $x(k)$ filtered by $L(z)$
$\bar{e}(k)$	Virtual error
$\phi_x(e^{j\Omega})$	Power spectrum of the signal $x(k)$

$r(k)$	Reference signal
$u(k)$	Plant input signal
$y(k)$	Plant output signal
$u_i(k)$	Internal control action
$u_e(k)$	External control action
$y_i(k)$	Internal output
$y_e(k)$	External output
$x^*(k)$	Nominal trajectory of the signal $x(k)$
$\Delta x(k)$	Variation around nominal trajectory of the signal $x(k)$
i_{in}	Input current
v_{in}	Input voltage
v_o	Output voltage
i_L	Inductor's current
d	Duty-cycle
L_b	Boost rectifier's inductor
C_o	Output capacitor
R_o	Output resistive load
P_o	Output power

CONTENTS

1 INTRODUCTION

In many real-world systems, a considerable amount of time and effort is spent modeling the process to synthesize a controller and operate in closed loop. As such, simplifications are often made to enable or facilitate modeling, but these can compromise system performance and robustness in some cases (Skogestad; Postlethwaite, 2005). Moreover, the stochastic nature of some systems may directly motivate the use of Data-Driven Control (DDC) techniques. For example, in the context of an increasingly power electronics dominated world, any converter which has to interface with the power grid in a closed-loop manner has to deal with its intrinsic uncertainty (Markovsky; Huang; Dörfler, 2023). In face of these difficulties, DDC methods seem to be an interesting alternative to model-based ones for applications in the control of power converters.

First, regarding the area of DC-DC converters, DDC has already been applied to the fundamental topologies in a plethora of works (Kameya et al., 2022; Qie et al., 2024; Ruiz-Martinez et al., 2020). In these cases, although the true behavior of the system is nonlinear (Kazimierczuk, 2015), a linear representation of the system can be extrapolated from the deviations of relevant signals around a known constant level. Consequently, DDC techniques can employ these signals, e.g., voltages and currents, to design linear controllers to regulate the system. Nonlinear control methods, such as Reinforcement Learning (RL), are also a topic of study, however there is an inherent disadvantage regarding the stability analysis in these cases, as they are much more complex to realize, therefore making the task of obtaining robust stability and performance much more complex (Recht, 2019). Among the linear techniques, the Virtual Reference Feedback Tuning (VRFT) deserves attention, since it's a one-shot technique, i.e., it only requires a single batch of input-output data to function. This reduces the hardware requirements and facilitates the conduction of a data-collection experiment, which is required to run the algorithm (Bazanella; Campestrini; Eckhard, 2011). Moreover, the simplicity in its formulation simplifies the task of studying the stability properties when applying it to a plant.

While VRFT has already been a topic of study in DC-DC converters, there is a noticeable gap in the literature around converters with large signal variation. An example of that are active Power Factor Correction (PFC) rectifiers, whose input currents are controlled to follow a sinusoidal trajectory (Friedli; Hartmann; Kolar, 2014), and thus don't present variations around a constant value. As Electromagnetic Compatibility (EMC) standards get increasingly restrictive, the use of PFC stages in power electronics in general is expected to rise in the future, specially in applications such as electric vehicles' chargers (Li et al., 2020), LED drivers (Castro et al., 2019), among others.

In order to start applying VFRT to PFC rectifiers, the simplest family of converters to begin with is the boost PFC one, since the boost topologies act similarly to a current source in the Continuous Conduction Mode (CCM), which relaxes the nonlinearities around the input

current's dynamics (Erickson; Maksimovic, 2020). Other topologies, such as the buck-boost, SEPIC, Ćuk, present a much strongly nonlinear behavior of the input current, and thus may require a more extensive analysis using nonlinear time-varying methods. Thus, this work focuses on the boost PFC family of rectifiers operating in CCM solely. Although this group presents several topologies, for instance the bridgeless or totem-pole variations (Huang; Huang, 2017; Cheng et al., 2015), all of them share the main boost dynamics, hence the proposed DDC design in this work may be applied to any of these converters.

In short, the general objective of this thesis is the proposal of a DDC design procedure using VRFT, which is able to return controllers that can manage to drive a boost PFC rectifier in CCM. Moreover, the related minor objectives are:

- The proposal of a method for conducting a data-collection experiment in order to enable VRFT;
- An analysis to determine the "worst-case" operating point of the converter to guarantee stability against certain parameter variations;
- Application of the proposed method in both simulated and experimental settings, in order to validate its effectiveness.

This work is organized as follows. In Chapter II a literature review of DDC techniques applied to power electronics is presented, and the VRFT design method is also described. Chapter III briefly introduces the totem-pole boost bridgeless PFC rectifier, which is the particular boost topology that is simulated and experimented in this thesis. Some PFC concepts and standards, which are utilized as a metric for comparison, are also introduced. Chapter IV contains the main results of this work, where VRFT is particularized to the boost PFC converter family with a cascade control structure. In sequence, Chapter V presents a simulation example and also explores the inner subsystem's controller calculation with noisy current data. Next, Chapter VI contains experimental results. Finally, Chapter VII concludes this thesis.

2 LITERATURE REVIEW

This chapter outlines DDC methods which have been applied to power electronics in the literature. A short description and a systematic review is presented.

2.1 DATA-DRIVEN CONTROL

In recent years a lot of attention has been given to the development and application of DDC techniques in the area of power electronics (Dörfler, 2023a,b). Power systems, for instance, are specially prominent cases of application, since it's very difficult to model the interactions between generators, power converters and the grid, but it's much more feasible to derive a control policy from input-output data instead (Markovsky; Huang; Dörfler, 2023). The same logic can be applied to the control strategy for DC-DC converters, which must reject disturbances in the input voltage and output load and thus work properly at a wide range of operating conditions. Model-based techniques often deal with this issue by considering these variations as parametric uncertainty, which is then leveraged in certain robust control analysis techniques, for instance, through the use of Linear Matrix Inequalities (LMIs) (Boyd et al., 1994). However, for simpler control design techniques, this often results in several iterations in the design process. On the other hand, DDC techniques are able to address more accurately the true operating conditions of the process, since this information is contained in the collected data. Accordingly, the use of stability and performance analysis techniques considering both parametric and unmodelled uncertainty can be less conservative. Moreover, many DDC techniques also incorporate and guarantee robustness given certain conditions, although this is still a topic of research in the literature.

Regarding the classification of DDC methods, the following criteria are considered (Prag; Woolway; Celik, 2022):

- Use of a fixed control structure;
- Use of Neural Networks (NNs);
- Direct or indirect methods.

In this last category, direct means that no model for the process is estimated in the controller design, whereas indirect is the opposite (Prag; Woolway; Celik, 2022). Some examples of data-driven control methods are: Virtual Reference Feedback Tuning (VRFT), Correlation Based Tuning (CBT) (Bazanella; Campestrini; Eckhard, 2011), Data-Driven Linear Quadratic Regulator (DD-LQR) (Silva et al., 2019), Reinforcement Learning (RL) (Recht, 2019), including others.

As it can be argued that the uncertainty of a model is contained within the operational data of the real process, data-driven techniques are often utilized as a way to directly mitigate

this uncertainty, while also providing systematic ways to design a controller (Prag; Woolway; Celik, 2022). In order to review how each technique addresses the controller design process, a classification of some DDC methods found in the literature that were used to control power converters is shown in Figure 1. In this master's thesis, the control problem is focused on the tracking and regulation for a single converter, so applications in the area of power systems, e.g., the control of several converters in a micro-grid, are not considered. This section presents a review of the main DDC methods present in the literature.

The verified methods can be divided globally in two groups, as shown in Figure 1. The first revolves around classical methods, which are given this name since they have become popular methods of DDC in many areas and have a solid mathematical theory in their formulations, often involving conditions for robust stability and performance (Bazanella; Campestrini; Eckhard, 2023; Yin et al., 2015; Hou; Wang, 2013).

The second main group, regarding Artificial Intelligence (AI) methods, has become more popular in recent years and is currently being studied or integrated into other techniques (Chen et al., 2023). However, methods in this group often lack the theoretical background for many important results like stability.

Within the classical methods, there is also a distinction between direct methods, which are able to return a controller without estimating a model for the process, and indirect methods that depend on an estimated model. This model can then be either linear, where all the model-based classical methods are applicable, or nonlinear and serve as a base for more complex techniques, for example Data-Driven Model Predictive Control (DD-MPC), which has multiple formulations that are either direct or indirect. Lastly, direct classical methods were divided into parameter-tuning and adaptive control. The former is based in the estimation of an optimal controller given a certain criterion and a fixed-structure - thus the method only estimates the optimal parameters related to the specified feedback law, e.g., the gains of a Proportional Integral (PI) controller. The latter concerns itself with formulating a local model for the plant based on online data and estimating a control law from it (Hou; Chi; Gao, 2017). The Model Free Adaptive Control (MFAC) is an example technique in this group. Examples of parameter tuning techniques are: VRFT, CBT, DD-LQR and behavioral theory.

In the literature, there are several examples of DDC methods applied to the control of power converters. Remes et al. (2021) studied the classic VRFT for the application in classic DC-DC converter topologies. Some guidelines were proposed and experimental results with a boost converter verified the effectiveness of the method. Additionally, Beal et al. (2023) have also utilized VRFT in order to generate an AC output voltage of an Uninterruptible Power Supply (UPS). A cascade control structure for current and voltage control was proposed, where a proportional gain in the feedback path of the current loop and a proportional-resonant controller for the voltage loop were fixed. Some simulation results indicate that tracking and harmonic rejection in the presence of non-linear loads were successfully achieved. Regarding DD-LQR, the

Figure 1 – Tree diagram of DDC techniques utilized in power electronics.

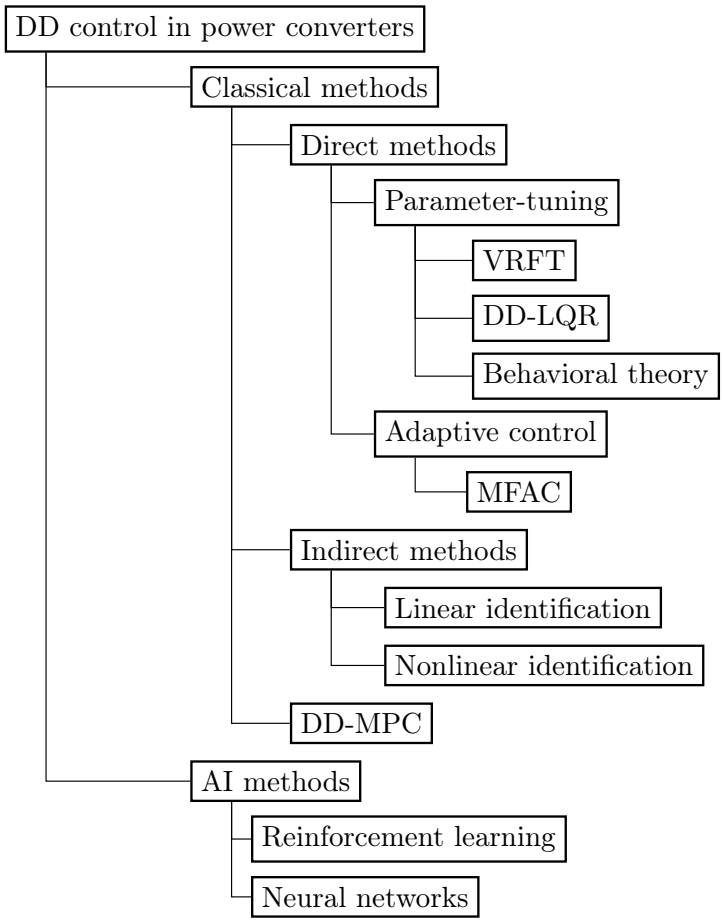

Source: adapted from Prag, Woolway, and Celik (2022).

same UPS application is studied by Silva et al. (2019), and experimental results have proved the practical applicability of this approach. A summary of DDC papers applied to power electronics is found in Table 1. Each DDC technique is discussed as follows.

2.1.1 VRFT

In the industrial fields, VRFT has received a lot of attention and has become one of the most popular direct DDC techniques (Bazanella; Campestrini; Eckhard, 2023). One of its most attractive advantages is the fact that it's a one-shot method, i.e., only one experiment is required to collect data and return a controller (Bazanella; Campestrini; Eckhard, 2011). The experiment can then be realized in an open-loop fashion or in a closed-loop with a stabilizing or already existing controller. There are both Single-Input Single-Output (SISO) and Multiple-Input Multiple-Output (MIMO) formulations, but only the SISO approach is discussed here for simplicity. In cascade structures, additional measurements for each controlled signal must also be made (Remes et al., 2020).

As a data-driven solution of the Model Reference Control (MRC) problem, VRFT requires a desired transfer function model for the plant $T_d(z)$. This desired model should follow

Table 1 – Summary of surveyed DDC methods in power converters.

Title	Converter topology	Method
VRFT for Current-Mode Buck Converter with Anti-Windup Compensation (Kameya et al., 2022)	Buck	VRFT
Virtual reference feedback tuning applied to cascade control (Remes et al., 2020)	SEPIC, zeta-buck-boost	VRFT
Virtual Reference Feedback Tuning Applied to DC–DC Converters (Remes et al., 2021)	Boost	VRFT
Harmonic Rejection on UPS through Cascade VRFT of Proportional-Resonant Controller (Beal et al., 2023)	Half-bridge	VRFT
A Novel Data-Driven Large Signal Stabilizer for Interleaved DC/DC Boost Converter With Constant Power Load (Qie et al., 2024)	Interleaved boost	DD-LQR
Data-Driven LQR Control Design (Silva et al., 2019)	Half-bridge	DD-LQR
Data-driven stabilizing control of DC-DC converters with unknown active loads (Ruiz-Martinez et al., 2020)	Boost	Behavioral
Data-Driven Tracking Control Design With Noisy Data and its Application in DC Microgrid Control (Wei et al., 2025)	SEPIC, buck, boost	Behavioral
Data-Driven Control for Interlinked AC/DC Microgrids Via Model-Free Adaptive Control and Dual-Droop Control (Zhang et al., 2017)	3ϕ inverter	MFAC
Model-free adaptive control for ultracapacitor based three-phase interleaved bidirectional DC-DC converter (Wang et al., 2023)	Interleaved boost	MFAC
Data-Driven Model-Free Adaptive Control of Z-Source Inverters (Asadi et al., 2021)	Z-source inverter	MFAC
Robust Data-Enabled Predictive Control: Tractable Formulations and Performance Guarantees (Huang et al., 2023)	3ϕ inverter	DD-MPC

Source: the author (2025).

some guidelines and it should be realistically obtainable. Then, with both the set of input-output data $\{u(k), y(k)\}_{k=1}^{N}$ and the reference model, VRFT aims to minimize the cost function

$$J^{VR}(\rho) = \sum_{k=1}^{N} \|L(z)[u(k) - C(z,\rho)\bar{e}(k)]\|_2^2, \tag{2.1}$$

where $L(z)$ is a weighting filter, ρ is the controller coefficients that need to be estimated, $C(z,\rho)$ is a fixed-structure controller that is linear in ρ and $\bar{e}(k)$ is the virtual error given by $\bar{e}(k) = (T_d^{-1}(z) - 1)y(k)$. This in turn is equivalent to an identification problem and can then be solved by the classic least-squares method.

The classical VRFT method has some limitations and some variations of the method have already been proposed. For more details, see (Bazanella; Campestrini; Eckhard, 2011). One of the major disadvantages is the lack of consideration in the base methods for stability and robustness, since there is no guarantee that a stabilizing controller is returned. A recent paper has also approached this problem by employing AI solutions and impulse response estimations (Fiorio et al., 2021).

Some recent papers have explored VRFT to directly control a power converter: Remes et al. (2021) presented a guide of how to apply the method for classical DC-DC converters. Additionally, some guidelines for the choice of reference model and filter $L(z)$ were given. The method was also employed in an actual experiment to control a boost converter, where a

comparison to classic model-based approaches was made. In that paper, it was shown that the method is feasible and can provide superior performance for reference tracking than model-based frequency shaping methods. Moreover, Remes et al. (2020) have also studied the adaptation of the classical VRFT to a cascade control structure. Two cascade controller topologies were analyzed, and a filter was derived for each case in order to improve the VRFT method. A simulation example of a 4th order plant representative of a SEPIC or a zeta-buck-boost converter was presented, where additional disturbance rejection was established with the cascade structure, albeit with the corresponding requirement of an additional current measurement.

VRFT has also been applied to other topologies like half-bridge inverter in Beal et al. (2023), where one of the cascade structures from Remes et al. (2020) was applied to the control of a UPS. A fixed-structure given by a proportional-resonant controller with set frequencies was proposed. The resonant frequencies were placed at the fundamental and some of its harmonics, considering the UPS output voltage signal. Simulated results have indicated improvement in harmonic rejection up to the 15th order because of the additional terms in the controller.

Finally, a recent paper (Kameya et al., 2022) has applied VRFT to tune the controller parameters of a current-mode buck converter with anti-windup compensation. By structuring the controller linearly, it was still possible to use the least squares technique to calculate the optimal controller that includes 4 parameters to be tuned: proportional-integral coefficients for the error in output voltage; and proportional for current and anti-windup terms. A comparison with the standard VRFT with an empiric setting for the anti-windup gain has shown that including this extra term in the VRFT formulation can further optimize the process, resulting in a slightly better settling time. Altogether, the inclusion of some nonlinear control laws in VRFT is still a study topic and shows potential to improve dynamic performance, although stability analysis is more complex.

2.1.2 DD-LQR

In discrete form, the LQR problem aims to minimize the quadratic cost

$$J = \sum_{k=0}^{\infty} x^T(k)Qx(k) + u^T(k)Ru(k), \tag{2.2}$$

where R is positive definite and Q is positive semidefinite (Van Waarde et al., 2023). For a linear known process model, there is a unique solution determined by the control law $u = K_{\text{opt}}x$, where K_{opt} can be computed from the state matrices from the model.

Following the data-driven methodology, the DD-LQR problem consists of estimating the optimal feedback gain $\hat{K}_{opt}$ directly from the states' data. In the literature, there are some publications that address this. In Silva et al. (2019) a direct formulation based on the Markov parameters from the subspace representation of the system is proposed. Here the controller is determined as a function of a Toeplitz matrix representing the forced dynamics of the system and an extended observability matrix, which is derived from two proposed algorithms. Both

have distinct advantages: the first results in a smaller bias whereas the second implies a smaller variance for the observability matrix terms. All the estimations can be made offline and are based on the least-squares formulation, resulting in desirable properties. The proposed strategy is put to test in a UPS application with the half-bridge topology. Additional stress was tested with the use of a Constant Power Load (CPL). The results indicate that the purely data-driven approach has similar results to a robust control design based on LMIs. Moreover, the controller still performs well under no-load or linear nominal load situations, implying robust performance of the method. Another approach was proposed in Qie et al. (2024) for an online policy-iteration on the feedback DD-LQR gains. In this regard, an algorithm iteratively updates the optimal solution matrix of the LQR problem based on operation data. The algorithm assumes a certain knowledge of the plant model to be initialized. For stability and convergence, a rigorous proof is given and, in order to alleviate the computational burden of the online process, recurrent neural networks are utilized to approximate some matrix operations. A benchmark in an interleaved boost converter is presented and robust performance is obtained in the presence of a CPL under both continuous and discontinuous conduction modes.

Both discussed methodologies manage to derive a DD-LQR control law and share two common flaws: i) Lack of formal prior analysis for robust stability based on the collected data; ii) Requirement to measure all the system's states. With this in mind, some attention has been given in the literature to the derivation of some conditions for data informativity, i.e., formal conditions for a global common existence of a stabilizing proposed control law given a set of data (Van Waarde et al., 2023; Persis; Tesi, 2020). Accordingly, it would be interesting to apply these conditions in the control design problem for power converters and see whether they are overly conservative or applicable, given the nonlinearities that are present. It's also interesting to use those frameworks as a base for formal informativity derivations when proposing more complex control laws, for instance switched control or Linear Parameter Varying (LPV) control.

2.1.3 Behavioral theory

The base of behavioral theory states that for linear systems, all the possible state trajectories can be derived by a finite set of data, as long as this set comes from sufficiently excited dynamics (Willems et al., 2005). Consequently, a stabilizing controller can be directly formulated from collected data.

This idea is explored by Ruiz-Martinez et al. (2020) for the control of a boost converter feeding a constant power load by finding the matrices of a controller in state-space form. To do this, an algorithm in the form of LMIs was applied to multiple points of operation of the system, resulting in multiple stabilizing controllers. However, the control problem here only searches a stabilizing controller, without optimizing any function, which could be further explored.

Moreover, recent research in this area explores direct synthetization of linear controllers through a framework using Quadratic Matrix Inequalities (QMIs) in its mathematical formulation

(Van Waarde et al., 2023). In that regard, instead of aiming for a controller which optimizes a certain performance metric to the most likely system represented by the data, these methods often aim to derive controllers which stabilize every system inside a set that is consistent with the data. This suggests that robust stability could already be guaranteed by the method if certain hypothesis in each formulation are correct, but more research must be made to assess this with certainty.

Although this is quite a recent approach to data-driven control, Wei et al. (2025) have explored this area to derive state-feedback controllers for several topologies in a microgrid minimizing an $\mathscr{H}_\infty$ performance metric. In this paper, two experiments are required, one to tune the internal controllers for current control and another to tune the outer droop control gains. Successful stability results under voltage and load disturbances validate the proposed method.

2.1.4 MFAC

Model free adaptive control is based on the dynamic linearization concept, which is capable of determining an equivalent representation of a nonlinear process at each operation point, purely by utilizing input/output data (Hou; Chi; Gao, 2017). On this matter, the compact-form dynamic linearization of the process can be expressed by

$$y(k+1) = y(k) + \phi(k)\Delta u(k), \tag{2.3}$$

where $\phi(k)$ is the Pseudo Partial Derivative (PPD) of the controlled system. This linear model can then be easily used to compute a control action based on any performance criterion. Multiple methods for estimation the PPD can be utilized.

For power electronics, Zhang et al. (2017) propose an adaptive control scheme of an interlinking three phase inverter, which bridges a DC and an AC microgrid. In this work, a fully data-driven controller is combined with other classic control methods in microgrids, such as droop control[1], for voltage regulation and power flow control. Within the overall control diagram, an inner data-driven MFAC voltage controller is designed to regulate both grids, i.e., the DC voltage level and the AC frequency, while also compensating for any disturbances, which are common in converter-dominated microgrids. The performance metric is based on the one-step ahead voltage error estimation. A more specific converter application is investigated in Wang et al. (2023), in which a bidirectional interleaved boost converter is applied to link a DC bus with an ultracapacitor stack. By comparing two cascade control structures, one based on traditional PI control and another in MFAC with a proposed cost function optimization, it was verified that the latter resulted in better transient performance and disturbance rejection with half of the settling time. Robustness was also improved by checking the current ripple under the effect of inductance parametric variations, due to the adaptive characteristics of the MFAC method. However, it

[1] Power flow control method, which may use the AC voltage signal's frequency and amplitude as the control action.

should be noted that the model-based PI controller did not consider parametric uncertainty in its project, which could have been done for the sake of fairness. Finally, the last publication by Asadi et al. (2021) applies MFAC to the control of Z-source inverters, which present a non-minimum phase dynamic model and can be more challenging for the design of traditional linear controllers. The proposed MFAC technique is combined with an integrator and aims to minimize a cost function based on the weighting of the one-step ahead prediction error and the control action variation. The corresponding optimal control law is a known result in literature (Hou; Wang, 2013) and is applied to the analyzed circuit topology. A comparison between the DDC method and model-based strategies such as PI control, pole-allocation and LQR has shown that MFAC results in better performance considering the metrics of total variation and overshoot in the presence of load variations.

All three works utilize conventional PPD matrices estimation techniques and can guarantee stability if certain hypothesis are met (Hou; Jin, 2013), which is one of the major advantages of MFAC. However, for the PPD matrix estimation, some control parameters are required to be tuned, which can often be cumbersome in practice and demand several tests or simulations to accomplish. Therefore, it would be an improvement for newer adaptive techniques to explore and systematically optimize this step on the control design process.

2.1.5 DD-MPC

Model predictive control can be described as a control strategy that optimizes a certain cost function J over a predefined horizon in time N, subject to a model of the system and user-defined restrictions (Rodriguez; Cortes, 2012). This can be stated as an optimization problem in the form of

$$\min_{\{\mathbf{u}(k),\ldots,\mathbf{u}(k+N)\}} J = f(\mathbf{x}(k),\mathbf{u}(k),\ldots,\mathbf{u}(k+N)), \tag{2.4}$$

where $\mathbf{x}(k)$ represents the measured states of the system at instant k. As this problem is solved at each sampling interval, it can get quite computationally expensive for converters operating at a high sampling frequencies (Mohamed et al., 2019). The control action here may be the switching states directly or another variable considering the application of a modulation technique (Geyer, 2016).

Although MPC is a classical control method applied power electronics, fewer publications have explored the data-driven variation of the methodology. In this regard, a formulation which leverages robustness is shown by Huang et al. (2023) with an example control application for power regulation with a three phase inverter. Here the Data Enabled Model Predictive Control (DeePC) method, which is derived from behavior theory, is adapted to handle different types of uncertainty in input/output data. Depending on the degree of conservatism, multiple types of uncertainty (structured, unstructured) can be considered and taken into account in the

optimization problem. It has been proven that the robust version results in a bounded cost for the real system, as long as the uncertainty set contains the exact data.

Given the simplicity and main advantages of VRFT over the other techniques, the rest of this work focuses on applying this method on the totem-pole boost bridgeless rectifier. As such, the next section discusses in detail the working principles and logic of VRFT for single and cascade control loops.

2.2 DATA-DRIVEN MODEL REFERENCE CONTROL

In this section the classic MRC problem and its data-driven solution utilizing the VRFT method is discussed.

2.2.1 Model Reference Control Problem

The MRC problem aims to minimize a cost function considering a desired closed loop model $T_d(z)$ for the system, such that $y_d(k) = T_d(z)r(k)$ is the target output signal considering the reference $r(k)$. Consider the Single-Input Single-Output system presented in Figure 2, where $G(z)$ is the transfer function which represents the process. The output of the system can be described by

$$y(k) = G(z)u(k) + \nu(k), \tag{2.5}$$

where $u(k)$ is the control action, z is the forward time-shift operator, i.e., $zx(k) = x(k+1)$, and ν is a noise term capturing uncertainties not represented by $G(z)$. Let the control law of this system be a function of a controller $C(z,\rho)$ with a parameter vector $\rho \in \mathbb{R}^p$ such that $u(k) = C(z,\rho)(r(k) - y(k))$.

Figure 2 – Considered SISO system for MRC.

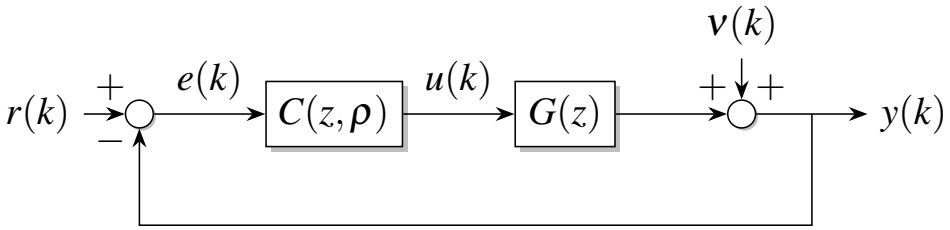

Source: the author (2025).

With that, the MRC problem can be stated as (Bazanella; Campestrini; Eckhard, 2011)

$$\min_{\rho} J^{\mathrm{MR}}(\rho) = \|(T(z,\rho) - T_d(z))r(k)\|_2^2, \tag{2.6}$$

where $T(z,\rho)$ is the closed-loop system given by

$$T(z,\rho) = \frac{C(z,\rho)G(z)}{1 + C(z,\rho)G(z)}. \tag{2.7}$$

The ideal controller which solves (2.6) is given by

$$C_d(z) = \frac{T_d(z)}{G(z)(1 - T_d(z))}. \tag{2.8}$$

By the usage of this framework, it can be stated that the VRFT tries to identify $C_d(z)$ from the input-output data of the process. If the control law is parametrized so that it is a linear function of ρ, then there is an analytical solution for (2.6), which the method exploits. This is explained further in the next subsection.

2.2.2 Virtual Reference Feedback Tuning (VRFT)

The VRFT method is a data-driven technique which is able to solve the MRC problem with a set of data collected from the process (Bazanella; Campestrini; Eckhard, 2011). One of its main advantages is the fact that is a one-shot method, so it only requires one batch of sampled data $\{u(k), y(k)\}_{k=1}^{N}$ for the algorithm to run offline and return a controller which is close to $C_d(z)$.

In order to do that, the VRFT technique transforms the MRC problem into an equivalent identification problem of the optimal controller and solves it through a least-squares solution, which is feasible if the controller's structure is linearly parametrized in respect to a set of parameters, as in

$$C(z, \rho) = \rho^T \bar{C}(z), \tag{2.9}$$

where $\rho \in \mathbb{R}^p$ and $\bar{C}(z)$ is a vector of transfer functions of the same length. Note that by restricting the controller to this form, it follows that its poles are fixed and the VRFT manages the optimal location of the zeros and gain.

With this restriction, assume that a batch of input-output data $\{u(k), y(k)\}_{k=1}^{N}$ is available. Then, let $\bar{r}(k) = T_d^{-1}(z)y(k)$ be defined as the *virtual reference* signal and $\bar{e}(k) = \bar{r}(k) - y(k)$ be defined as the *virtual error*, according to the diagram of Figure 3. The VRFT aims to identify the optimal controller $C(z, \rho)$ that would have generated the signal $u(k)$ if fed by the error signal $\bar{e}(k)$. To this end, it minimizes the 2-norm of the residues, which is represented by the optimization problem below:

$$\begin{aligned} &\min_{\rho} J^{\mathrm{VR}}(\rho) \\ &J^{\mathrm{VR}}(\rho) = \|u(k) - C(z, \rho)(T_d^{-1} - 1)y(k)\|_2^2, \end{aligned} \tag{2.10}$$

which has the same minimum as the Model Reference (MR) cost J^{MR} if the ideal controller $C_d(z)$ can be written as a linear combination of $\bar{C}(z)$, or, in other words, if $C_d \in \mathscr{C} = \{\rho^T \bar{C}(z), \rho \in \mathbb{R}^p\}$. As this is rarely the case, it's possible to apply a specific filter $L(z)$ to the data before solving (2.10) in order to approximate both minimums (Bazanella; Campestrini; Eckhard, 2011). By making sure that the two cost functions have their own minimum around the same value of ρ, the

design is oriented to tune $C(z,\rho)$ to achieve the best closed-loop response $T(z)$ considering the quadratic error as cost. In other words, the filter $L(z)$ is used to ensure that the design procedure returns the best possible response considering the limitations in the chosen controller class $\mathscr{C}$. In this case, the filter's magnitude must satisfy

$$|L(e^{j\Omega})|^2 = |T_d(e^{j\Omega})|^2|1-T_d(e^{j\Omega})|^2\frac{\phi_r(e^{j\Omega})}{\phi_u(e^{j\Omega})},\ \forall\Omega\in[-\pi,\pi], \tag{2.11}$$

where $\phi_r(e^{j\Omega})$ and $\phi_u(e^{j\Omega})$ are the power spectra of $r(k)$ and $u(k)$, respectively. It's remarked that this equation relies on the approximation $|S(e^{j\Omega},\rho)|^2 \approx |S_d(e^{j\Omega})|^2 = |1-T_d(e^{j\Omega})|^2$. Regarding the deduction of (2.11), a detailed proof is shown in (Bazanella; Campestrini; Eckhard, 2011, p. 34), but in short, the filter's expression can be deduced by comparing the model reference cost function (2.6) and VRFT's cost function (2.10) in the frequency domain using Parseval's theorem. By proposing the filter $L(z)$ as a free design parameter, any filter that satisfies (2.11) tends to reduce the MRC cost in the end, resulting in a better controller belonging to $\mathscr{C}$.

Figure 3 – Block diagram corresponding to the virtual signals used in VRFT.

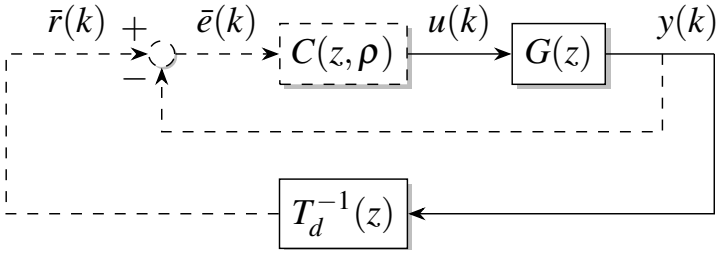

Source: the author (2025).

Since the collected data is corrupted noise, in practice an Instrumental Variable (IV) solution to (2.10) is applied, which utilizes another set of data which is strongly correlated with the first. A usual choice is to just reapply the same input signal and collect two sets of data, which can still be done with just one experiment (Remes et al., 2021). To this end, consider the notation

$$x_L(k) = L(z)x(k), \tag{2.12}$$

where $x(k)$ is any signal and x_L is its filtered version considering an $L(z)$ which satisfies (2.11). Consider as well that $y'(k)$ is an instrumental variable. Then, the VRFT least-squares solution of (2.10) can be stated as

$$\hat{\rho}^{\mathrm{VR}} = \left[\sum_{k=1}^{N}\xi_\rho(k)\psi_\rho^T(k)\right]^{-1}\sum_{k=1}^{N}\xi_\rho(k)\zeta_\rho(k), \tag{2.13}$$

where

$$\xi_\rho(k) = \bar{C}(z)(1-T_d(z))y'_L(k), \tag{2.14}$$

$$\psi_\rho(k) = \bar{C}(z)(1-T_d(z))y_L(k), \tag{2.15}$$

$$\zeta_\rho(k) = T_d(z)u_L(k). \tag{2.16}$$

It's remarked that this VRFT formulation is only suitable for minimum-phase plants. For the non-minimum phase case, extensions of the method are also present in the literature (Bazanella; Campestrini; Eckhard, 2011; Remes et al., 2021).

2.2.3 Cascade control structure

This work adopts the cascade control structure shown in Figure 4, where the process is divided into two subsystems $G_i(z)$ and $G_e(z)$, that is

$$y_i(k) = G_i(k)u_i(k) + \nu_i, \tag{2.17}$$

$$y_e(k) = G_e(k)y_i(k) + \nu_e, \tag{2.18}$$

where $y_i(k), y_e(k)$ are the internal and external subsystem's outputs respectively, ν_i, ν_e are noise terms that encompass model and measurement error, $u_i(k)$ is the control signal and $G_i(z)$ and $G_e(z)$ are transfer functions that represent the process. In DC-DC converters in general it can be proposed that the internal subsystem is the 'inductor current as a function of the duty-cycle' transfer function, whereas the external subsystem is the 'capacitor voltage as a function of the inductor current' transfer function (Erickson; Maksimovic, 2020). The objective is to attain simultaneous tracking of both the internal and external references r_i and r_e.

The reasoning for focusing on this architecture is that, in general, there are several advantages with the use of cascade control, such as multiple reference tracking, improved disturbance rejection and simplicity over 'multiple input multiple output' methods (Skogestad; Postlethwaite, 2005; Remes et al., 2020; Corleta et al., 2016; Wang; Ren; Chen, 2019). It's also easier to propose two separate reference models than a reference transfer function matrix in the multivariable case. In the context of power converters, several recent applications make use of this structure (Schrittwieser et al., 2018; Li et al., 2019; Qin et al., 2018; Pandey; Singh, 2019; Belkamel; Kim; Choi, 2020), which further validates its advantages. Furthermore, null steady-state error is feasible since both controllers $C_i(z)$ and $C_e(z)$ are in the direct path.

Figure 4 – Block diagram of the considered cascade control system omitting perturbations.

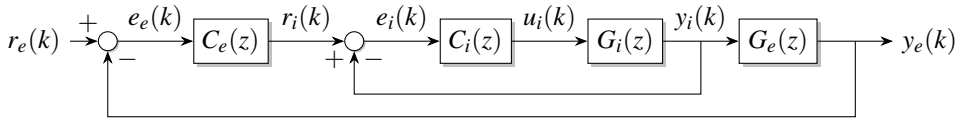

Source: the author (2025).

A general distinction between DC-DC converters and PFC rectifiers is the region of operation concerning the variations of the converter's states. The former tends to operate around small variations of a fixed point, for example the mean inductor current and capacitor voltage of a buck converter. This enables the use of linearization techniques in order to create a transfer-function model of the converter, which can be utilized in model-based techniques. For boost PFC rectifiers, it's desired to control the input current such that it follows a sinusoidal trajectory

(Erickson; Maksimovic, 2020). On the other hand, because of the sinusoidal shape of the input current, the inductor's current tends to follow the same signal and thus it doesn't vary around a single fixed value, but instead it fluctuates around a specific sinusoidal trajectory. This behavior can be described by linearizing the average state model around a known trajectory, which is equivalent to a small-signal Linear Time Varying (LTV) model (Khalil, 2002). While this points at the use of nonlinear techniques suitable for such systems, linear control techniques in the literature still provide good results and are simpler to analyze (Schrittwieser et al., 2018; Li et al., 2019; Qin et al., 2018; Pandey; Singh, 2019; Belkamel; Kim; Choi, 2020), which motivates the use of linear data-driven control techniques, such as VRFT. An extension of this technique for cascade systems has been presented by Remes et al. (2020), where it was also studied in the context of DC-DC converters. However, there is a notable nonlinearity present in the control diagram for PFC rectifiers, which is the sinusoidal multiplier used to synthesize the current reference. Further context on the purpose of the multiplier is given in Chapter 3. Since this nonlinearity is directly in the signal path after the external controller $C_e(z)$, as shown in Figure 5 through the multiplying term $k_m|\sin\theta(k)|$, where k_m is simply an arbitrary constant, the technique in that paper can't directly be translated to the application of interest. To contour this problem, it's proposed to transform the control design problem in the cascade structure to two individual identification problems, which then can be solved independently with VRFT. Chapter 4 formalizes these propositions.

Figure 5 – Block diagram of the considered cascade control system with the sinusoidal multiplier omitting perturbations.

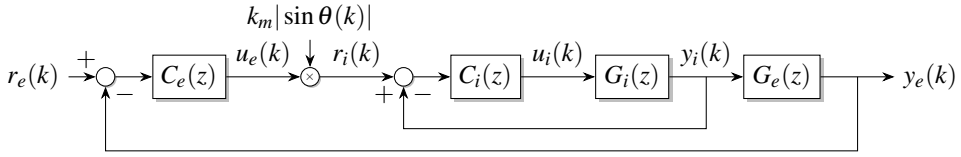

Source: the author (2025).

2.3 FINAL CONSIDERATIONS

In the context of power electronics, DDC techniques have already been applied in several areas, specially in power systems. This chapter has reviewed several papers contemplating multiple existing techniques. The methods were also classified in a tree-diagram of Figure 1, in which a division between classical and AI methods is made.

For the classical methods, a strong advantage is found in direct methods, which do not rely on an identification step for the system. Among them, VRFT has some distinct advantages, such as being a one-shot technique, relying only on the data of one experiment (Remes et al., 2021). Another advantage is the simplicity of the method, which isn't based in complex optimization procedures. In fact, the classic VRFT application consists of a straightforward computation solving a least squares problem (Bazanella; Campestrini; Eckhard, 2011). Furthermore, the

complexity of the output resulting controller is a design parameter. In other words, a low-order controller which optimizes the Model Reference (MR) performance metric can be obtained with VRFT, which results in desirable robustness properties. Finally, extensions of the method for non-minimum phase systems and with hard robustness constraints can be found in the literature (Remes et al., 2021; Fiorio et al., 2021).

Regarding VRFT, while this method has been applied to DC-DC converters before, these are often studied in the context of small variations around a single fixed point, which can be well characterized by linear dynamics. As such, there is a gap in the literature concerning its application in more complex converters, where some nonlinearities are more noticeable. In particular, PFC rectifiers are a notable area of application, since they present a large signal variation concerning the duty-cycle, inductor current and input voltage even in steady-state. Furthermore, the use of linear controllers in the literature also motivates the application of VRFT (Schrittwieser et al., 2018; Li et al., 2019; Qin et al., 2018; Pandey; Singh, 2019; Belkamel; Kim; Choi, 2020). On the other hand, the small-signal dynamics of the boost PFC converter are best and often solved with a cascade control loop along with a sinusoidal multiplier (Skogestad; Postlethwaite, 2005). For this case, some adaptations in the ways VRFT is applied in the literature must be considered, such that this nonlinearity is adequately dealt with. Therefore, the next chapter describes a rectifier in the boost PFC family, stating some information which is utilized later to particularize a VRFT formulation to this family of converters.

3 TOTEM-POLE BOOST BRIDGELESS RECTIFIER

The totem-pole boost bridgeless converter is discussed in this chapter. Since VRFT relies on the assumption that the controller class is capable of yielding a closed-loop system which is close to the reference model, this chapter also describes the known small-signal models present in the literature, which are used later to compose a suitable space of functions for the current reference models. In addition, some PFC concepts are discussed, and some performance metrics are presented.

3.1 SOME PFC CONCEPTS

The Power Factor (PF) is a metric utilized to measure how effectively electrical energy is transmitted from a source to its load (Erickson; Maksimovic, 2020). In the context of loads being connected to the electric grid, it's assumed the that input voltage $v_{in}(t)$ and current $i_{in}(t)$ present periodic behavior corresponding to a period T. First, let P_{in} be the average power flowing through the input source given by

$$P_{in} = \frac{1}{T}\int_0^T v_{in}(t)\, i_{in}(t)dt. \tag{3.1}$$

Let the Root Mean Square (RMS) value of a signal x be denoted by X^{rms}. The apparent power flowing through the source can be defined as product between the RMS values of its voltage and current, that is

$$S_{in} = V_{in}^{\text{rms}}\, I_{in}^{\text{rms}}. \tag{3.2}$$

The PF can thus be defined as the ratio between the average power and the apparent power flowing through the input source, in short

$$\text{PF} = \frac{P_{in}}{S_{in}}. \tag{3.3}$$

Usually, the norms concerning to the PF of various products also establish limits to the harmonics of the input current. Let a signal $x(t)$ be periodic with period T. Then, it can always be expressed as a Fourier series by

$$x(t) = X_0 + \sum_{n=1}^{\infty} X_n \cos(n\omega t - \phi_n), \tag{3.4}$$

where X_0 is its average value, X_n represents its harmonics amplitude, ϕ_n is the phase of the harmonic n and $\omega = 2\pi/T$. The standard pertinent with the study cases in this work is the IEC 61000-3-2 (IEC, 2018).

Among the consequences of a poor PF and large harmonic content in electrical installations and equipment, the main ones are (Oruganti; Srinivasan, 1997):

- Overheating of the neutral line;
- Interference with communication and control signals;
- Inefficient use of volt-ampere ratings of transformers, distribution lines, generators, among others.

There are several solutions for meeting PF requirements in electrical equipment. For low power applications, passive solutions are still attractive due to its lower cost (Kalair et al., 2017; Sayed; Massoud, 2022; Oruganti; Srinivasan, 1997). In addition, their simplicity and robustness make them appropriate for certain applications. Some examples of passive PFC methods are: inductive filters at the AC or DC side of a rectifier, LC filters, resonant input filters and beyond.

For higher-power applications, some disadvantages of passive methods start to arise, for instance the size of the filter's components start to become exceedingly large, making them not very cost-effective. Furthermore, they are often not able to meet standards' requirements, as their performance is, in general, worse than active methods. As such, active PFC techniques, which use active components like IGBTs or MOSFETs, tend to be more suitable in higher power contexts, or when the size of the product is a primary concern. For example, with the increasing popularity of electric vehicles in the market, there is a higher demand for electric charging stations, which often use an active PFC front-end stage (Rafi; Bauman, 2021).

Active PFC rectifiers are structured into multiple topologies, from the fundamental buck, boost and buck-boost converters to hybrid versions of them (Oruganti; Srinivasan, 1997; Mansouri et al., 2013). Multilevel topologies are also a topic of study and can manage to reach high power-density levels (Qin et al., 2019). In terms of simplicity, the boost PFC family of converters is often preferred, specially when considering the control of the current waveform, which can be modelled by a linear plant when the rectifier operates in CCM. To obtain a close to unit PF, it's required to reduce the harmonic content of the input current signal, since these components do not contribute to the active power demanded by the application, as they are orthogonal to a sinusoidal input voltage considering (3.1). Moreover, it's also required to minimize the phase difference between the fundamental component of $i_{in}(t)$ and $v_{in}(t)$, i.e. they should be in phase. Thus, a good control of the input current signal is fundamental for this type of application.

In the boost PFC family, bridgeless variations, which integrate the rectifier bridge with the boost PFC operation, are often preferred in certain applications due to the lower conduction losses (Rafi; Bauman, 2021; Huber; Jang; Jovanovic, 2008; Fischer; Rech; Novaes, 2020). For this reason, the totem-pole boost bridgeless converter and its operation stages are presented in the next section. This topology in specific is relevant due to the fact that recent semiconductor technologies, such as Silicon Carbide and Gallium Nitride, manage to reduce the switching losses as well, turning this converter an interesting solution to maximize efficiency in many cases (Fischer; Rech; Novaes, 2020; Huang; Huang, 2017).

3.2 TOTEM-POLE BOOST BRIDGELESS RECTIFIER

This section contains a short summary of the totem-pole boost bridgeless rectifier and its operation stages. First, this topology is presented in Figure 6, where L_b is the boost inductor, C_o is the output capacitor of the rectifier, R_o is the equivalent load resistance, i_C is the capacitor's current, i_L is the inductor's current, which is the same as the input current, and v_{in} is the sinusoidal input voltage. Moreover, the capacitor's voltage v_C and the output voltage v_o are also the same. The switching elements of the converter are the diodes D_1, D_2 and the switches S_1, S_2. IBGTs are drawn for illustration purposes, but other semiconductor technologies are also possible. Later this specific topology is used in simulation examples and experimental case studies.

Figure 6 – Totem-pole boost bridgeless rectifier.

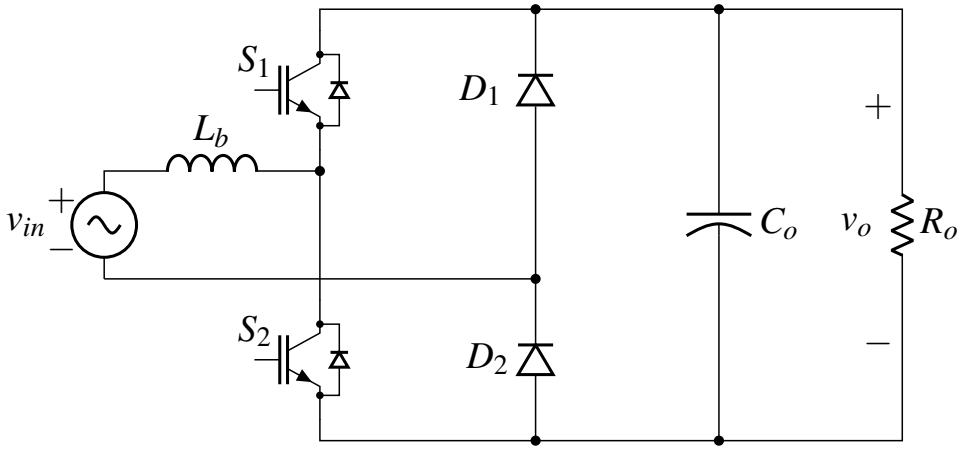

Source: the author (2025).

Considering operation in CCM, the rectifier's operation stages are shown in Figure 7, where one of the diodes D_1 or D_2 conducts depending on the polarity of the input current. In case it's positive, only D_2 conducts and the switching of S_2 determines whether the inductor L_b is magnetized (S_2 on) or demagnetized (S_2 off). In case $i_L < 0$, D_1 conducts and S_1 switches similarly. When the inductor is being magnetized, as in Figs. 7a and 7c, it assumes the voltage of v_{in}, and thus it's energized obeying

$$\frac{di_L}{dt} = \frac{v_{in}(t)}{L_b}. \tag{3.5}$$

During these states only the output capacitor sustains the output voltage. When the inductor is being demagnetized, corresponding to the states of Figs. 7b and 7d, it obeys the differential equation

$$\frac{di_L}{dt} = \frac{v_{in}(t) - \text{sign}(i_L(t))v_o}{L_b}, \tag{3.6}$$

where $\text{sign}(i_L)$ corresponds to 1 if $i_L > 0$ or -1 if $i_L < 0$.

Closed-loop control is required to ensure the input current follows a specific trajectory, which is normally a sinusoidal curve. As such, the control objectives for this converter correspond

Figure 7 – Operation stages for the totem-pole boost bridgeless rectifier.

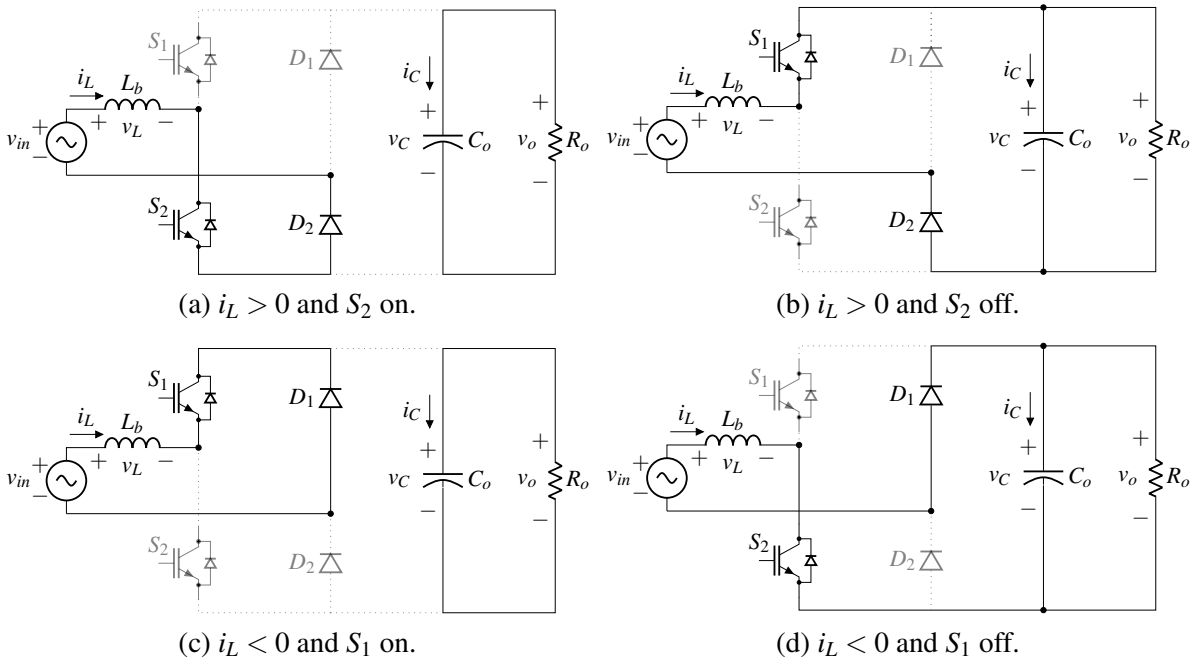

(a) $i_L > 0$ and S_2 on.

(b) $i_L > 0$ and S_2 off.

(c) $i_L < 0$ and S_1 on.

(d) $i_L < 0$ and S_1 off.

Source: the author (2025).

to regulate the output voltage while maintaining the input current's harmonics within predefined limits of pertinent standards. There are several ways to design the control system to this end, but a focus on average current control with two control loops in cascade is given. This structure is detailed in sequence.

3.2.1 Control diagram for PFC

Applying the cascade control structure of Figure 4 to the totem-pole boost bridgeless rectifier, the Figure 8 illustrates how the whole system is organized. In the diagram, $H_i(s)$ and $H_{vo}(s)$ represent the input current $i_{in}(t)$ and output voltage $v_o(t)$ sensor's transfer functions, resulting in the measured variables $i_{in,\text{meas}}$ and $v_{o,\text{meas}}$, respectively. Both sensors have unitary DC gain in this formulation, which is always possible to adjust digitally. Correspondingly, the internal and external outputs are $y_i(t) = |i_{in}(t)|$ and $y_e(t) = v_o(t)$. The cascade control loop first actuates in the external one, generating the internal reference i_{ref} for the internal loop, which calculates the duty-cycle $d(k) \in [0,1]$ for the modulation process.

There are two additional features in the control loop: i) First, a Phase Locked Loop (PLL) is introduced to generate a purely rectified sinusoidal signal to generate the current reference; ii) Second, a parameter varying gain is implemented by a peak detector on the input voltage signal. This varying gain is given by $V_{in,\text{max}}/V_{in,\text{peak}}$, where $V_{in,\text{max}}$ is the maximum value that the input voltage can admit and $V_{in,\text{peak}}$ is the currently detected peak of $v_{in}(t)$. The consequence of introducing this varying gain is to decouple the effect of a varying peak of $v_{in}(t)$ in the voltage loop (Erickson; Maksimovic, 2020, p. 884). This is further elaborated in Section 3.2.3.

Moreover, different variations of boost PFC rectifiers may introduce more switches, while keeping the same principles of operation of the boost converter. In these cases, the only differences from the control diagram are in the Pulse Width Modulation (PWM) block, which should decide accordingly which switches to drive. Indeed, the totem-pole bridgeless variation of the boost rectifier selects either S_1 or S_2 to command with a duty-cycle $d(k)$, and this is made based on the sign of the tracked PLL output signal. If it's positive, then S_2 is modulated, otherwise S_1 is the active switch for modulation. This is illustrated in Figure 8 by the block TP-PWM.

Figure 8 – Considered control diagram for the PFC rectifier.

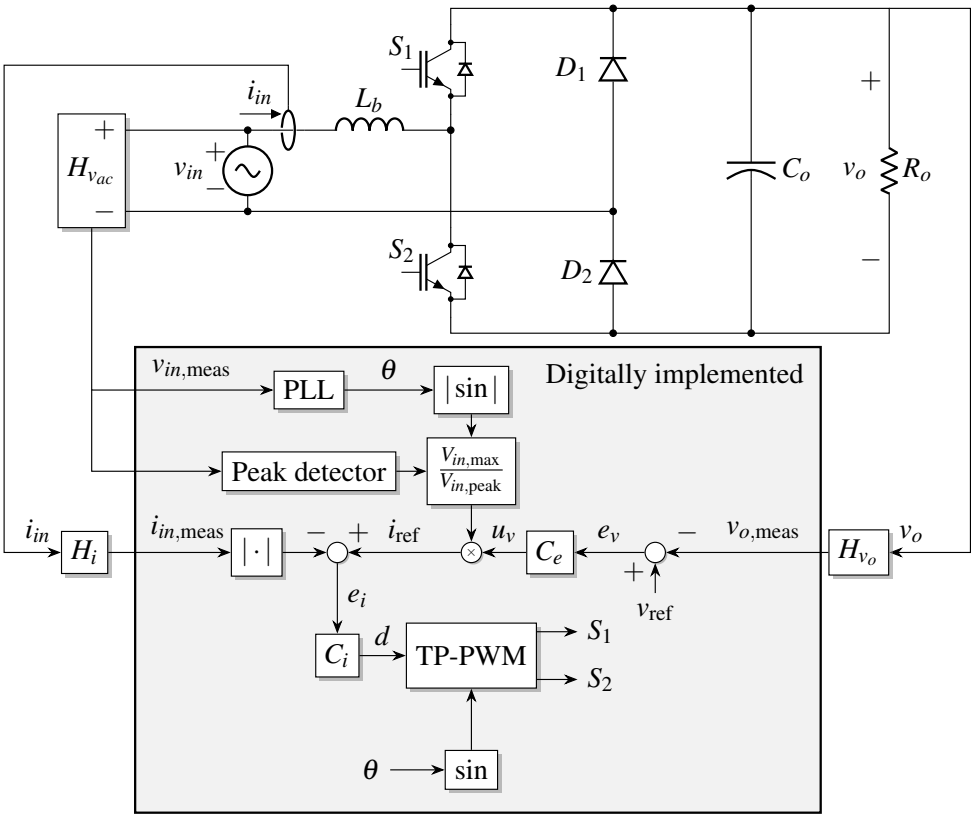

Source: the author (2025).

3.2.2 PLL implementation

The PLL structure is chosen to be a Moving Average Filter Power PLL designed with the symmetrical optimum method (Golestan; Guerrero; Vasquez, 2017). This technique is chosen due to its simplicity and higher performance when comparing with the simplest possible PLL structure (Golestan et al., 2014). In this aspect, the PLL is described by the diagram of Figure 9, where the input of the PLL is the measured input voltage $v_{\text{ac,meas}}$, and its output is the angle $\hat{\theta}$, which should track the angle of the input signal in steady state.

First, the Moving Average (MA) filter is specified to have a window length T_w of $1/(2f_{ac})$ to attenuate harmonics which are multiple of two times the line frequency f_{ac}, e.g. 60 Hz in

the case of this work. Moreover, it operates with a sampling frequency arbitrarily chosen to be 480 Hz, which is sufficient considering that the input signal is approximately a 60 Hz sinusoid. With those definitions, the filter is specified to have $480\,\text{Hz}/120\,\text{Hz} = 4$ taps.

The PLL Low Pass Filter (LPF) is designed with the methods described by Golestan, Guerrero, and Vasquez (2017). It's worth remarking that the interface between the output of the MA block and the LPF is made by a zero order hold, i.e. by keeping the output of the MA filter constant. Specifying the LPF as a PI filter, it follows that its coefficients can be determined by (Golestan et al., 2014)

$$k_{p,\text{PLL}} = \frac{2}{T_w \cdot b}, \tag{3.7}$$

$$k_{i,\text{PLL}} = \frac{4}{T_w^2 \cdot b^3}, \tag{3.8}$$

where b is a design parameter that leverages damping and phase-margin (Golestan et al., 2014). With the desired window length, and by utilizing $b = 2.4$, which corresponds to a fast and well damped response with a phase-margin of 45º, the corresponding PI controller can be converted to the discrete form through the Tustin approximation considering the sampling frequency f_s, which is the same as the switching frequency of 64.8 kHz in this work. Therefore, this results in the difference equation

$$y(k) = y(k-1) + 100u(k) - 99.97u(k-1). \tag{3.9}$$

The equation above and the MA filter are used in the simulation study cases and experimentally on a microcontroller in order to implement the PLL.

Figure 9 – Moving Average Filter Power PLL diagram.

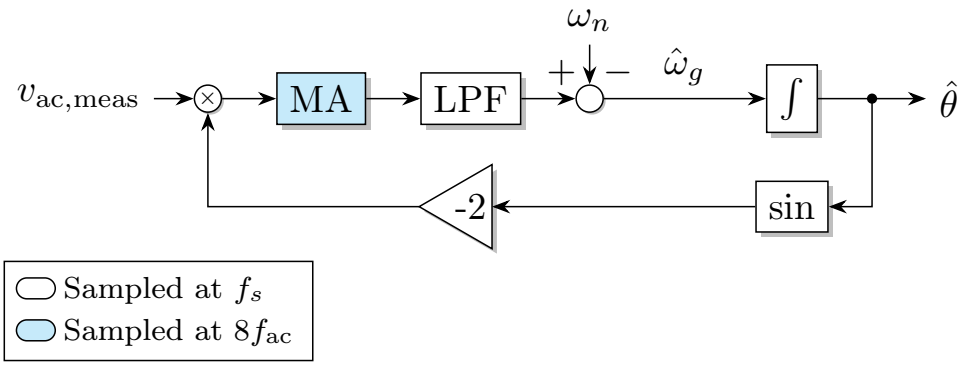

Source: the author (2025).

3.2.3 Small-signal models

Although this work aims at developing a data-driven framework to a PFC control system, there is still useful information that can be extracted from approximate models of switched converters. In particular, it's proposed in Section 4.4 that these models can be utilized in order to

determine the optimal point of operation during data-collection, so that stability is guaranteed in every possible operating region during CCM.

To that end, it's well known that, for the boost converter, the inductor's average voltage in a switching cycle $\langle v_L(t)\rangle_{T_s}$ can be expressed as a function of the duty-cycle $d(t)$, the average input voltage $\langle v_{in}(t)\rangle_{T_s}$ and the average output voltage $\langle v_o(t)\rangle_{T_s}$ by (Erickson; Maksimovic, 2020)

$$\langle v_L(t)\rangle_{T_s} = \langle v_{in}(t)\rangle_{T_s} + [d(t)-1]\langle v_o(t)\rangle_{T_s}. \tag{3.10}$$

As $\langle v_L(t)\rangle_{T_s} = L_b d\langle i_L(t)\rangle/dt$, the inductor's current dynamics can be described by the equation

$$L_b \frac{d\langle i_L(t)\rangle}{dt} = \langle v_{in}(t)\rangle_{T_s} + [d(t)-1]\langle v_o(t)\rangle_{T_s}, \tag{3.11}$$

which is a nonlinear differential equation because of the multiplication between $\langle v_o(t)\rangle_{T_s}$ and $d(t)$.

If the ripple in the output voltage signal is small, the approximation $\langle v_o(t)\rangle_{T_s} \approx V_o + \hat{v}_o(t)$ is valid, where $\hat{v}_o(t) \ll V_o$ represents the small-signal variations of the average output voltage. Substituting this in (3.11) returns

$$L_b \frac{d\langle i_L(t)\rangle}{dt} = \langle v_{in}(t)\rangle_{T_s} + V_o\,[d(t)-1] + \hat{v}_o(t)\,[d(t)-1]. \tag{3.12}$$

Since $\hat{v}_o(t) \ll V_o$, the last term in this equation can be discarded, resulting the differential equation

$$L_b \frac{d\langle i_L(t)\rangle}{dt} \approx \langle v_{in}(t)\rangle_{T_s} + V_o\,[d(t)-1], \tag{3.13}$$

which is linear in $\langle v_{in}(t)\rangle_{T_s}$ and $d(t)$. By taking the Laplace transform of the above, the following transfer matrix model for the inductor's current $i_L(s) = \mathbf{M}_i(s)\begin{bmatrix} d(s) & v_{in}(s)\end{bmatrix}^T$ can be deduced, which is valid for any trajectory of $i_L(t)$, as long as the converter remains in CCM and the output voltage does not drift away from V_o:

$$\mathbf{M}_i(s) = \begin{bmatrix} \frac{V_o}{L_b s} & \frac{1}{L_b s}\end{bmatrix}. \tag{3.14}$$

The current to duty-cycle transfer function model $G_i(s)$ is simply the first term of $\mathbf{M}_i(s)$, so

$$G_i(s) = \frac{V_o}{L_b s}. \tag{3.15}$$

The exact discretization of $G_i(s)$, considering the presence of a zero order hold and a sampling time T_s, yields an internal subsystem of the form

$$G_i(z) = \frac{K_{Gi}}{z-1}, \tag{3.16}$$

where $K_{Gi} = V_o \cdot T_s / L_b$ the equivalent gain of the discretized model.

Alternatively, for the external loop model, the rectifier is first modelled as a loss free resistor, as shown in Figure 10. The period for averaging in this case half of the line period, i.e., $T_{2L} = 0.5/f_{\text{line}}$, where f_{lines} is the frequency of the line voltage. Here, the rectifier is modelled as a power source. As no losses are taken into account, the power balance of the equivalent circuit is expressed by the differential equation

$$\frac{1}{2}C_o \frac{d\langle v_o(t)\rangle_{T_{2L}}^2}{dt} + \frac{\langle v_o\rangle_{T_{2L}}^2}{R_o} = \langle p_{in}\rangle_{T_{2L}}(t). \tag{3.17}$$

Linearizing around $\langle v_o(t)\rangle_{T_{2L}} = V_o + \hat{v}_o(t)$ and $\langle p_{in}(t)\rangle_{T_{2L}} = P_{in} + \hat{p}_{in}(t)$, and dropping the higher order terms, it follows that

$$C_o V_o \frac{d\hat{v}_o}{dt} + \frac{2V_o\hat{v}_o}{R_o} = \hat{p}_{in}. \tag{3.18}$$

Next, the variations in the input power are equal to the input voltage times the input current, i.e., $\hat{p}_{in}(t) = V_{in,\text{peak}} \cdot \hat{I}_{in,\text{peak}}(t)/2$. If the inner current loop is much faster than the line frequency, the approximation $\hat{I}_{in,\text{peak}}(t) = \hat{I}_{\text{ref}}(t)$ can be made, where $\hat{I}_{\text{ref}}(t)$ is the peak current reference.

To illustrate the effect of the varying gain block $V_{in,\max}/V_{in,\text{peak}}$ of Figure 8, the equivalent external loop model without this gain, i.e. with a unitary gain instead, is derived first. In this case, it follows that $\hat{I}_{\text{ref}}(t) = u_v(t)$, where $u_v(t)$ is the voltage controller's output. As such, (3.18) can be rewritten as

$$C_o V_o \frac{d\hat{v}_o}{dt} + \frac{2V_o\hat{v}_o}{R_o} = \frac{V_{in,\text{peak}}}{2} \cdot u_v(t). \tag{3.19}$$

Taking the Laplace transform of the above yields

$$G_{e1}(s) = \frac{V_o(s)}{U_v(s)} = \frac{R_o}{4} \cdot \frac{V_{in,\text{peak}}}{V_o} \cdot \frac{1}{1 + 0.5R_oC_os}, \tag{3.20}$$

where it's noticeable there is a gain which is directly proportional with the peak of the line's voltage $V_{in,\text{peak}}$.

On the other hand, if the varying gain block $V_{in,\max}/V_{in,\text{peak}}$ is used, then it follows that $\hat{I}_{\text{ref}}(t) = V_{in\,\max}/V_{in,\text{peak}} \cdot u_v(t)$. Substituting this in (3.18) and taking the Laplace transform results in the decoupled model

$$G_e(s) = \frac{V_o(s)}{U_v(s)} = \frac{R_o}{4} \cdot \frac{V_{in,\max}}{V_o} \cdot \frac{1}{1 + 0.5R_oC_os}. \tag{3.21}$$

The model of (3.21) contains a single pole and a DC gain term. Its equivalent discretized model, considering the zero order hold method and a sampling time T_s, is given by

$$G_e(z) = \frac{K_{Ge}}{z - p_{Ge}}, \tag{3.22}$$

where K_{Ge} and p_{Ge} are the equivalent gain and pole of the discretized model. The specific values of K_{Ge} and p_{Ge} can be calculated with the knowledge of the system's parameters, but are not important for the data-driven design.

Figure 10 – Average loss free model of the rectifier stage.

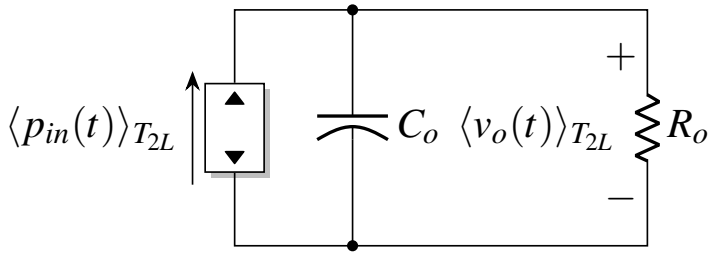

Source: the author (2025).

3.3 FINAL CONSIDERATIONS

This chapter has presented the totem-pole boost bridgeless rectifier and its operation stages. Although it's a specific converter among the boost PFC family, the control structure defined by Figure 8 is easily adaptable to other boost PFC topologies. Indeed, the small-signal models derived in Section 3.2.3 are still valid for the boost PFC converter family in CCM operation and are used in the next chapter to derive suitable reference models for both loops. The next chapter formulates the main results of this dissertation, where VRFT for cascade control systems is particularized for boost PFC rectifiers in general.

4 VRFT APPLIED TO BOOST PFC RECTIFIERS

In this chapter the control design problem for PFC converters is discussed, focusing on the cascade control architecture. Not only this structure has several advantages, as previously discussed, but the separation of internal and external dynamics makes it easier to design good and attainable reference models. The control design problem follows the MRC framework, whose optimal solution can be obtained by employing the data-driven controller-design technique VRFT.

In the VRFT context, the design of a discrete-time controller relies on the choice of the controller class, reference model and collected data from the process. Each of these aspects is discussed in sequence and needs to be compatible with the control objectives for the converter. For the boost PFC case, it's desirable to obtain simultaneous tracking of the output DC voltage and the sinusoidal input current, keeping it in phase with the input voltage, while also rejecting any external disturbances in the system, such as load or input voltage steps.

4.1 CONTROLLER CLASSES

Aiming at robustness and simplicity, low order controllers are preferred for both loops. For the current loop, since one of the objectives is to track a rectified sinusoidal signal, one could propose to utilize a proportional-resonant class of controllers in order to attain zero steady state error. While this is reasonable, this controller class ends up introducing two zeros, turning the task of proposing a reachable reference model more complex. Relaxing the control objective to only seek for a finite low steady-state error, the simpler Proportional Integral (PI) class ends up being more suitable option (Pandey; Singh, 2019; Belkamel; Kim; Choi, 2020). As the objective is to track a low frequency reference composed of 60 Hz and its harmonics, good performance for the control loop can be achieved with a large open-loop gain up to a certain frequency f_{bi}, which denotes the bandwidth of the current loop. This can be achieved by the integral action, which boosts the gain of the system at lower frequencies.

The same PI class of controllers is suitable for the voltage loop for the same reasons. Furthermore, when the input current of a controlled rectifier is sinusoidal, the instantaneous input power signal becomes a pulsed waveform, while the instantaneous output power is approximately DC with a resistive load. As a consequence, the difference between the instantaneous input and load powers flows through the output capacitor, causing an oscillation in the output voltage signal at twice the frequency of the input current (Erickson; Maksimovic, 2020). Such oscillation is expected, thus the voltage loop should not try to reject it. To this end, a low bandwidth in the voltage loop is often forced, with the limitation of a slow response against load or input voltage variations. Apart from this, there are desirable stability properties in the VRFT formulation that can be achieved if this class of controllers is utilized for the external loop. These properties are discussed in Section 4.4.

In the discrete-time domain, the PI class is represented the space of functions

$$\mathscr{C}_{\text{PI}}(z,\rho) = \left\{ \begin{bmatrix} k_p & k_i \end{bmatrix} \begin{bmatrix} 1 \\ \frac{z}{z-1} \end{bmatrix}, \begin{bmatrix} k_p & k_i \end{bmatrix} \in \mathbb{R}^2 \right\}, \tag{4.1}$$

where $\rho = \begin{bmatrix} k_p & k_i \end{bmatrix}$ in this case.

4.2 REFERENCE MODELS

In the MRC sense, the reference model should encompass the control objectives in the form of an achievable closed-loop transfer function. One requirement for the VRFT algorithm to result in an ideal causal controller is that the relative degree of the reference model, i.e., the order of the denominator minus the order of the numerator, should be higher or equal than the relative degree of the process (Bazanella; Campestrini; Eckhard, 2011; Remes et al., 2021). To comply with this restriction, the well-known models in the literature for $G_i(z)$ and $G_e(z)$ in the boost PFC converter are used to extract such information.

With that, in CCM, the discretized models of (3.16) and (3.22) are considered. It's worth remarking that, although information about the models' structure is used in this section, no knowledge of the converter's parameters is required in the final formulation. In other words, only the information about the space of functions that these two models can admit is required for this chapter's main results. It's also remarked that the model in (3.22) is obtained by averaging the pertinent signals at half of the line frequency period, since the output voltage has an AC component at two times the line frequency, so it's only valid for frequencies sufficiently lower than the line frequency (Erickson; Maksimovic, 2020, p. 902).

First, regarding the internal current loop, initially considering the simplest possible reference model, which would be a first order model in this case, the normal behavior for VRFT with controllers of the PI class is that the controller's zeros cancel with the plant's poles, so that the tuning of the controller's gain and the action of the integrator end up shaping the loop according to a desired reference model (Remes et al., 2020). However, in this case the plant already has an integrator according to (3.16), which would result in the controller's zero to be tuned around $z = 1$, which isn't appropriate for stability reasons. So, in order to propose an achievable reference model, the structure of the resulting closed-loop system when using a PI controller in the direct feedback path is expressed in sequence, so as to determine a suitable transfer function structure for the internal reference model. With that, let $C_i(z,\rho_i) = K_{Ci} \cdot (z - z_{Ci})/(z-1)$, where $K_{Ci} \in \mathbb{R}$ and $z_{Ci} \in (0,1)$. Then, denoting the open-loop transfer function of the inner subsystem by $L_i(z) = G_i(z)C_i(z,\rho_i)$, the closed-loop transfer function takes the form of

$$T_{di}(z) = \frac{\text{num}\{L_i\}}{\text{den}\{L_i\} + \text{num}\{L_i\}} \tag{4.2}$$

$$\rightarrow T_{di}(z) = K_{Tdi} \cdot \frac{z - z_{Ci}}{z^2 + c_{i1}z + c_{i0}}, \tag{4.3}$$

where the zero of the controller carries on to the closed-loop transfer function, $K_{Tdi} = K_{Ci}K_{Gi}$, $c_{i1} = -2 + K_{Tdi}$ and $c_{i0} = 1 - K_{Tdi}\,z_{Ci}$. In fact, the zero z_{Ci} and the coefficients c_{i1}, c_{i0} can be constrained by the relationship $z_{Ci} = (1 - c_{i0})/(c_{i1} + 2)$. It's also noticeable that the zero in $T_{di}(z)$ is the same of the controller $C_i(z, \rho_i)$, which would imply that one of the parameters that are to be identified should already be known. However, it's remarked that this would only be true if the model in (3.16) were perfect, when it's only an approximation and the true behavior of the rectifier's current dynamics is, in fact, nonlinear. As such, any process uncertainty contained within this disparity can move the optimal zero to a different position. In this case, the task of identifying this optimal location is given to the VRFT algorithm.

Thus, the space of functions created by every possible $T_{di}(z)$ in (4.3) is a good candidate for the reference model of the inner subsystem. To specify the coefficients of (4.3), the control objectives for the inner loop are taken into account, where it's only demanded that a bandwidth f_{bi} is achieved. The bandwidth here is defined as the frequency where the sensitivity function $S_{di}(z) = 1 - T_{di}(z)$ crosses $1/\sqrt{2}$ from below, as recommended by Skogestad and Postlethwaite (2005). The peak of the sensitivity function $S_{di}(z)$ is also important, since it's a good metric for system's robustness (Fiorio et al., 2021). Since the gain K_{Tdi} will always ensure that $T_{di}(1) = 1$, because of the integrators in the system, and there is a relation between z_{Ci}, c_{i0} and c_{i1}, only these two last parameters need to be chosen.

To this end, it's possible to numerically verify the two properties of interest for several $T_{di}(z)$ respecting (4.3) (Kupas, 2022). In addition, the additional condition $0 < z_{Ci} < 1$ should be followed, to guarantee that the controller $C_i(z, \rho_i)$ does not contain an unstable zero. Substituting this inequality in the relation for z_{Ci} yields the conditions

$$c_{i0} < 1, \tag{4.4}$$

$$c_{i1} > -1 - c_{i0}. \tag{4.5}$$

With these restraints, Figure 11 shows that there is a bandwidth Ω_{bi} (normalized from 0 to 1) for the closed-loop response, which is inversely proportional to c_{i0}. Therefore, lower bandwidths are only achievable with higher values for c_{i0}. However, it's also clear that $\|S_{di}\|_\infty$, which is a robustness metric to be kept as low as possible (Skogestad; Postlethwaite, 2005), is inversely proportional to c_{i0} for any value of c_{i1}. Because of this, the following procedure can be taken to maximize the robustness of the reference model:

1. Given Ω_{bi}, select the lowest value of c_{i0} which is capable of achieving it;
2. Then, select the corresponding value of c_{i1} to yield the desired bandwidth;
3. Calculate the associate zero z_{Ci} according to $z_{Ci} = (1 - c_{i0})/(c_{i1} + 2)$;
4. Finally, the reference model should have unitary DC gain, so choose $K_{Tdi} = (1 + c_{i1} + c_{i0})/(1 - z_{Ci})$.

Figure 11 – Peak of S_{di} and normalized bandwidth as a function of c_{i0}, c_{i1}.

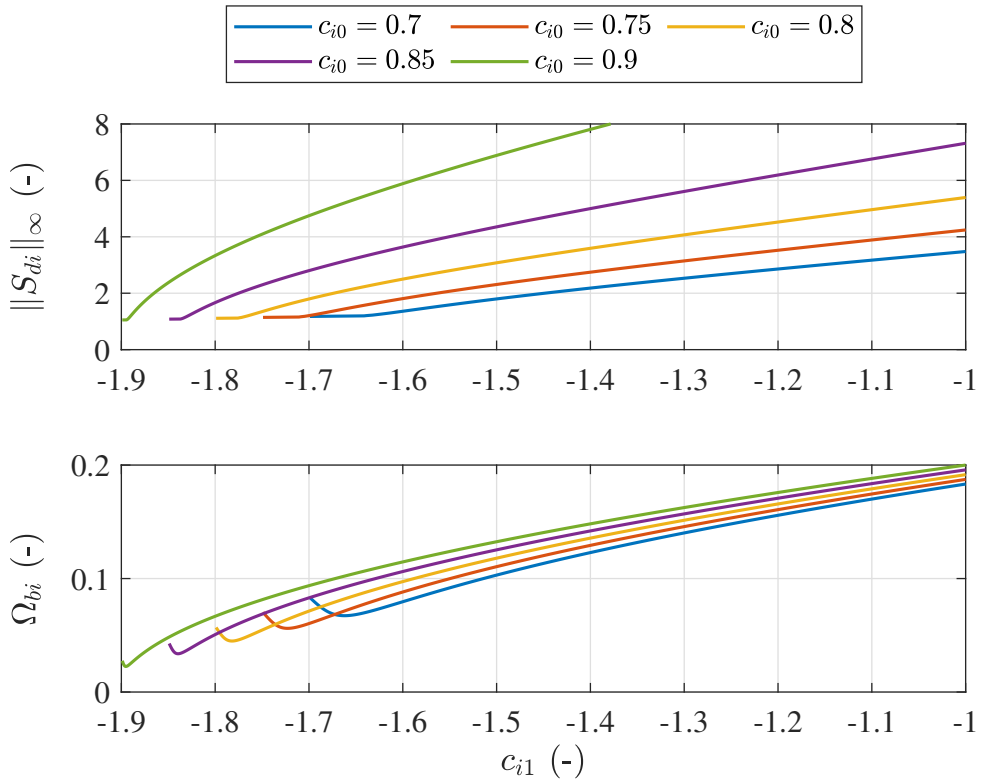

Source: the author (2025).

For the external loop, since the expected behavior for the plant is a 1st order system, VRFT can be employed as recommended by Remes et al. (2021). As such, the reference model's relative degree must be higher or equal than the order of $G_e(z)$, denoted by $\Gamma\{G_e(z)\}$. Since $\Gamma\{G_e(z)\} = 1$, then it follows that $\Gamma\{T_{de}\} = 1$ as well. As such, the simplest reference model that can be used is given by

$$T_{de}(z) = K_{Tde} \cdot \frac{1}{(z - p_{e1})}, \tag{4.6}$$

where p_{e1} is the dominant pole and the gain $K_{Tde} = (1 - p_{e1})$ ensures unitary DC gain. Regarding the oscillation at twice the line frequency in the output voltage signal, there are many ways to deal with this issue, but the simplest method is to reduce the bandwidth of external loop, so that these oscillations are mostly ignored. This also goes along with the operating point analysis for robustness done in Section 4.4. To this end, the control objective for the external voltage control loop is to ensure a low bandwidth so that the output voltage oscillation at twice the line frequency does not distort the current reference. Let f_{be} be the desired bandwidth in Hz. With that, iterating through every stable value of $p_{e1} \in (0,\ 1)$ yields the results of Figure 12, which shows the peak of the associated sensitivity function $S_{de}(z) = 1 - T_{de}(z)$ and the normalized bandwidth $\Omega_{be} = f_{be}/(f_s/2)$. A zoom for $\Omega_{be} < 1{\cdot}10^{-3}$ is also shown, as it's common for the outer loop to be designed to a much lower bandwidth than the switching frequency, which is often the sampling frequency. In conclusion, the following procedure can then be taken to choose

the reference model:

1. Given Ω_{be}, select the corresponding value of p_{e1}.
2. Calculate the gain of the reference model to ensure unitary DC gain, i.e., $K_{Tde} = (1 - p_{e1})$.

Figure 12 – Peak of S_{de} and normalized bandwidth as a function of p_{e1}.

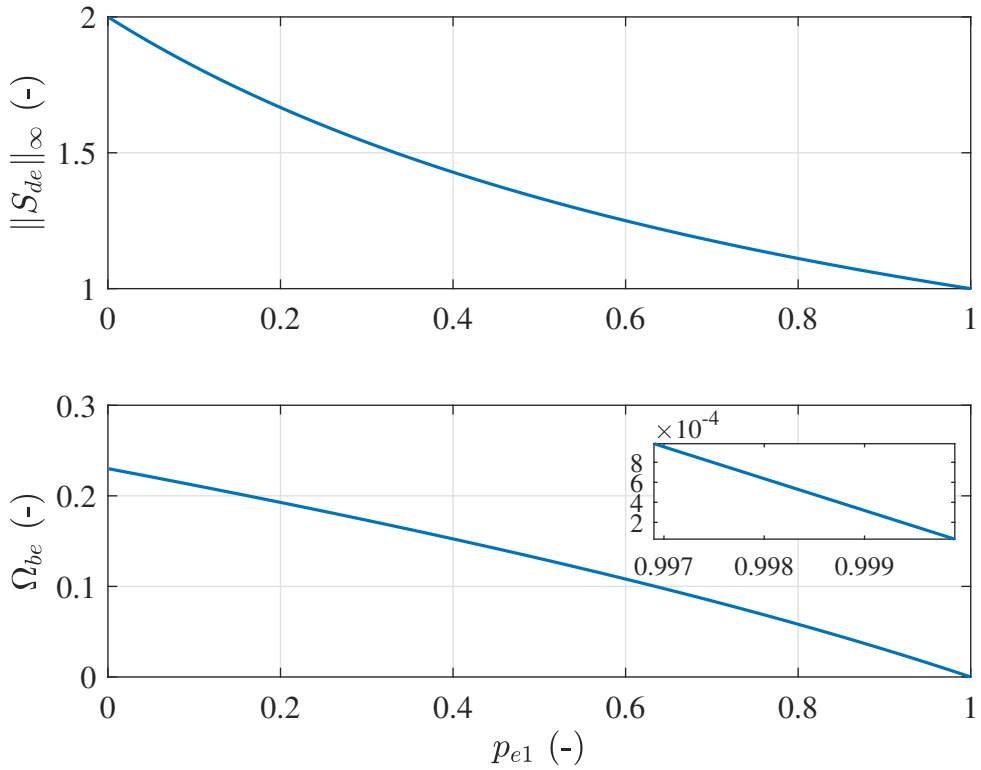

Source: the author (2025).

4.3 DATA COLLECTION

In order to estimate optimal controllers in the MRC sense, data which represents well the behavior of the system needs to be collected. In the considered cascade system structure, this demands the collection of both the internal and external outputs $y_i = |i_L|, y_e = v_o$, as well as the output of both controllers $u_i = d$ and u_e. However, since the normal operation mode for boost PFC rectifiers has these variables following a time-varying trajectory, e.g., i_L follows a sinusoidal shape, data can't be collected around a DC operational point such as in the works of Remes et al. (2021).

In short, it's required to observe the small-signal variations around the signals' nominal trajectories. The trajectories of interest are denoted by $\begin{bmatrix} i_L^* & v_o^* \end{bmatrix}^T = \begin{bmatrix} I_{L,p}|\sin(\theta)| & V_o \end{bmatrix}^T$, where $I_{L,p}$ is the expected peak input current for at a certain load, $\sin\theta$ is synchronized with the input voltage and V_o is the desired output voltage. Although it's known that the behavior of a nonlinear system linearized around a trajectory is LTV, it's assumed that the variations of $\begin{bmatrix} i_L & v_o \end{bmatrix}^T$ around

this specific trajectory are linear enough in order to enable the use of VRFT. In other words, it's proposed to use the set of signals $\{\Delta u_i(k), \Delta u_e(k), \Delta y_i(k), \Delta y_e(k)\}_{k=1}^{N}$, where

$$\Delta u_i(k) = u_i(k) - u_i^*(k), \tag{4.7}$$

$$\Delta u_e(k) = u_e(k) - u_e^*(k), \tag{4.8}$$

$$\Delta y_i(k) = y_i(k) - y_i^*(k), \tag{4.9}$$

$$\Delta y_e(k) = y_e(k) - y_e^*(k). \tag{4.10}$$

In practice, since the signals are corrupted by noise, it's required to gather a second data set that is strongly correlated with the first one, in order to enable the instrumental variable solution for VRFT. To that end, two experiments are required: one to identify $C_i(z, \rho_i)$ and a second one to identify $C_e(z, \rho_e)$. In the first experiment, the pertinent signals to be collected are the internal output and the internal control action $u_i(k) = d(k)$. In the second experiment, the external control action $u_e(k)$, according to Figure 5, and the external output $y_e(k) = v_o(k)$ are collected. All the signals are partitioned into two strongly correlated signals to enable the instrumental variable solution. Furthermore, Figure 13 illustrates the process of obtaining suitable data for an example signal $x(k)$. The procedure of Figure 13 needs to be executed two times per signal of interest, which can be done in one experiment if the same excitation signal is used two times in sequence.

To identify the internal controller, with the knowledge of the load's resistance during the data collection experiment, it's proposed to conduct an experiment where the current i_L is controlled with a proportional controller and a feedforward control term, enabling the designer to also excite system's current and gather the required variation data $\{\Delta u_i(k), \Delta y_i(k)\}_{k=1}^{N}$. To identify the external controller, since the nominal trajectory for the external output oscillates around a constant value V_o, it's easier to conduct the second experiment in an open-loop fashion to collect the data $\{\Delta u_e(k), \Delta y_e(k)\}_{k=1}^{N}$. The two experiments are detailed in sequence.

4.3.1 Internal data-collection experiment

In order perform the experiment, the converter must be driven to its operating point. Since initially no internal controller is available to regulate the inductor's current, it's proposed to utilize a proportional controller added to a feedforward term than can be calculated with no knowledge of the converter's parameters, relying only on the operating point of the converter, i.e., the input voltage and desired output voltage. Regarding the choice for the proportional gain, any proportional controller k_p is locally stable to a system which is only composed of an integrator and a DC gain. Since that's the case of the current model (3.15), the controlled current loop is stable as long as no nonlinearities start to affect the system. Considering the saturation of the control action, in this case the duty-cycle $d(k)$, which is limited to the interval $[0, D_{\max}]$, $D_{\max} \in (0,1)$, it's possible to choose an appropriate value for k_p, so that the current reference r_{iL} is followed without causing the saturation of $d(k)$.

Figure 13 – Illustration for collecting signal $\Delta x(k)$ for VRFT.

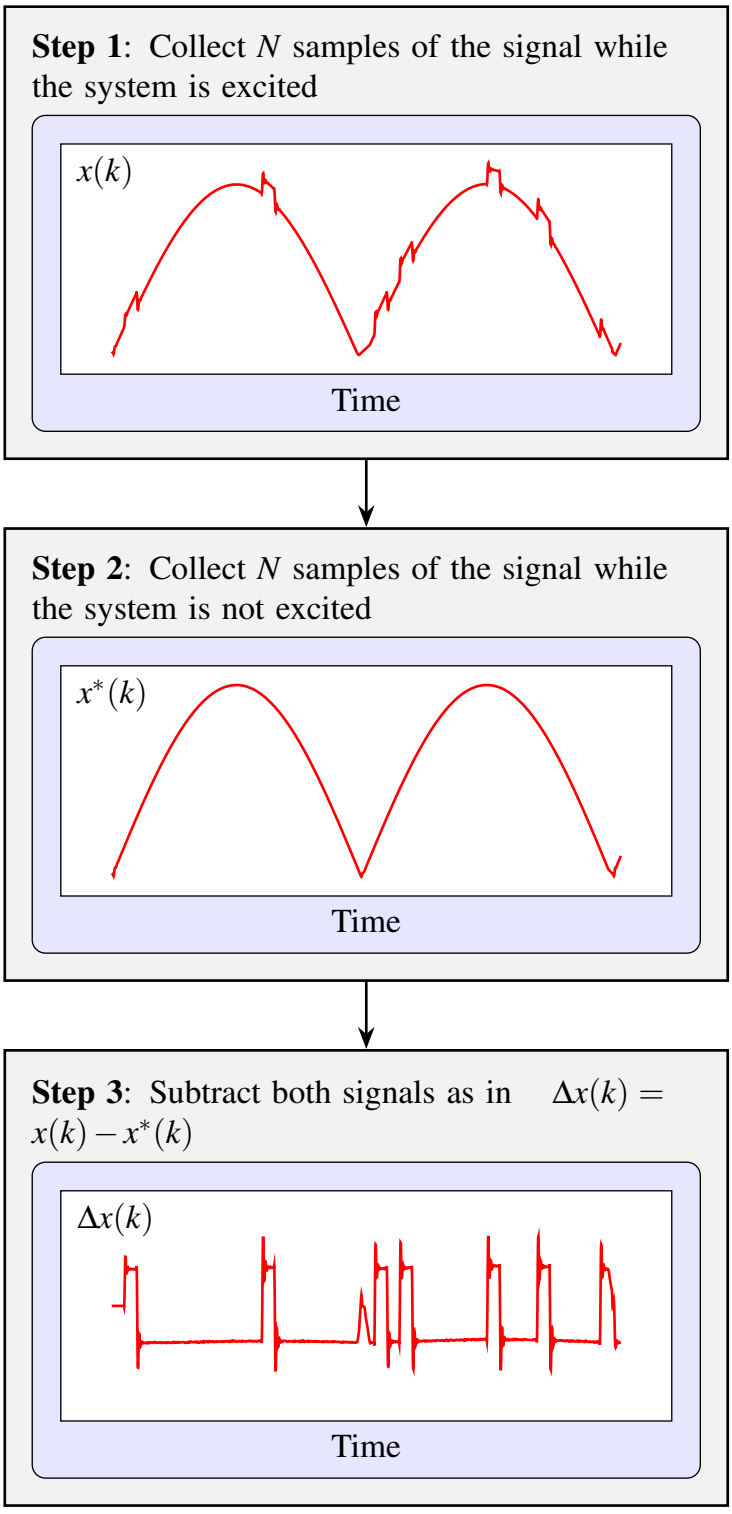

Source: the author (2025).

Considering the power balance of the converter and disregarding losses, i.e., $v_{in}(t)i_{in}(t) =$

$v_o(t)i_o(t)$, the current reference for the experiment is given by

$$r_{iL} = I_{in,pk}|\cos(\theta)| + \Delta r_{iL}, \tag{4.11}$$

$$I_{in,pk} = \frac{2P_o}{V_{in,pk}}, \tag{4.12}$$

where $I_{in,pk}$ is the expected peak input current, P_o is the output power, Δr_{iL} is the identification signal which excites the converter's behavior around its nominal trajectory, $V_{in,pk}$ is the peak line voltage and $\cos(\theta)$ is synchronized with its angle. A PLL is recommended to generate this last term. The identification signal Δr_{iL} should guarantee persistence of excitation[1], which is feasible with signals such as square waves or a Pseudo-Random Binary Signal (PRBS). It's remarked that Δr_{iL} should be partitioned into two identical sequences, in order to enable the collection of instrumental variables.

A feedforward term can be implemented to compensate for the effects of the input voltage on the input current, making it easier to obtain an approximately sinusoidal current signal. Indeed, in CCM, the input voltage $v_g(t) = |v_{in}(t)|$ affects the input current $i_g(t) = |i_L(t)|$ approximately according to the differential equation (Erickson; Maksimovic, 2020, p. 885)

$$L_b \frac{d\langle i_g(t)\rangle_{T_s}}{dt} = \langle v_g(t)\rangle_{T_s} + (d(t) - 1)V_o, \tag{4.13}$$

where $\langle i_g(t)\rangle_{T_s}$ and $\langle v_g(t)\rangle_{T_s}$ are the average absolute input current and voltage in a switching cycle T_s, and V_o is the average DC output voltage. As such, the feedforward term can be proposed to cancel the effects of $\langle i_g(t)\rangle_{T_s}$ and $\langle v_g(t)\rangle_{T_s}$ on the differential equation above. In this case, let

$$d_{ff}(t) = 1 - \frac{|v_{in}(t)|}{V_o}. \tag{4.14}$$

If $d(t) = d_{ff}(t) + u_i(t)$ then the dynamics of (4.13) simplify to

$$L_b \frac{d\langle i_g(t)\rangle_{T_s}}{dt} = u_i(t)V_o, \tag{4.15}$$

where $u_i(t) = k_p(r_{iL} - |i_L(t)|)$. By taking this approach, the proportional controller doesn't need to compensate for disturbances in $v_g(t)$ in this case.

It's remarked that the choice of proportional gain k_p for data-collection is fundamental for a successful experiment. To this end, any k_p that doesn't make the final duty-cycle $d(t)$ go into saturation is stabilizing for the plant of (3.15). Therefore, k_p can be limited by stipulating a maximum output control action $u_i(t)$, which is then added to the feedforward term. Since the maximum of (4.14) is one when $v_{in} = 0$, which would result in a 0 gain controller, a saturation action is imposed after the calculation of $d_{ff}(t)$, which limits the maximum feedforward term to a certain user-defined value $D_{ff,\max}$. With that, considering that the maximum error can be

[1] Persistence of excitation for VRFT is guaranteed if the input-output signals $u(k), y(k)$ present in their spectrums p or more nonzero components, where p is the number of parameters to be identified, i.e. two in the case of the PI controller class (Bazanella; Campestrini; Eckhard, 2011).

Figure 14 – Proposed procedure to drive the converter during data-collection.

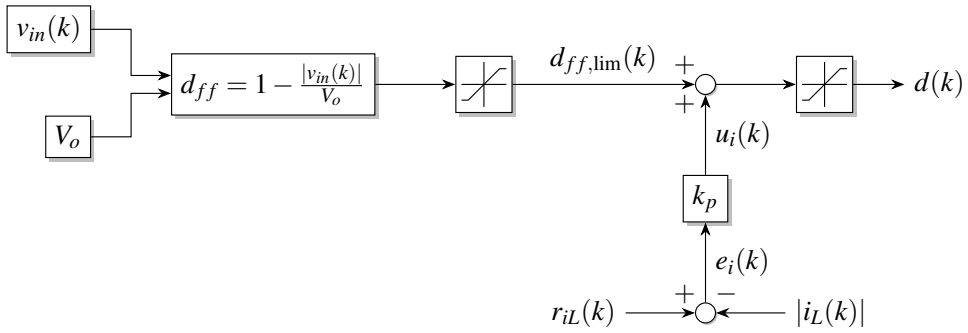

Source: the author (2025).

approximated to two times the amplitude of the identification signal Δr_{iL} (maximum allowed reference change), a maximum value for $u_i(t)$ can be approximated to $u_{i,\max} = k_p \cdot 2\Delta r_{iL,\max}$. Finally, an upper limit for k_p, in order to avoid saturation of the duty-cycle, is then given by

$$k_p \leq \frac{D_{\max} - D_{ff,\max}}{2\Delta r_{iL,\max}}, \tag{4.16}$$

where $\Delta r_{iL,\max}$ is the maximum amplitude of the current excitation signal. Naturally, $D_{ff,\max}$ should be chosen so that $D_{ff,\max} < D_{\max}$. The block diagram for the proposed experiment is shown in Figure 14.

4.3.2 External data-collection experiment

The experiment for the synthesis if $C_e(z,\rho_e)$ may be realized in open-loop because it's much easier to drive the output voltage signal around a DC level. In this way, by setting the external control action to $u_e(k) = U_e + \Delta u_e(k)$, where $U_e = I_{in,pk}$, as defined in (4.12), and $\Delta u_e(k)$ is an identification signal, which may also be a PRBS. Correspondingly, Δu_e should again be partitioned into two identical sequences. Exciting the system this way and with the already identified internal controller enables the designer to drive the system to its operating region and collect suitable data $\{\Delta u_e(k), \Delta y_e(k)\}_{k=1}^{N}$ to identify $C_e(z,\rho_e)$.

4.4 OPERATING POINT FOR STABILITY GUARANTEES

In this section, assertions about the effects of the operating region in which data was collected on the stability and robustness property of the closed-loop system are investigated. The operating region here consists of the variations on the peak value of the input voltage and on the load power, both of which are contained in known intervals, i.e., $V_{in,pk} \in [V_{in,pk}^{-}, V_{in,pk}^{+}]$ and $P_o \in [P_o^{-}, P_o^{+}]$. A "worst-case" situation is particularly attractive to identify where, if the designed controller manages to stabilize the system, then it also stabilizes every other system considering variations in $\{V_{in,pk}, P_o\}$. Here, the models' structures of (3.16) and (3.22) are utilized again, however these are not used in any way in the VRFT algorithm, so the method still remains data-driven. Instead, they are only used in order to derive the worst-case conditions of interest.

Regarding other forms of uncertainty, such as robustness to noise and multiplicative uncertainty, those can be mitigated with a proper choice of reference models, preferably ensuring that the maximum peak of the sensitivity function $\|S_d(z)\|_\infty = \|1 - T_d(z)\|_\infty$ is lower than 2 (Skogestad; Postlethwaite, 2005). It's worth reinforcing that the VRFT method doesn't guarantee a bound on this metric by default, so if a hard limit on $\|S(z)\|_\infty$ is desired, the VRFT extension of Fiorio et al. (2021) could be utilized in order to obtain a controller which respects an estimation of it, at the cost of a harder problem to optimize.

First the internal current loop is discussed. A possible way to approach the problem is to analyze the simplified model for the internal subsystem $G_i(s)$ in (3.15), which is valid as long as the variations around the nominal average output voltage are much smaller that it, i.e., if $\bar{v}_o(t) = V_o + \hat{v}_o(t)$ is the averaged output voltage, then $\hat{v}_o \ll V_o$ (Erickson; Maksimovic, 2020, p. 885). Since this model doesn't depend on the input voltage or load power, then if a controller $C_i(z, \rho_i)$ manages to stabilize the current for a certain point $\{V_{in,pk}, P_o\}$, then this also applies to every other point as long as the model is valid. A clear requisite for this is to always maintain CCM operation, but other than that, there is no specific value for $\{V_{in,pk}, P_o\}$ in order to design a data-collection experiment. It's remarked as well that, since this model is an approximation, at best only local stability around the steady-state trajectories can be guaranteed.

According to the simplified model $G_i(s)$, there are no restrictions imposed by the current subsystem. Next, the external subsystem $G_e(s)$ of (3.20) is studied, which can also be written as

$$G_e(s) = \frac{R_o V_{in,pk}}{4V_o} \frac{1}{1 + 0.5 R_o C_o s}, \tag{4.17}$$

where R_o is the equivalent load resistance, C_o is the output capacitance (Pereira et al., 2021; Erickson; Maksimovic, 2020). A limitation of this simple linear model is that it's only valid to frequencies much lower than the line frequency, so this analysis is limited to external reference models $T_{de}(z)$ of low bandwidth. Moreover, the case without a varying gain to compensate for different input voltage peaks is considered for simplicity. Therefore, considering the structure of Figure 4, the outer loop transfer function at a certain point $\{V_{in,pk}, R_o\}$ can be expressed as

$$L_e(s) = C_e(s) T_i(s) \frac{R_o V_{in,pk}}{4V_o} \frac{1}{1 + 0.5 R_o C_o s}, \tag{4.18}$$

where $T_i(s)$ is the equivalent closed-loop transfer function of the internal subsystem. Next it's verified the effects of the operating point for the data-collection experiment on the phase and gain margins of the closed loop external subsystem. To this end, two cases are considered: $\{V_{in,pk}^{(0)}, R_o^{(0)}\}$ where the data-collection was realized and another case $\{V_{in,pk}^{(1)}, R_o^{(1)}\}$ representing any other point.

Consider as well that $C_e(s)$ is in the PI class, as discussed in Section 4.1. In the ideal case VRFT should aim to cancel the pole of $G_e(s)$, so its structure can be proposed as

$$C_e(s) = K_0 \cdot \frac{1 + 0.5 R_o C_o s}{s}, \tag{4.19}$$

where the gain K_0 is directly related to the reference model $T_{de}(s)$. Moreover, the system's loop transfer function in the two considered cases can be expressed by

$$L_e^{(0)}(s) = T_i(s)K_0\frac{R_o^{(0)}V_{in,pk}^{(0)}}{4V_o}\cdot\frac{1}{s}, \tag{4.20}$$

$$L_e^{(1)}(s) = T_i(s)K_0\frac{R_o^{(1)}V_{in,pk}^{(1)}}{4V_o}\cdot\frac{1}{s}\cdot\frac{1+0.5R_o^{(0)}C_os}{1+0.5R_o^{(1)}C_os}. \tag{4.21}$$

By noting that, if $L_e^{(1)}(s)$ has more phase and gain margins than $L_e^{(0)}(s)$, then the case 0 corresponds to the "worst-case" operating point of interest. In order for this to be true, it is necessary and sufficient that the gain of $L_e^{(1)}(j\omega)$ is smaller than $L_e^{(0)}(j\omega)$ at every frequency ω; and it's also necessary that the phase of $L_e^{(1)}(j\omega)$ is higher than the phase of $L_e^{(0)}(j\omega)$ at every frequency. In other words, if the conditions

$$|L_e^{(1)}(j\omega)| < |L_e^{(0)}(j\omega)|,\ \forall\omega, \tag{4.22}$$

$$\angle L_e^{(1)}(j\omega) > \angle L_e^{(0)}(j\omega),\ \forall\omega, \tag{4.23}$$

are true, then it's possible to collect data at the point $\{V_{in,pk}^{(0)}, R_o^{(0)}\}$, so that the system remains stable and present more gain and phase margins at any other point of operation. Condition (4.23) is met if $R_o^{(0)} > R_o^{(1)}$, whereas the requirement (4.22) is met if $V_{in,pk}^{(1)} < V_{in,pk}^{(0)}$. To illustrate, Figure 15 presents an example of $L_e^{(0)}(s)$ and $L_e^{(1)}(s)$ when the above conditions are met.

Figure 15 – Example of two outer loop transfer functions $L_e^{(0)}(s)$ and $L_e^{(1)}(s)$.

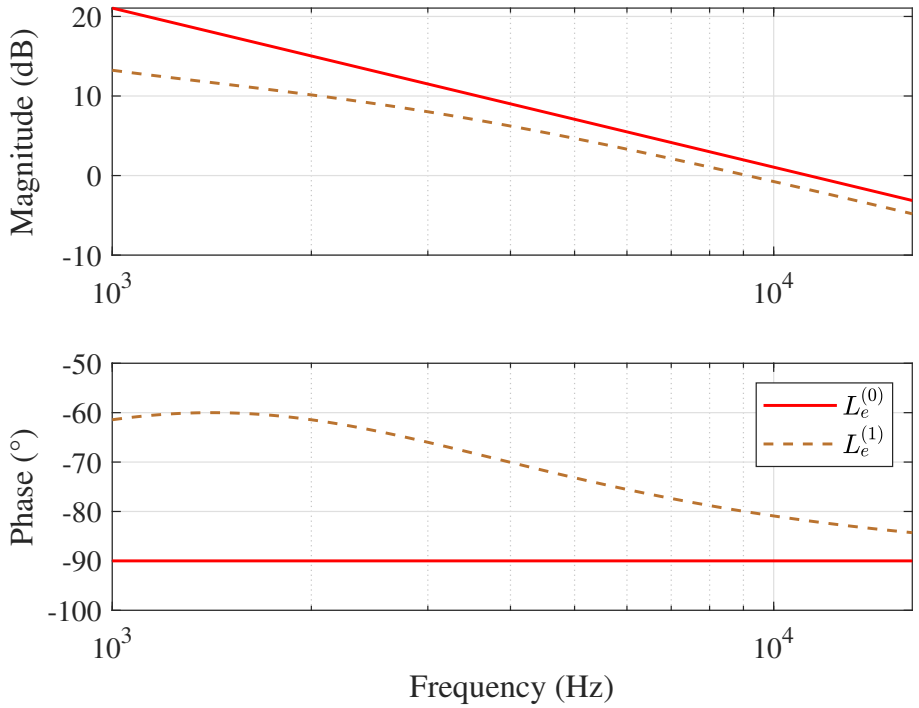

Source: the author (2025).

Finally, it's concluded through this analysis, that if the data-collection experiment is done with the minimum load (equivalently the maximum value of R_o) and maximum input voltage and results in a stable controller, then this controller also stabilizes the system at any other operating point $\{V_{in,pk}, R_o\}$, resulting in more phase and gain margins in those cases as well. It's reinforced that this is only true if $T_{de}(s)$ has a bandwidth much lower than the line frequency.

4.5 SUMMARY OF THE DESIGN PROCESS

The step-by-step procedure of the experiment is summed up below:

1. Define the amplitude of the identification signal Δr_{iL}, its frequency and the proportional controller k_p according to Sec. 4.3.

2. Drive the converter with $\Delta r_{i_L} = 0$ to collect the data $\{d(k), |i_L(k)|\}_{k=1}^{N}$, where the instant $k = 1$ corresponds to a specific line voltage value, e.g., the zero crossing point. Two sets of nominal trajectories are demanded, so this step needs to be executed twice, or equivalently a single dataset obtained from a single experiment can be divided into two partitions.

3. Repeat the previous step, but with Δr_{iL} being a nonzero identification signal, two more times in order to gather all the required signals. Δr_{iL} should be the same signal in all cases. This step may be repeated more times if there is too much noise present in the data, where averaging multiple datasets is recommended before applying the IV solution of VRFT.

4. Define the reference model $T_{di}(z)$ according to Sec. 4.2. Then calculate the filter $L_i(z) = T_{di}(z)[1 - T_{di}(z)]$.

5. Use the least-squares instrumental variable solution (2.13) with $y'_L(k) = L_i(z)\Delta i'_L(k)$, $y_L(k) = L_i(z)\Delta i_L(k)$ and $u_L(k) = L_i(z)\Delta d(k)$ to obtain $C_i(z, \hat{\rho}_i) \in \mathscr{C}_{\text{PI}}$.

6. Define the amplitude and frequency of Δu_e according to Sec. 4.3.2.

7. Drive the converter with the with $\Delta u_e = 0$ to collect the data $\{u_e(k), v_o(k)\}_{k=1}^{N}$, where the instant $k = 1$ corresponds to a specific line voltage value, e.g., the zero crossing point. Two sets of nominal trajectories are demanded, so this step needs to be executed twice, or equivalently a single dataset obtained from a single experiment can be divided into two partitions.

8. Repeat the previous step, but with Δu_e being a nonzero identification signal, two more times in order to gather all the required signals. Δu_e should be the same signal in all cases. This step may be repeated more times if there is too much noise present in the data, where averaging multiple datasets is recommended before applying the IV solution of VRFT.

9. Define the reference model $T_{de}(z)$ according to subsection 4.2. Then calculate the filter $L_e(z) = T_{de}(z)[1 - T_{de}(z)]$.

10. Apply again the least-squares solution (2.13), but with $y'_L(k) = L_e(z)\Delta v'_o(k)$, $y_L(k) = L_e(z)\Delta v_o(k)$ and $u_L(k) = L_e(z)\Delta u_e(k)$ to obtain $C_e(z,\hat{\rho}_e) \in \mathscr{C}_{\text{PI}}$.

4.6 FINAL CONSIDERATIONS

This chapter specified how to apply the DDC method VRFT in order to tune two controllers in a cascade system for PFC rectifiers in general. Guidelines concerning the data-collection, choice of reference models and controller classes were given. Furthermore, the operating point for prioritizing robustness was also specified. The next chapters contain examples of application of the proposed method.

5 SIMULATION RESULTS

A simulation case study is shown next, where the proposed method is applied to a bridgeless totem-pole boost PFC rectifier. The control scheme is the same one of Figure 8, with the assumption that the sensors H_{vo}, H_i and H_{vac} have unitary DC gain, thus the measured variables are in the same scale as the real converter's currents and voltages.

The parameters for this example are shown in Table 2. The circuit is first simulated without any noise to give an example on how to apply the proposed method. Then, different levels of noise are applied in the current measurements to verify its impact in the data-driven controller design. All simulations are realized in the software Qspice, and the digital blocks are implemented in the C++ programming language.

Table 2 – Parameters for the bridgeless totem-pole converter.

Symbol	Description	Value
$V_{ac,rms}$	Nominal rms value of AC input voltage	220 V
$V_{ac,\max}$	Maximum rms value of AC input voltage	264 V
$V_{ac,\min}$	Minimum rms value of AC input voltage	85 V
f_{ac}	Nominal line frequency	60 Hz
P_o^+	Maximum load power	300 W
P_o^-	Minimum load power	194 W
L_b	PFC inductance	3.2 mH
C_o	Rectifier output capacitance	270 μF
f_s	Switching frequency	64.8 kHz
t_d	Dead time	50 ns
V_o	Output DC voltage	380 V

Source: the author (2025).

5.1 NOISELESS CASE

First, in order to design the current controller, the procedure to drive the converter with a proportional controller is followed. In that regard, maximum values for the duty-cycle $D_{\max} = 0.9$ and feedforward term $D_{ff,\max} = 0.85$ are stipulated. While the latter can arbitrarily assume values as close to $D_{\max}$ as possible, this may result in a low k_p which is incapable of exciting the system enough to follow the experiment's current reference r_{iL}. As such, some fine-tuning may be required when proposing these duty-cycle limits.

When driving the converter with minimum power in the CCM region and maximum input voltage for maximum stability guarantees, the expected peak input current can be calculated from (4.12) and corresponds to $I_{in,pk} = 1.04\,\text{A}$. A PRBS identification signal of amplitude of approximately 20% of $I_{in,pk}$ is chosen to excite signals with a good Signal to Noise Ratio (SNR),

i.e., $\Delta r_{iL} = 0.2\,\text{A}$. Depending on the noise level, this value should be increased so that the SNR of the variation signals for VRFT is high enough. The frequency of the PRBS signal is set to 800 Hz, which is enough for the current variation signal $\Delta y_i(k)$ to reach the settling time, according to the recommendations of Ljung (1999). With that, the upper bound of (4.16) corresponds to

$$k_p \leq \frac{0.9 - 0.85}{2 \cdot 0.2} = 0.125. \tag{5.1}$$

Therefore, a stabilizing controller can be chosen as $k_p = 0.125/2$.

Afterward, the converter is driven with the minimum resistive load corresponding to P_o^- in order to collect four data sequences: $\{u^*_{i,n}(k), y^*_{i,n}(k)\}_{k=1}^N$, which are the two nominal trajectories; and $\{u_{i,n}(k), y_{i,n}(k)\}_{k=1}^N$, $n = 1, 2$, which are the trajectories with variation data, each composed of $N = 4320$ samples. These signals are presented in Figure 16. Since there is no noise, the signals for $n = 1, 2$ are overlapping, so the graph only shows the first group. By taking the difference between the signals and the nominal trajectories, the signals of Figure 17 are calculated.

Figure 16 – Internal experiment dataset for the noiseless case.

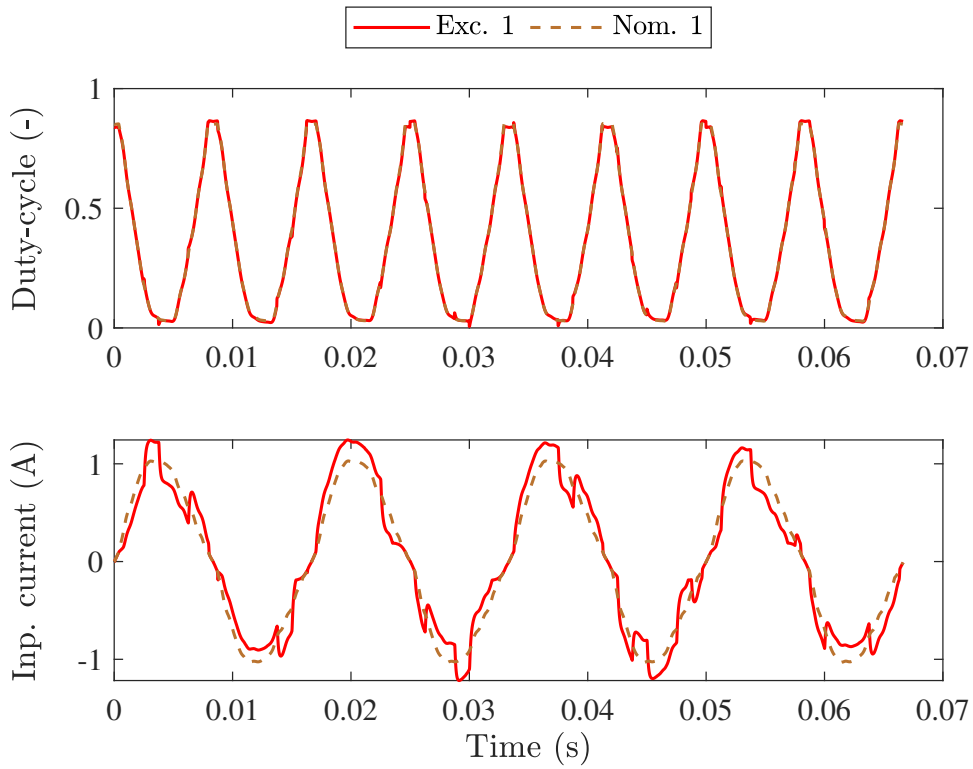

Source: the author (2025).

By selecting a bandwidth of 1.2 kHz, which is fast enough to track signals up until the 10th harmonic of a 120 Hz periodic signal, this enables the choice of $c_{i0} = 0.85$ and $c_{i1} = -1.83$ according to Figure 11. Thus, the corresponding reference model corresponds to

$$T_{di}(z) = 0.17 \cdot \frac{z - 0.88}{z^2 - 1.83z + 0.85}. \tag{5.2}$$

Using this model and the data of Figure 17 results in the internal controller

$$C_i(z,\rho_i) = 0.09416 \cdot \frac{z-0.9306}{z-1}. \tag{5.3}$$

Figure 17 – Internal experiment noiseless signals for VRFT.

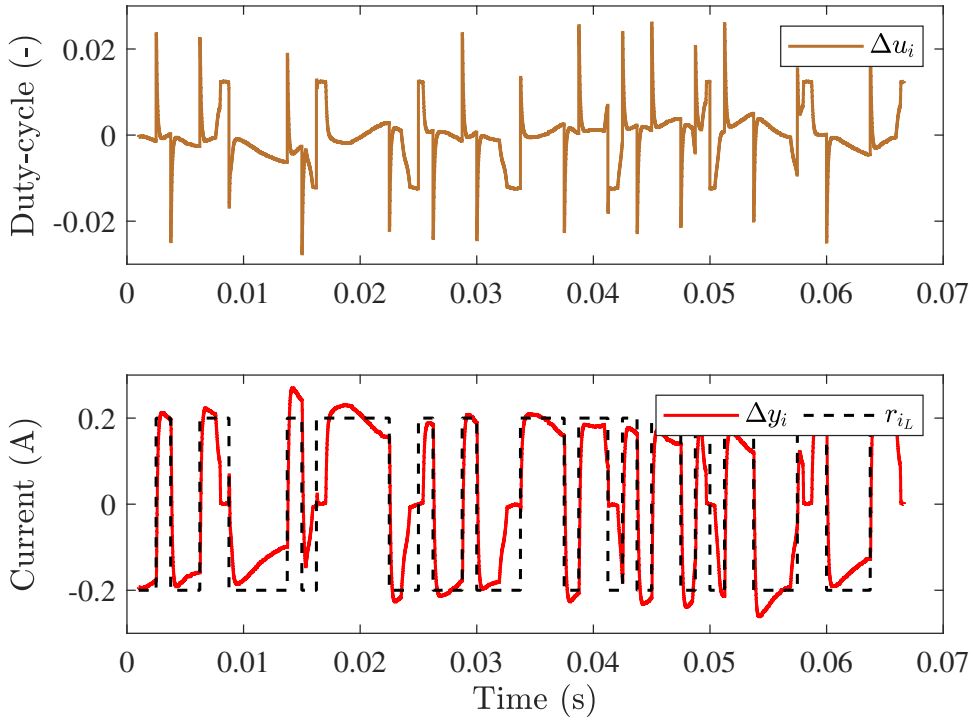

Source: the author (2025).

The next step is to conduct the external experiment in order to design $C_e(z,\rho_e)$. To excite the system, a PRBS open-loop input $\Delta u_e(k)$ with a peak of 0.2 A and frequency of 100 Hz is selected. Then, the converter is driven again with the previously obtained $C_i(z,\rho_i)$, a resistive load corresponding to P_o^- and maximum input voltage $V_{ac,\max}$, obtaining the four data sequences of Figure 18: $\{u^*_{e,n}(k), y^*_{e,n}(k)\}_{k=1}^{N}$, which are the two nominal trajectories; and $\{u_{e,n}(k), y_{e,n}(k)\}_{k=1}^{N}, n = 1,2$, which are the trajectories with variation data, each composed of $N = 43200$ samples. By taking the difference between the excited signals and the nominal trajectories, the signals of Figure 19 are calculated.

Regarding the reference model, by selecting a bandwidth of 10 Hz, which is lower than the line frequency in order to ensure stability over every operation point, the first order reference model's pole can be chosen as $p_{e1} = 0.999$ according to Figure 12, resulting in

$$T_{de}(z) = \frac{0.001}{z-0.999}. \tag{5.4}$$

Applying VRFT with the data of Figure 19 results in the controller

$$C_e(z,\rho_e) = 0.034103 \cdot \frac{z-0.9998}{z-1}. \tag{5.5}$$

Figure 18 – External experiment dataset for the noiseless case.

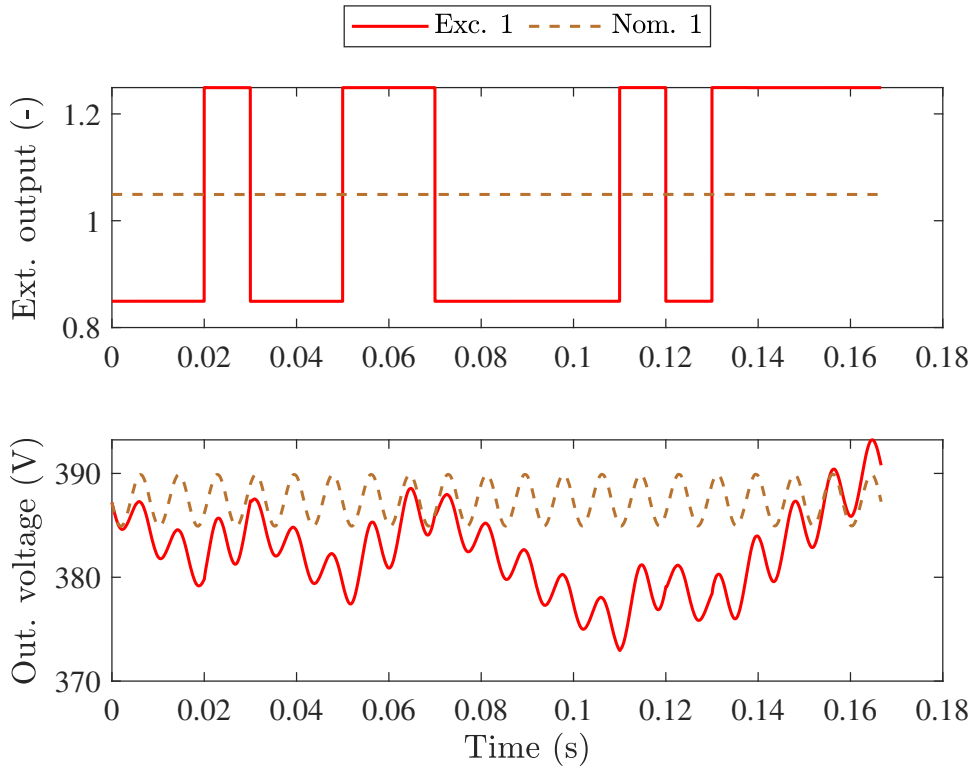

Source: the author (2025).

Figure 19 – External experiment noiseless signals for VRFT.

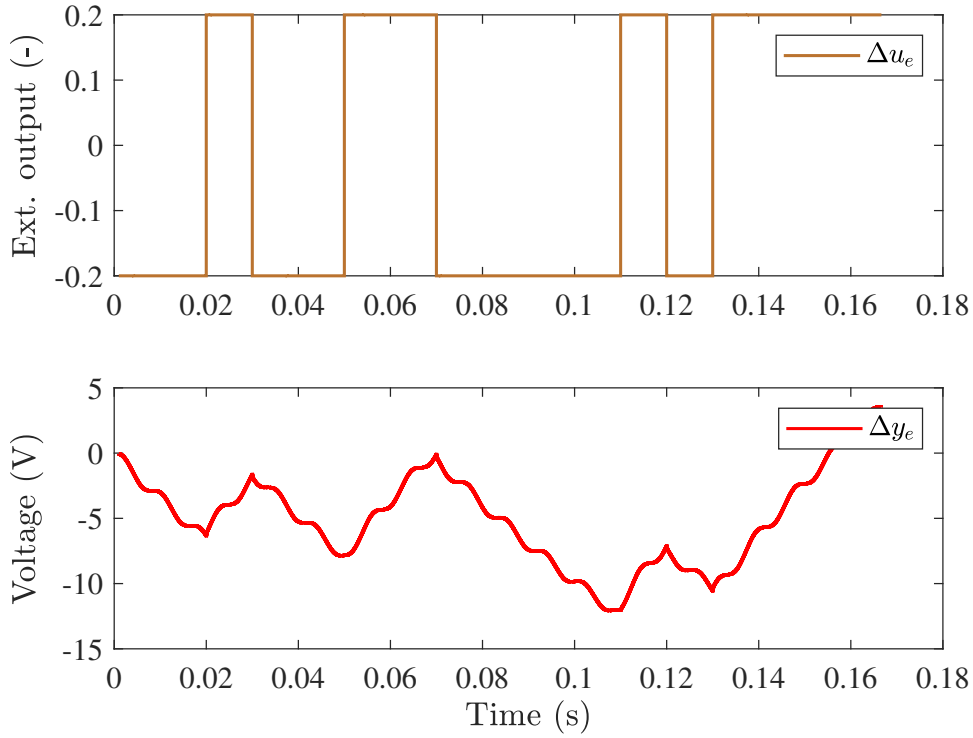

Source: the author (2025).

To illustrate that the converter can function properly with the obtained controllers, Figure 20 shows the controlled signals during nominal operation, i.e., $V_{in,rms} = 220\,\text{V}$ and $P_o = 300\,\text{W}$. It's clear that the controllers can drive the converter to its nominal point of operation as the output voltage is regulated at 380 V and the input current is near sinusoidal. The power factor is then close to unitary, being calculated as 0.9978. The response to load steps is also simulated and is shown in Figure 21, where the designed controllers manage to maintain the mean output voltage at 380 V and the input current sinusoidal. Regarding its harmonics, taking the standard IEC 61000-3-2 Class D (IEC, 2018), Figure 22 shows that the standard's requirements are easily met with the obtained controllers.

Figure 20 – Simulated closed-loop operation of the converter with $V_{in,rms} = 220\,\text{V}$ and $P_o = 300\,\text{W}$.

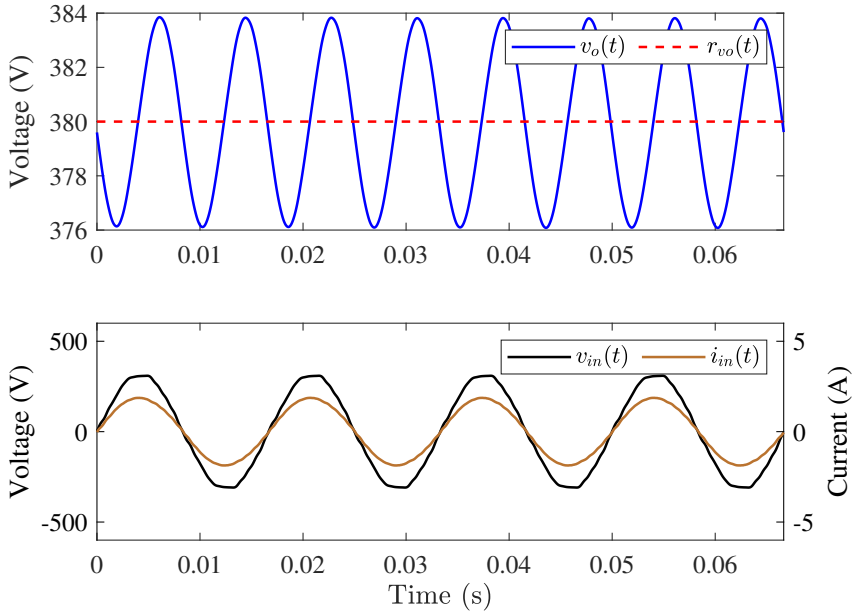

Source: the author (2025).

A quantitative comparison with a model-based design is laid out in sequence. The design is obtained using the Model-Based Frequency-Domain (MB-freq) methodology of Kazimierczuk (2015) with the discretized models (3.15) and (3.21). It's considered that the bandwidths defined before are approximately equal to the frequencies where the open-loop gain is equal to zero, which is a reasonable approximation (Skogestad; Postlethwaite, 2005). In addition, the control objectives in the frequency domain are to achieve a Gain Margin (GM) and a Phase Margin (PM) above the thresholds $\text{GM} \geq 6\,\text{dB}$ and $\text{PM} \geq 30^\circ$, which are the reference guidelines contained in the literature (Kazimierczuk, 2015). It's remarked that there is no unique solution with this methodology since multiple controllers can achieve the required GM and PM values. For this model-based design, PI controllers are considered as well, where the margin $\text{PM} = 50^\circ$ is set arbitrarily to tune the zero of $C_i(z), C_e(z)$ and the gain is adjusted to yield the required bandwidths. It's also proposed to compare the results corresponding to the controllers obtained by a Model-Based Model Reference (MB-MR) framework using the same reference models (5.2) and (5.4).

Figure 21 – Simulated load step response of the converter.

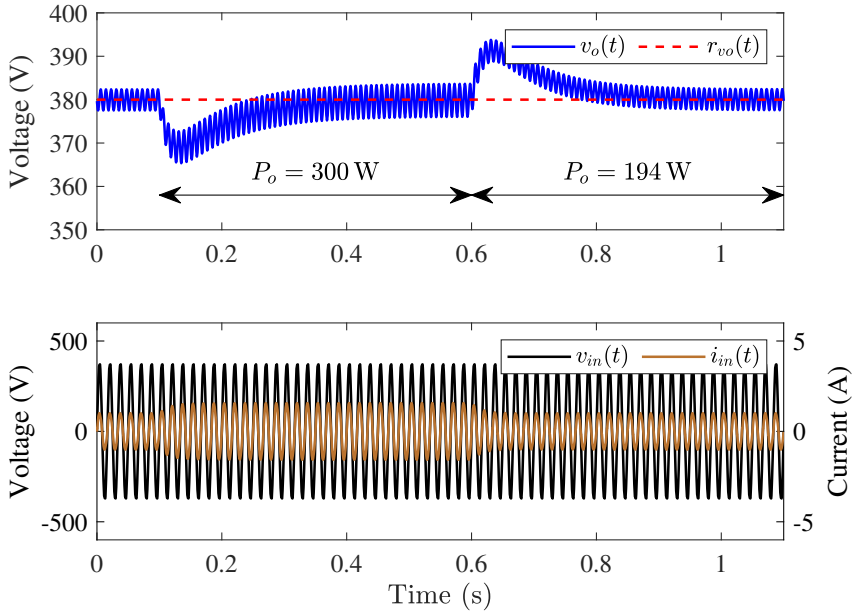

Source: the author (2025).

Figure 22 – Harmonics of the input current in nominal operation and allowed limits of IEC 61000-3-2 (Class D).

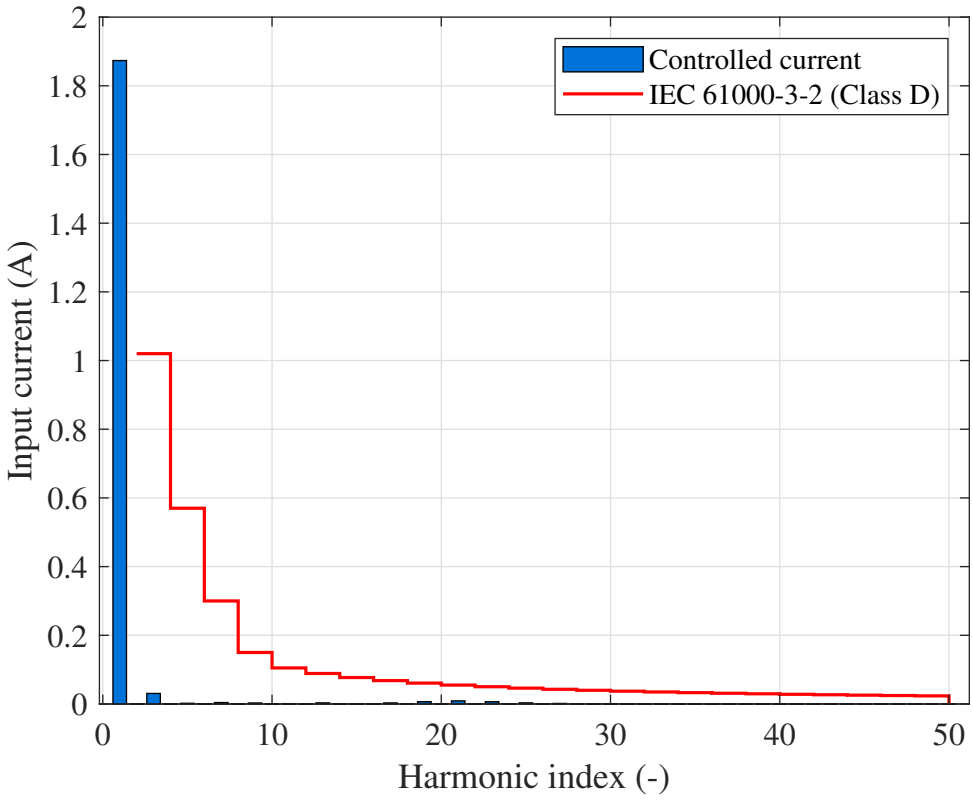

Source: the author (2025).

With these, the following model-based controllers are obtained:

$$C_{i,\mathrm{MB-freq}}(z) = 0.055011 \cdot \frac{z-0.9256}{z-1}, \tag{5.6}$$

$$C_{e,\mathrm{MB-freq}}(z) = 0.02296 \cdot \frac{z-0.9989}{z-1}. \tag{5.7}$$

$$C_{i,\mathrm{MB-MR}}(z) = 0.092766 \cdot \frac{z-0.8824}{z-1}, \tag{5.8}$$

$$C_{e,\mathrm{MB-MR}}(z) = 0.035618 \cdot \frac{z-0.9998}{z-1}. \tag{5.9}$$

The MRC performance of all controllers can be verified in the worst operating point of the converter, i.e., $V_{in,rms} = 264\,\mathrm{V}$ and $P_o = 194\,\mathrm{W}$. For the current loop, by simulating the converter with the same current reference used for data-collection, the data of Figure 23 is obtained, where it's clearly observable that the resulting simulated response matches closely the reference output $\Delta i_{L,d}(k) = T_{di}(z)\Delta r_{iL}(k)$. For the voltage loop, Figure 24 shows that VRFT yields practically the same response as the MB-MR design, which indicates that VRFT is working adequately. The same can be seen with the response to resistive load steps, which is shown in Figure 25.

For a quantitative comparison of robustness and performance, closed-loop models for both internal and external systems are identified through the estimation of the impulse response, which is obtained using the *impulseest* function/package from MATLAB (Matlab, 2020, 2021) and the data of Figs. 23 and 24. In addition, the model-reference cost $\hat{J}_{\mathrm{MR}}$ and quadratic cost J_r were estimated by

$$\hat{J}_{\mathrm{MR}} = \frac{1}{N}\sum_{k=1}^{N}\left[y(k) - T_d(z)r(k)\right]^2, \tag{5.10}$$

$$\hat{J}_r = \frac{1}{N}\sum_{k=1}^{N}\left[y(k) - r(k)\right]^2, \tag{5.11}$$

where N is the amount of samples contained in each dataset shows in the figures, $y(k)$ is the pertinent output, i.e., the absolute value of the input current or the output voltage, $r(k)$ is the pertinent reference and $T_d(z)$ is the pertinent reference model. For the external voltage system, the oscillations in 120 Hz were removed with the notch filter

$$H_{\mathrm{notch-120Hz}}(z) = \frac{0.999z^2 - 1.998z + 0.999}{z^2 - 1.998 + 0.9981}. \tag{5.12}$$

The results for both loops are summarized in Table 3. The model-reference cost for the model-based design with the frequency domain methodology was not calculated.

Figure 23 – Simulated MR performance for the current loop.

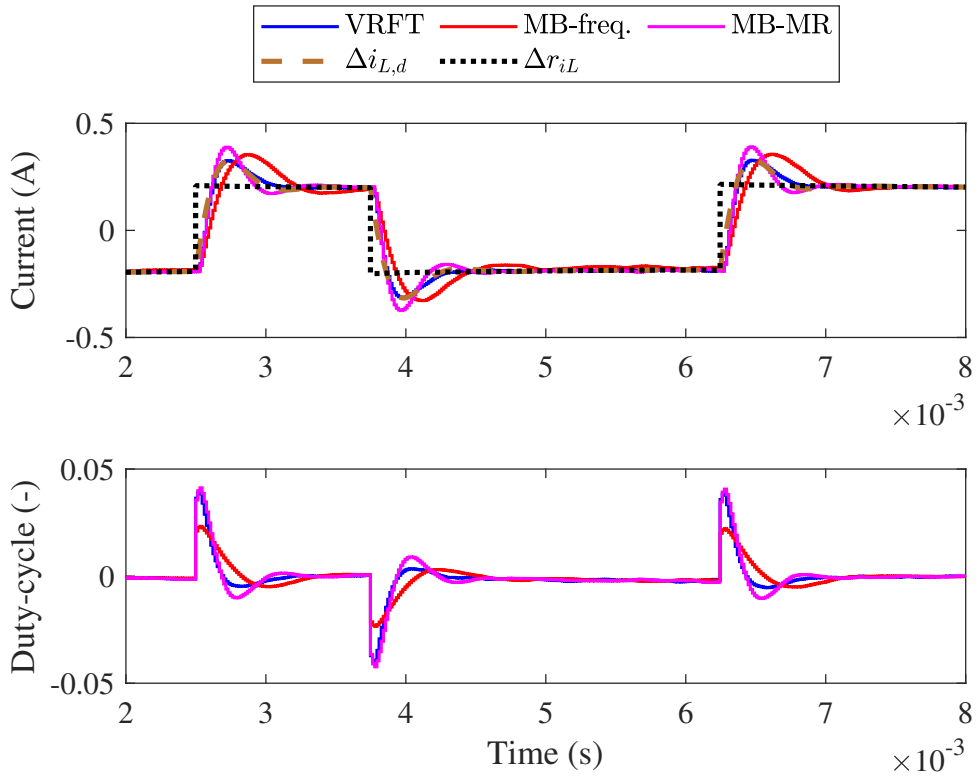

Source: the author (2025).

Figure 24 – Simulated MR performance for the voltage loop.

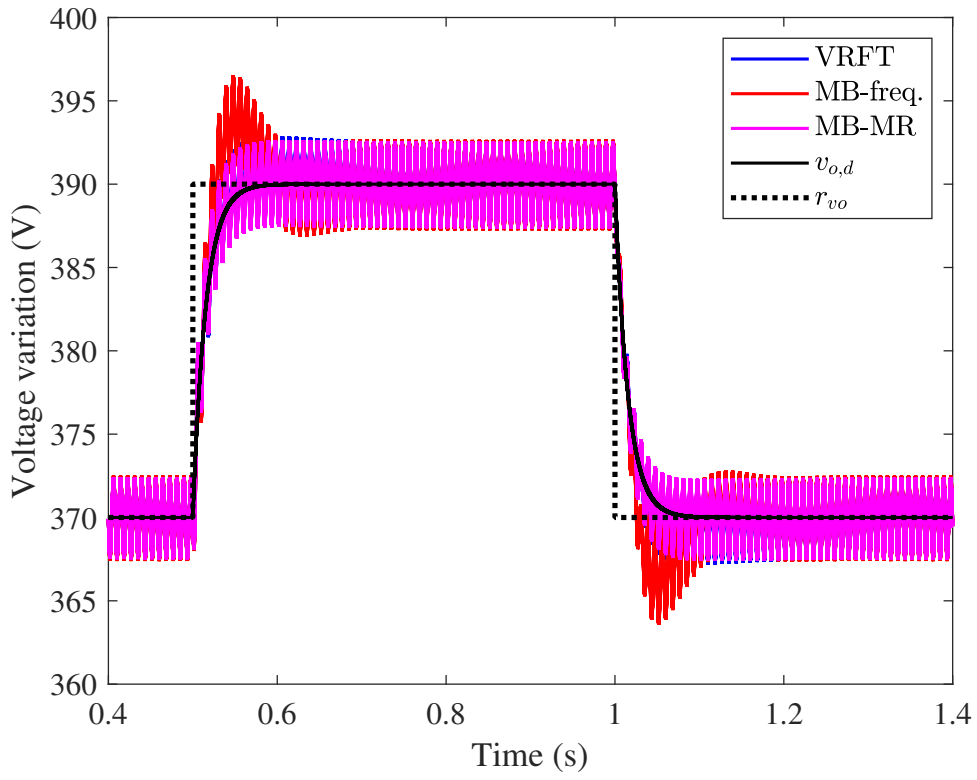

Source: the author (2025).

Figure 25 – Simulated load step response.

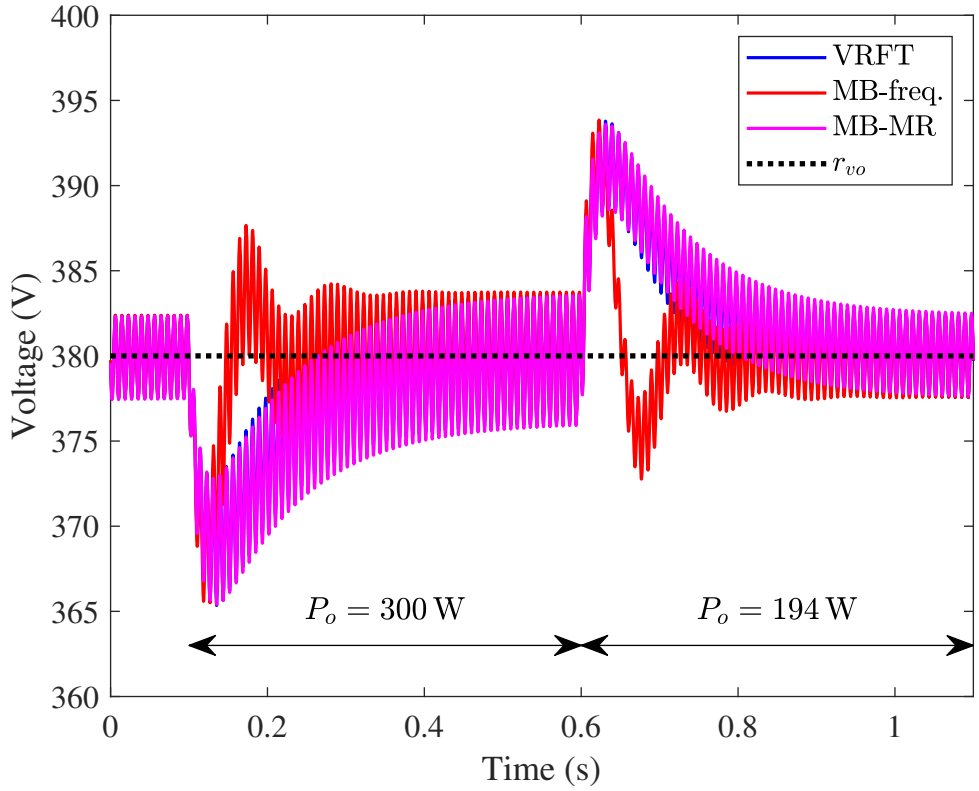

Source: the author (2025).

Considering first the model-reference cost for the current loop, these results show that the proposed data-based design does in fact perform better than the model-based one, achieving less than half of its MR cost. It's also generally better when considering the mean square error, while also presenting the least settling time among the three designs. Finally, it manages to accomplish this with $\|S_i\|_\infty = 1.42$, which is the second-lowest obtained with the three designs. Alternatively, the results for the voltage loop indicate very similar results between VRFT and the MB-MR design, which present lower quadratic and model-reference costs than the frequency-domain approach, as well as lower peaks of the estimated sensitivity function. Moreover, the settling times for steps in the voltage reference are also significantly shorter. On the other hand, the response to resistive load steps is worse with VRFT and the MB-MR design, since the model-reference approach tends to cancel the subsystem's poles. As such, the performance is degraded when there is a disturbance in them, and thus the frequency-domain design ends up performing better, with a lower settling time and a lower quadratic cost.

Finally, it's noticeable that the controller's zero in the VRFT solution (5.5) is very close to the unit circle, which indicates that the sampling frequency for this control loop may be too high. Because of this, Appendix A illustrates that, by downsampling the data before applying VRFT, it's possible to obtain a controller with a similar gain, but with a zero further away from the unit circle. Moreover, the MR performance is qualitatively very similar to the case without downsampling, indicating that there are no problems with the sampling frequency.

In short, the proposed design manages to achieve the best performance in the current loop and is able to perform very similarly against the corresponding MB-MR design for the voltage loop. Since it's a model reference approach, it ends up performing worse in load steps scenarios than the MB-freq methodology.

Table 3 – Performance comparison between data-driven and model-based designs.

Characteristic	VRFT	MB - MR	MB - freq.
$\|\|S\|\|_\infty$ - int. loop	1.42	1.58	1.37
Cost $\hat{J}_{i,\text{MR}}$	254 mA^2	612 mA^2	-
Cost $\hat{J}^{\text{ref}}_{i,r}$	0.006 A^2	0.007 A^2	0.009 A^2
Time $t^{\text{ref}}_{s,2\%,i}$	556 us	879 us	995 us
$\|\|S\|\|_\infty$ - ext. loop	1.27	1.27	1.40
Cost $\hat{J}_{e,\text{MR}}$	0.05 V^2	0.02 V^2	-
Cost $\hat{J}^{\text{ref}}_{e,r}$	6.47 V^2	6.35 V^2	7.00 V^2
Cost $\hat{J}^{\text{dist}}_{e,r}$	17.35 V^2	19.11 V^2	7.08 V^2
Time $t^{\text{ref}}_{s,2\%,e}$	0.0417 s	0.0499 s	0.1153 s
Time $t^{\text{dist}}_{s,2\%,e}$	0.0803 s	0.0862 s	0.0335 s

Source: the author (2025).

5.2 VRFT WITH NOISY CURRENT DATA

In this section the performance of VRFT against additive gaussian white noise added to the measurement of the current in the data-collection is studied. The analysis is focused on the current controller, since it's the loop where VRFT application is different from the DC-DC converters case, as the current doesn't follow a DC nominal trajectory, but instead a sinusoidal one. Besides, it's the loop with the higher bandwidth, as such analog filters can't be designed with lower cut-off frequencies, and thus noise problems tend to happen more frequently.

With the goal of observing the influence of noise in the current controller calculated by VRFT, 25 instances of data for 10 different noise levels are collected. The noise is parametrized in relation to its variance, starting from $7.47{\cdot}10^{-4}$ A^2 going in fixed equal intervals up to $7.47{\cdot}10^{-3}$ A^2, or equivalently, from an SNR of approximately 30 dB to 20 dB, considering the current signal power. The lower noise level is equivalent to the noise observed in the experimental prototype discussed in the next chapter. It's worth remarking that these SNR magnitudes are in relationship to the total power of the sinusoidal current waveform, however the SNR associated with the variation data for VRFT is much smaller, as it can be noticed from the confidence intervals of Figure 26. In fact, the actual SNR used in the input data for VRFT goes from 14 dB to 4 dB, resulting in poor performance of the algorithm as the noise power increases.

In the noiseless case, the obtained gain vector associated with the internal current controller of (5.3) is $\rho_i = \begin{bmatrix} 0.0876 & 0.0065 \end{bmatrix}^T$. To illustrate the importance of using four sets

Figure 26 – Noisy current data with 68% confidence intervals.

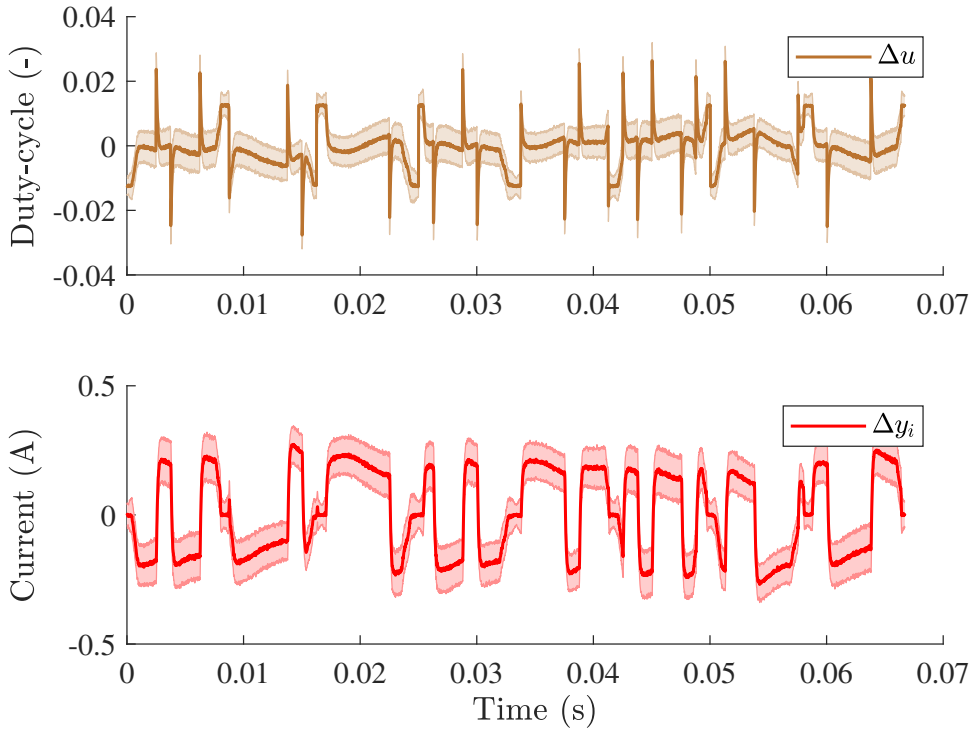

Source: the author (2025).

of data in the procedure summarized by Section 4.5, first VRFT is applied when collecting only one set of nominal signals $\{u_i^*(k), y_i^*(k)\}_{k=1}^N$; and calculating the trajectory variation set $\{\Delta u_i(k), \Delta y_i(k)\}_{k=1}^N$ by subtracting the two excited sets and the common nominal one. When this is done with noise added to the current measurements, several gains corresponding to the box plots of Figure 27a are obtained, showing that, as the noise level increases, there is a clear alteration in the expected values for the two current gains ρ_{i1} and ρ_{i2}. In other words, the use of a common nominal set of data makes the VRFT solution biased, which raises the error between the expected calculated gains and the desired one found in the noiseless case. Furthermore, Figure 28 shows the percentage of stabilizing current controllers in this case, where it's noticeable that VRFT returns controllers which aren't stabilizing after the noise variance reaches a certain threshold, even reaching the point of returning zero stabilizing controllers with the highest simulated noise variance.

On the other hand, when four sets of data are used, i.e. two sets of nominal signals and two sets of excited ones, the gains' distributions of Figure 27b are obtained, showing that the expected VRFT output remains around the same point, which is very close to the noiseless case. Indeed, the effects of the noise just seem to affect the variance of each box plot, which is an expected result of using the instrumental variable solution for VRFT. Furthermore, every controller throughout each noise level is stabilizing.

Figure 27 – Bias effect on current controller gains ρ_i.

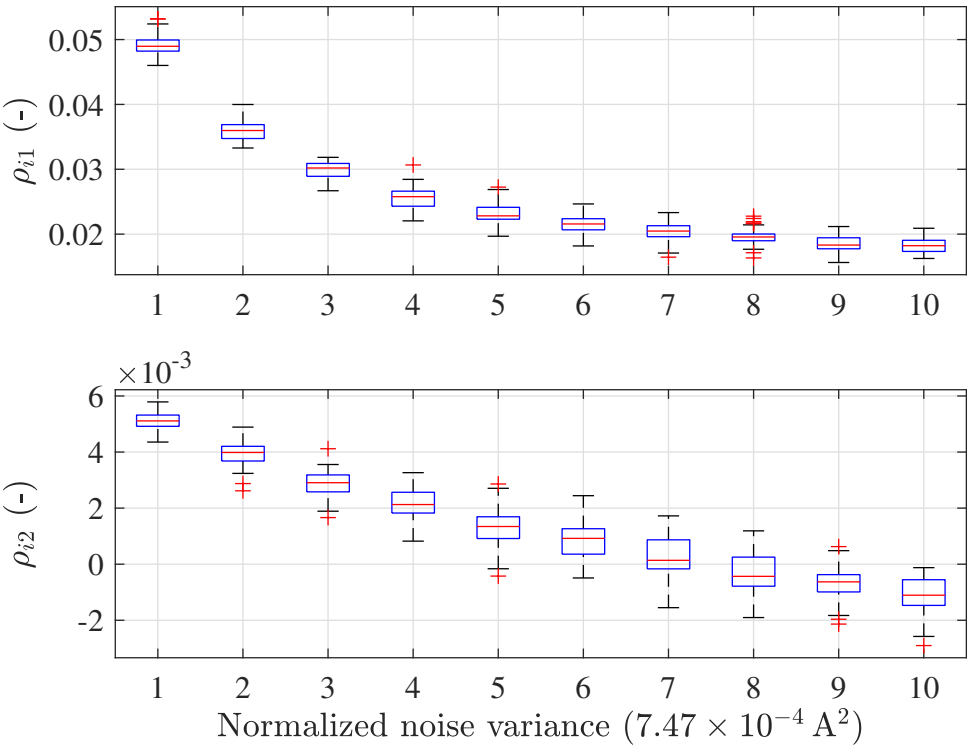

(a) Box plots when three sets of data are used.

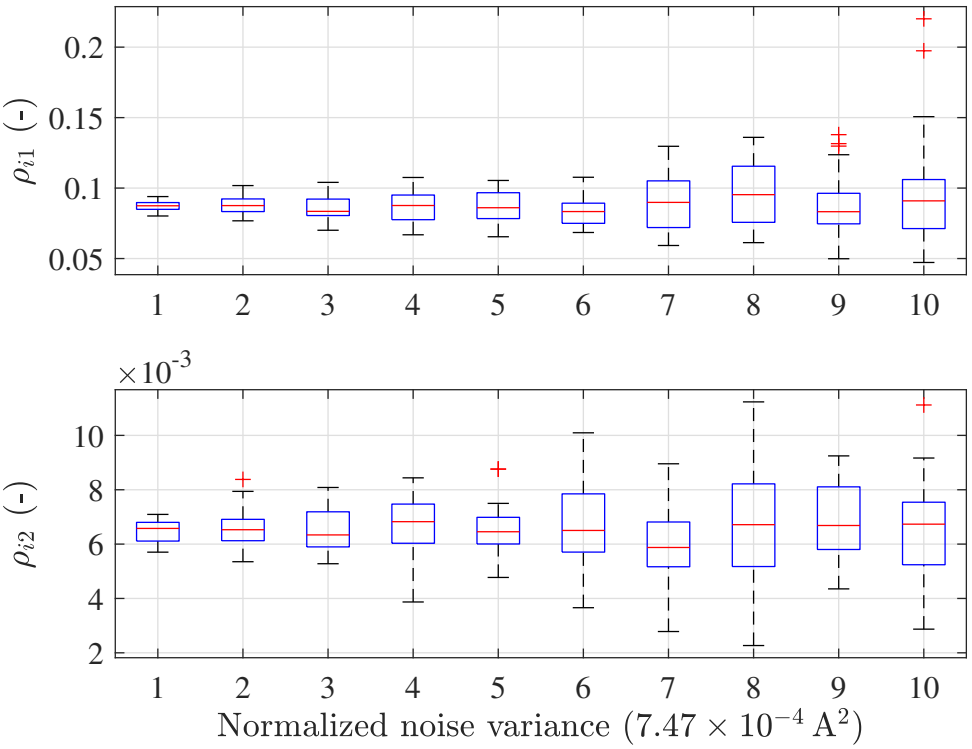

(b) Box plots when four sets of data are used.

Source: the author (2025).

Figure 28 – Percentage of stabilizing current controllers when three sets of data are used.

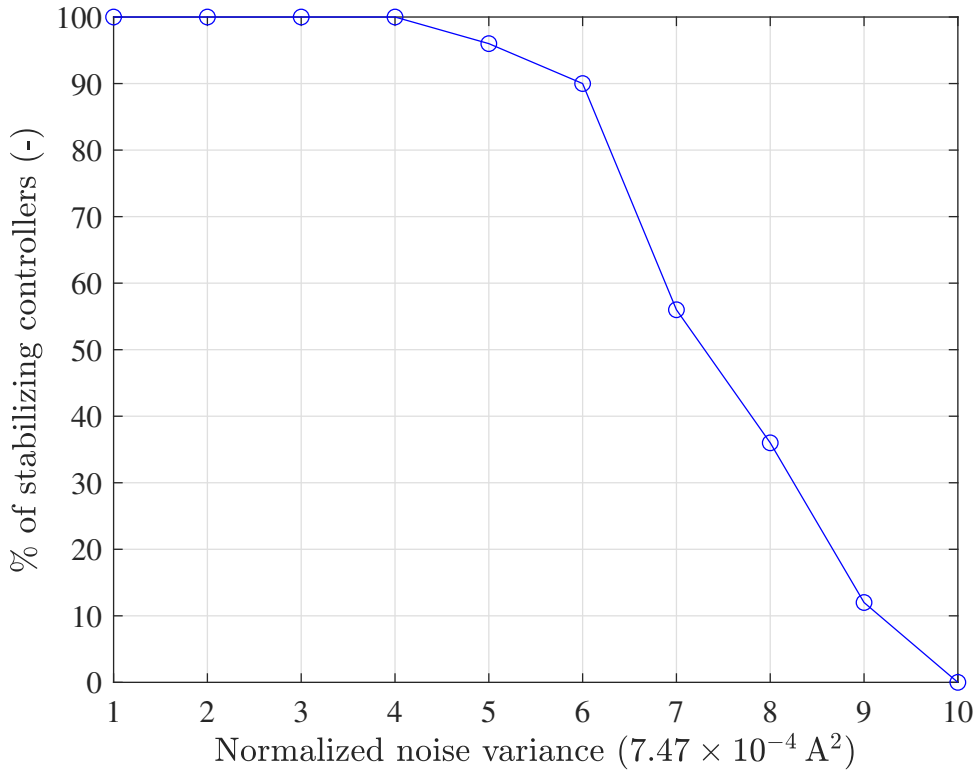

Source: the author (2025).

5.3 FINAL CONSIDERATIONS

This chapter has illustrated how to apply the proposed method in a noiseless simulation example. It was confirmed that a good MR performance is attainable with just input-output data for both subsystems, specially the current loop. In addition, a comparison with a model-based design shows that the data-driven one presents a lower MR cost. Furthermore, the outer voltage loop presents the lowest peak of the estimated sensitivity function, hinting that the design for the worst-case operating point does in fact work. Finally, several simulations with different noise levels in the current measurements reveal that the expected controller gains vary around the same value, being independent of the noise variance. In other words, no bias in the resulting controller gains is observed, verifying that the IV solution for VRFT using the 4 sets of data is functioning adequately.

6 EXPERIMENTAL RESULTS

This chapter presents an application of the proposed DDC technique to a boost PFC rectifier prototype. Experimental results are then acquired and illustrate the effectiveness of the proposed method.

6.1 EXPERIMENTAL SETUP

A prototype for a bridgeless totem-pole boost rectifier was built to validate the proposed data-driven design method. The converter's specifications are also listed in Table 2, and the design is based of the work from Fischer, Rech, and Novaes (2020). A picture of the prototype is found in Figure 29, where two IGBTs in antiparallel with two Silicon Carbide diodes are used for the fast switching components in the power stage. The current measurement is done through a hall effect current sensor, whereas the voltage from the output is obtained through a resistor divider. All the relevant measurements go through analog conditioning circuits before they are read by the Microcontroller Unit's (MCU) Analog-to-Digital Converters. In addition, in order to avoid disparities between the expected discretized models (3.15) and (3.21), the board's input filter was removed so that the model-based projects wouldn't be exceedingly penalized by ignored dynamics.

A development board hosting a TMS320F28379D MCU is utilized to conduct the data-collection experiment, as well as controlling the converter and executing other routines to ensure safe operation. To generate the current reference, a moving average PLL algorithm (Golestan; Guerrero; Vasquez, 2017; Golestan et al., 2014) is utilized, following the same control diagram from Figure 8. Furthermore, a digital low-pass filter is used to reduce the noise influence in the voltage measurements, which is already incorporated in the measurement block H_{vo} in Figure 8.

Similarly to the simulation study case, the input voltage comes from a variable autotransformer yielding a maximum rms voltage of 264 V, which is then considered the maximum input voltage used in the data-collection experiments. During the tests the converter is set to feed a resistor bank load measuring 746 Ω, corresponding to a minimum load power of 194 W. The tests are set to this minimum power because it's the worst-case operating point regarding gain and phase margins, as discussed in Section 4.4.

Figure 29 – Boost rectifier prototype.

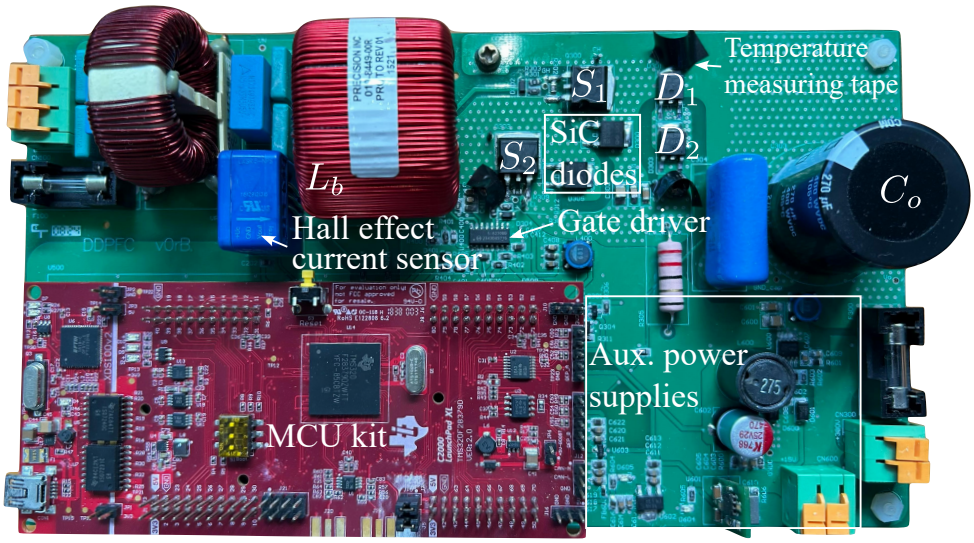

Source: the author (2025).

6.2 CONTROLLER DESIGN

First, the experiment to design the inner current controller is conducted. In the same way as the simulation study case, the parameters for driving the converter correspond to: $D_{\max} = 0.9$ and $D_{ff,\max} = 0.85$, $\Delta r_{iL} = 0.2\,\text{A}$ and $k_p = 0.125/2$. The PRBS frequency is also set to 800 Hz.

Given the above, the required two sets of nominal and excited trajectories are collected. Due to the memory limits of the MCU, a total of $N = 10800$ samples for each dataset is captured, i.e., the system is excited over the span of 10 line cycles. Already taking the difference between the trajectories, the signals of Figure 30 are obtained, which illustrates only 4320 samples for visual clarity.

Then, the same reference model (5.2) can be selected to design the PI current controller. Therefore, using this model and the data of Figure 30 in the VRFT algorithm results in the controller

$$C_i(z,\rho_i) = 0.11753 \cdot \frac{z-0.9003}{z-1}. \tag{6.1}$$

Next, in order to conduct the external experiment, a variation of $\Delta u_e(k) = 0.2\,\text{A}$ is selected. The PRBS frequency is set to 50 Hz. In sequence, again the two sets of nominal and excited trajectories are collected, yielding 4 sets of data with $N = 10800$ samples each. The input experimental data for VRFT is shown in Figure 31. Applying these signals and the reference model of (5.4) on the VRFT algorithm results in the controller

$$C_e(z,\rho_e) = 0.02857 \cdot \frac{z-0.9999}{z-1}. \tag{6.2}$$

Figure 30 – Internal experiment signals for VRFT.

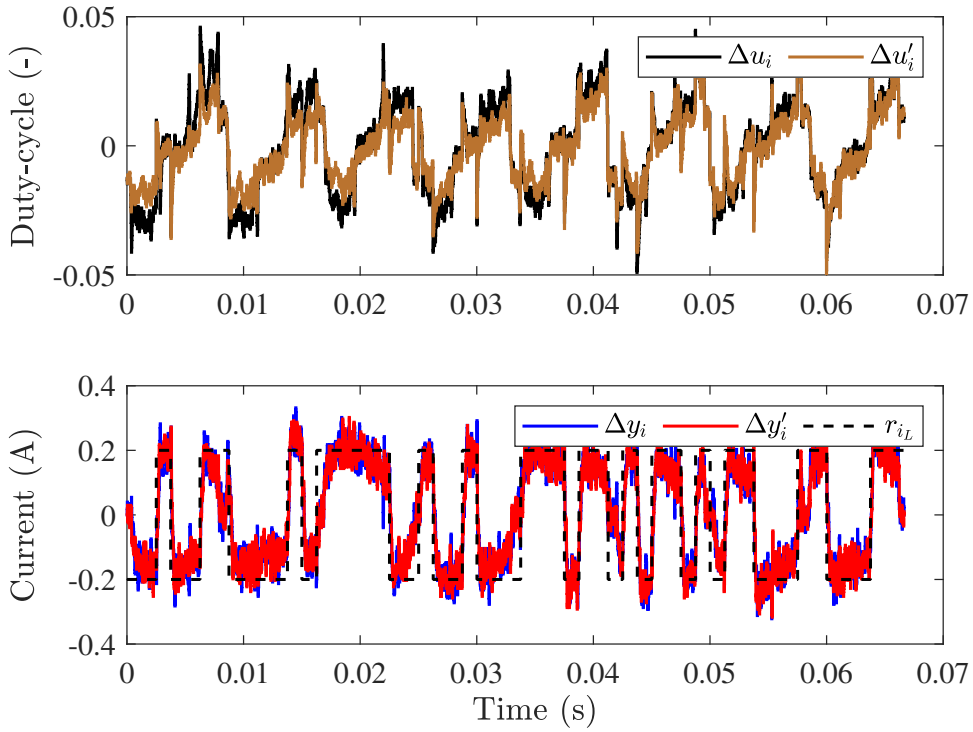

Source: the author (2025).

Figure 31 – External experiment signals for VRFT.

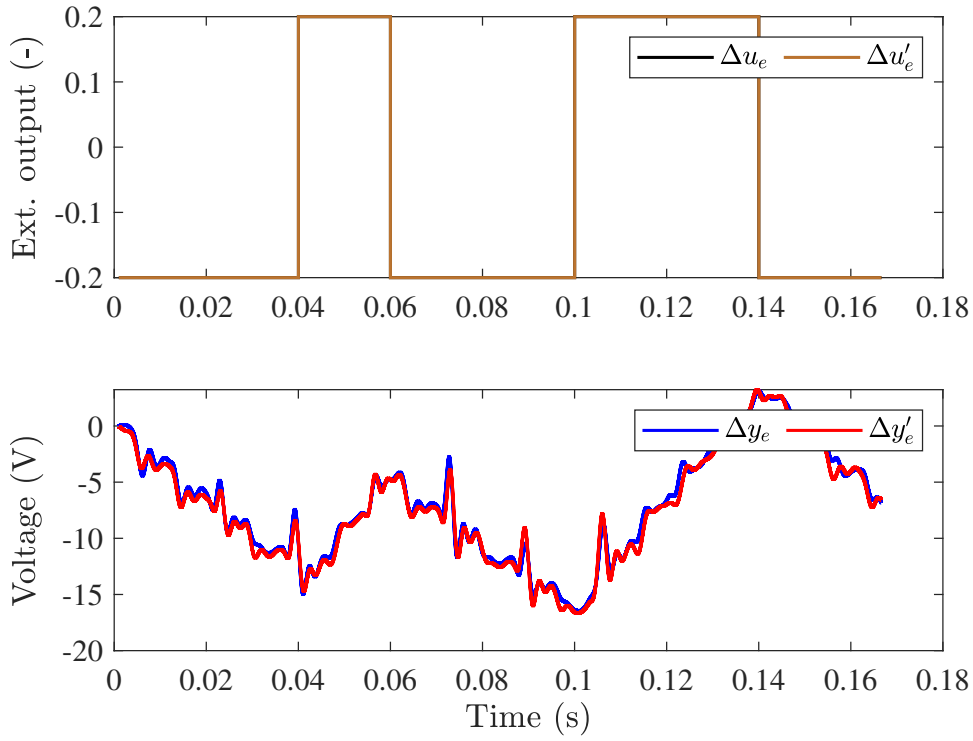

Source: the author (2025).

Both controllers are similar to the ones obtained in the noiseless simulation study case, i.e., (5.3) and (5.5), with the advantage of incorporating parameter deviations and model uncertainty

in the design process through the use of data.

6.3 CLOSED-LOOP RESULTS

Next an analysis of the model reference and quadratic costs of the obtained VRFT controllers and the same model-based ones of (5.6) – (5.9) is carried out. To this end, the same excitation signal used in the data-collection experiments is applied in the reference of both control loops, enabling the observation of the variation around the resulting trajectories. These results also correspond to the operating point $V_{in,rms} = 264\,\text{V}$ and $P_o = 194\,\text{W}$. The estimation of the peak of the sensitivity functions is also done as in Section 5.1.

First, Figure 32 shows the signals collected by the oscilloscope during operation with the minimum allowed output power for the VRFT controllers. It can be seen that the both the output voltage and input current are regulated around the desired trajectories. Moreover, Figure 33 shows the harmonics of $i_{in}(t)$ and the limits of IEC 61000-3-2 considering the nominal power of 300 W. It's clear then that, even when operating with lower power the DDC design manages to control the current to acceptable levels considering the standard.

Figure 32 – Closed-loop operation of the converter with $V_{in,rms} = 264\,\text{V}$ and $P_o = 194\,\text{W}$.

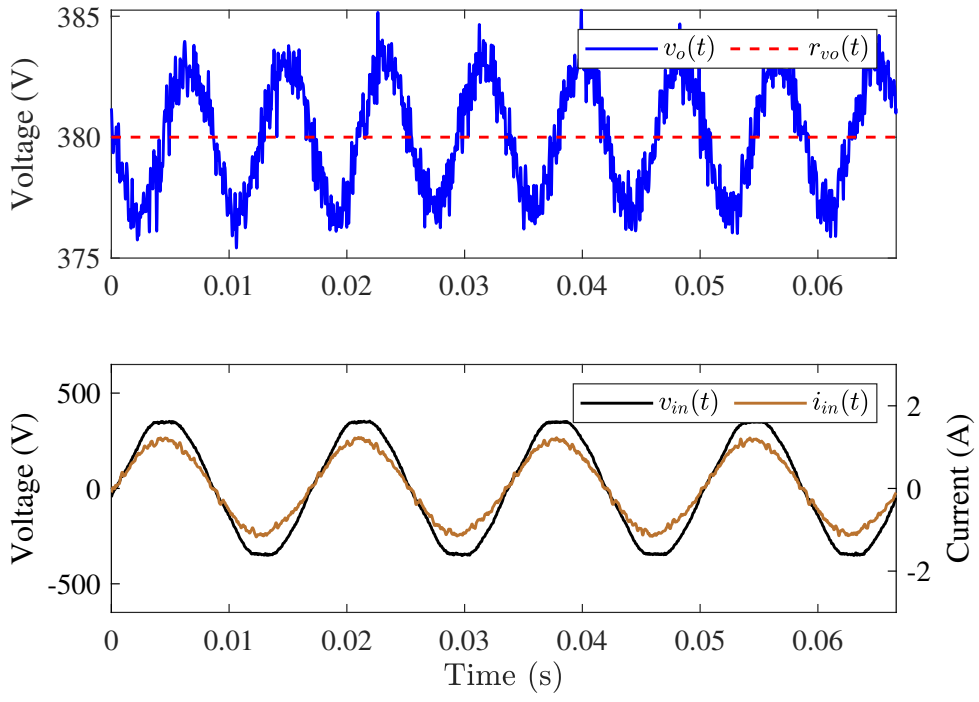

Source: the author (2025).

In order to analyze the MR performance, initially considering the current loop, the closed-loop experiment was repeated 10 times to cope with the noise, such that mean current and duty-cycle trajectories for each controller were calculated. These signals are then utilized to determine the performance metrics of Table 4 and are shown in Figure 34. Although all the controllers show a similar response, it's clear that VRFT in this case yields the response with the

Figure 33 – Harmonics of the input current with $P_o = 194\,\text{W}$ and limits of IEC 61000-3-2 (Class D).

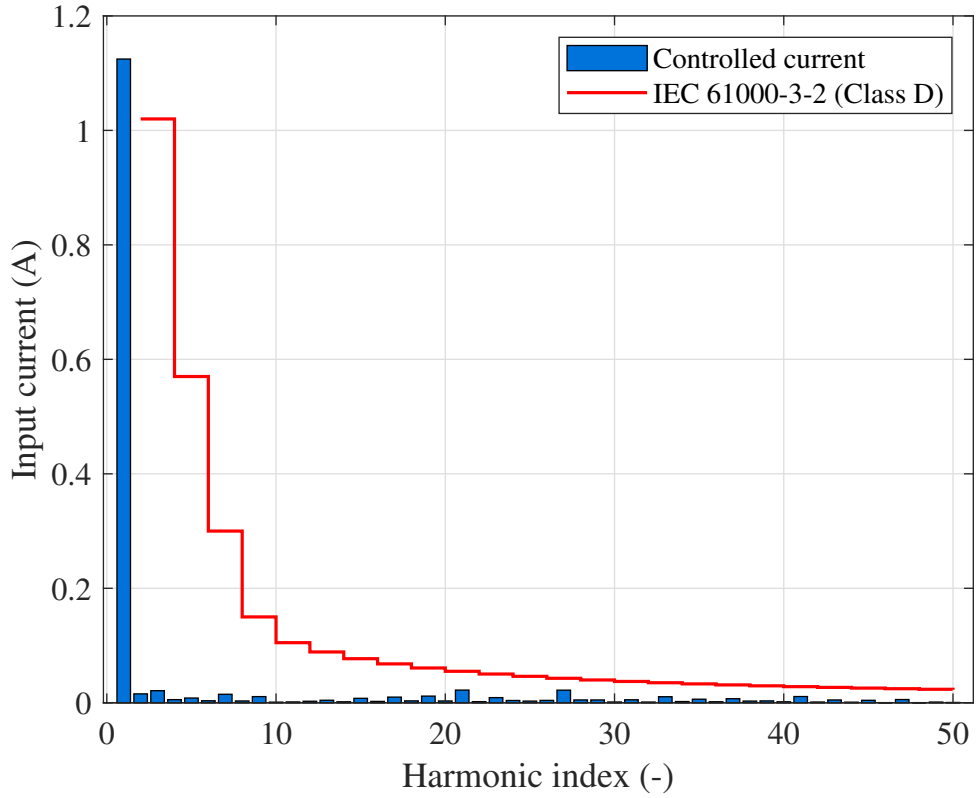

Source: the author (2025).

least settling time and lowest costs, which also resembles the most the desired trajectory $\Delta i_{L,d}$. Furthermore, the estimated $\|S_i\|_\infty$ indicates that it's also the most robust controller.

Table 4 – Performance comparison between data-driven and model-based designs.

Characteristic	VRFT	MB - MR	MB - freq.
PF	0.9953	0.9924	0.9940
$\|S_i\|_\infty$	1.20	1.45	1.22
Cost $\hat{J}_{i,\text{MR}}$	0.00121 A^2	0.00272 A^2	-
Cost $\hat{J}_{i,r}^{\text{ref}}$	0.00712 A^2	0.00993 A^2	0.0101 A^2
Time $t_{s,5\%,i}^{\text{ref}}$	1.05 ms	1.14 ms	1.51 ms
$\|S_e\|_\infty$	1.26	1.29	1.53
Cost $\hat{J}_{e,\text{MR}}$	0.1644 V^2	0.1874 V^2	-
Cost $\hat{J}_{e,r}^{\text{ref}}$	4.98 V^2	3.86 V^2	5.20 V^2
Time $t_{s,2\%,e}^{\text{ref}}$	0.0514 s	0.0534 s	0.0746 s

Source: the author (2025).

Additionally, considering the voltage loop, Figure 35 shows the obtained responses of a single experiment when a PRBS signal of 5 V and 50 Hz is added to the voltage reference. Due to a memory limitation of the MCU, the sampled output voltage signals were re-sampled at a

Figure 34 – Experimental MR performance for the current loop.

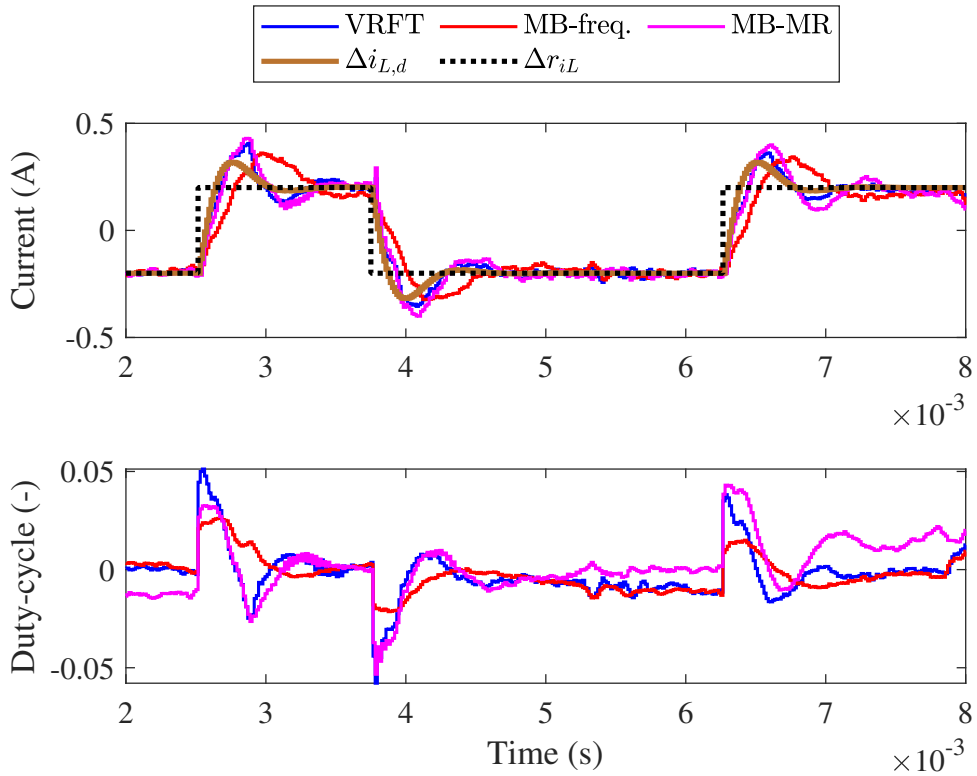

Source: the author (2025).

frequency 5 times lower than the switching frequency, and linear interpolation was applied in the post-processing to reconstruct them. All the output voltage signals in this case present a ripple in the harmonics the line frequency (60 Hz), which is visible in the sampled signals. In order to facilitate the determination of the settling times, a moving average filter was employed to remove this noise, however this filter is not utilized to calculate MR and quadratic costs. With that, the worst design method in this case is the MB-freq, yielding the least robust and slowest response. Notably, VRFT and MB-MR perform very similarly, with the former resulting in the lowest MR cost and the latter in the lowest quadratic cost. This suggests that the uncertainty in the prototype favored a faster but more aggressive response in the MB-MR design over the VRFT design. Indeed, the estimated $\|S_e\|_\infty$ for both controllers indicate that VRFT is slightly more robust than the remaining methods, demonstrating the effectiveness of the proposed design procedure for the worst-case operating region.

Finally, the power factor was also estimated using the saved oscilloscope data, showing that all three design methods manage to yield a power factor close to unity, with a small advantage as well for VRFT. Altogether, VRFT manages to outperform the model-based design methods in practically every metric, validating the proposed data-driven design method. Some oscilloscope screenshot samples are presented in Appendix B.

Figure 35 – Experimental MR performance for the voltage loop.

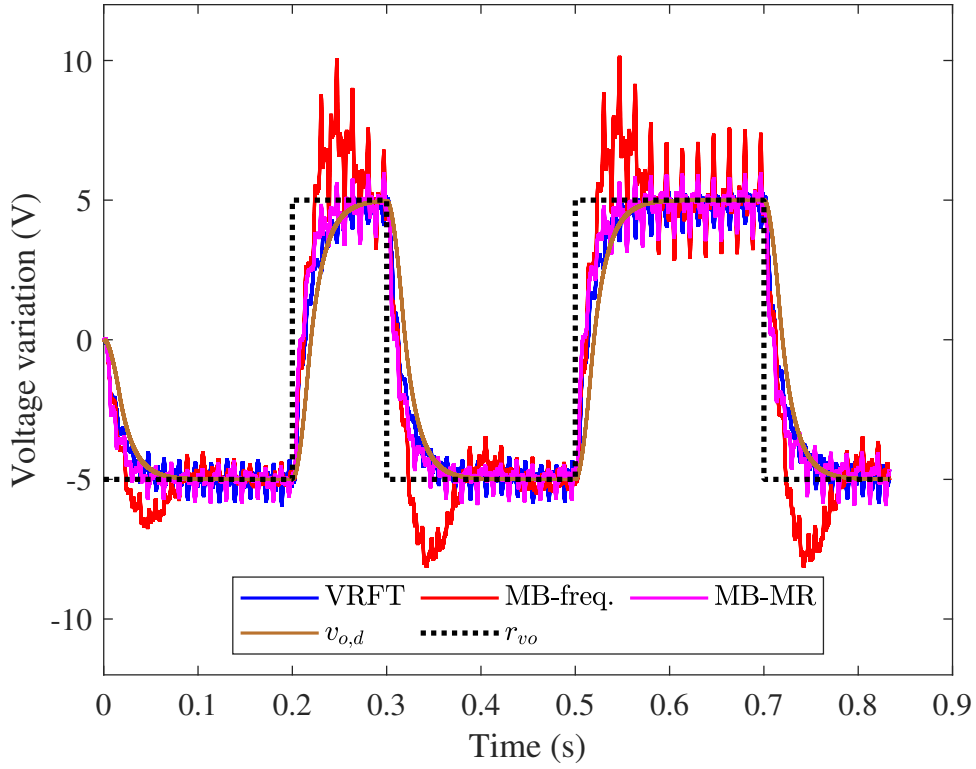

Source: the author (2025).

6.4 FINAL CONSIDERATIONS

This chapter has validated the proposed DDC method to derive the two controllers required to drive a boost PFC rectifier prototype. The low error between the desired responses and the obtained current and voltage signals indicates the effectiveness of the proposed DDC technique over manual tuning of model-based ones.

7 CONCLUSION

To advance the state-of-the-art DDC techniques to a more complete position in terms of use case, the topic of data-driven control in the context of designing the cascade controllers of a totem-pole boost bridgeless rectifier has been explored, where the VRFT technique is adapted to this particular application. Although results are particularized towards this specific topology, they can easily be generalized for any converter belonging to the boost PFC family of rectifiers, which consist of a good middle-ground between the fundamental DC-DC topologies and more complex converters with strong nonlinearities.

In Chapter 2, a literature review of DDC techniques in the context of power electronics is presented. Among many reviewed methods, it is noticeable that VRFT has some distinct qualities, specially the simplicity in its formulation and the fact that it's a one-shot technique. Unfortunately, considering the proposed design procedure of this master's thesis, this last quality is traded off in order to deal with the multiplier nonlinearity in the control path. Nonetheless, the mathematical framework around this technique further motivates the choice to use it to design PFC controllers. In that regard, Chapter 3 has presented some basic PFC concepts and reviewed the totem-pole boost bridgeless rectifier, which is the chosen converter to validate the proposed method experimentally.

The main results of this work are gathered in Chapter 4, which elaborates on the designer choices around VRFT in order to design two controllers in a cascade structure. First, the PI controller class is recommended for both control loops, as it attends the requisite of loop shaping towards a target bandwidth, as well as a low and null steady-state error for the current and voltage loops respectively. Regarding the reference models, suitable transfer-functions forms are presented for both loops, which considerate the structure of the processes' models. Moreover, a method of collecting data with two separate experiments is presented, which uses the variation of signals around its nominal trajectories to collect suitable data for VRFT. This is specially important for the current loop, since both the current and duty-cycle signals present large variations and don't vary around a single DC level.

In order to illustrate the proposed technique, Chapter 5 contains simulations results, first presented in a noiseless scenario, where it was possible to design two controllers and drive a totem-pole boost bridgeless rectifier to a passing performance regarding the IEC 61000-3-2 standard. Furthermore, the VRFT qualities of returning non-biased controllers are also verified through a study where several simulations with gaussian white noise added to the current measurements are used to design multiple controllers. Indeed, it is noticeable that the corresponding distribution of gains varies around the same mean value as noise power increases, showing that there is no bias in the VRFT estimation. Accordingly, the experimental results of Chapter 6 further reinforce the conclusions taken from the simulations. Actually, due to the intrinsic uncertainties of the built experimental prototype, VRFT manages to perform better than

other model-based techniques, validating the proposed DDC method for PFC rectifiers.

Finally, the main contributions of this master's thesis can be summarized as follows:

1. The proposal of a DDC technique to design cascade controllers for boost PFC rectifiers;
2. Guidelines for choosing achievable closed-loop reference models and for how to conduct the data-collection experiments to ensure stability over variations of the input voltage and resistive load;
3. Example case studies in simulation and with a built 300W prototype to achieve a passing performance in regard to EMC standards.

Regarding future works, it's suggested to:

1. Expand the method considering operation in the discontinuous conduction when low power is demanded. A nonlinear control law of gain scheduling or a switching algorithm can be proposed to change between the two modes;
2. Validate the method for higher bandwidths in the external loop by utilizing a notch or moving average filter in the output voltage readings;
3. Compare VRFT with some recent formulations based on the behavioral theory;
4. Expand the proposed method in order to require only one data-collection experiment;
5. Adapt the proposed method to use the proportional-resonant controller class and obtain null steady-state error in the current loop.

REFERENCES

ASADI, Yasin et al. Data-Driven Model-Free Adaptive Control of Z-Source Inverters. en. **Sensors**, Multidisciplinary Digital Publishing Institute, v. 21, n. 22, p. 7438, Jan. 2021. ISSN 1424-8220. DOI: 10.3390/s21227438. Available from: <https://www.mdpi.com/1424-8220/21/22/7438>. Visited on: 16 Apr. 2024. Cit. on pp. 21, 25.

BAZANELLA, Alexandre Sanfelice; CAMPESTRINI, Lucíola; ECKHARD, Diego. **Data-Driven Controller Design: The H2 Approach**. [S.l.]: Springer Science & Business Media, Nov. 2011. ISBN 9789400723009. Cit. on pp. 16, 18, 20, 21, 26–30, 42, 48.

BAZANELLA, Alexandre Sanfelice; CAMPESTRINI, Lucíola; ECKHARD, Diego. The data-driven approach to classical control theory. **Annual Reviews in Control**, v. 56, p. 100906, Jan. 2023. ISSN 1367-5788. DOI: 10.1016/j.arcontrol.2023.100906. Available from: <https://www.sciencedirect.com/science/article/pii/S1367578823000706>. Visited on: 15 Apr. 2024. Cit. on pp. 19, 20.

BEAL, Guilherme de Paoli et al. Harmonic Rejection on UPS through Cascade VRFT of Proportional-Resonant Controller. In: 2023 IEEE Conference on Control Technology and Applications (CCTA). [S.l.: s.n.], Aug. 2023. P. 1083–1088. ISSN: 2768-0770. DOI: 10.1109/CCTA54093.2023.10252391. Available from: <https://ieeexplore.ieee.org/document/10252391>. Visited on: 8 Apr. 2024. Cit. on pp. 19, 21, 22.

BELKAMEL, Hamza; KIM, Hyungjin; CHOI, Sewan. Interleaved totem-pole ZVS converter operating in CCM for single-stage bidirectional AC–DC conversion with high-frequency isolation. **IEEE Transactions on Power Electronics**, IEEE, v. 36, n. 3, p. 3486–3495, 2020. Cit. on pp. 29–31, 41.

BOYD, Stephen et al. **Linear Matrix Inequalities in System and Control Theory**. [S.l.]: Society for Industrial and Applied Mathematics, Jan. 1994. (Studies in Applied and Numerical Mathematics). ISBN 9780898714852. DOI: 10.1137/1.9781611970777. Available from: <https://epubs.siam.org/doi/book/10.1137/1.9781611970777>. Visited on: 5 July 2024. Cit. on p. 18.

CASTRO, Ignacio et al. A Review on Flicker-Free AC–DC LED Drivers for Single-Phase and Three-Phase AC Power Grids. **IEEE Transactions on Power Electronics**, v. 34, n. 10, p. 10035–10057, Oct. 2019. ISSN 1941-0107. DOI: 10.1109/TPEL.2018.2890716. Available from: <https://ieeexplore.ieee.org/document/8598951>. Visited on: 7 May 2024. Cit. on p. 16.

CHEN, Peng et al. A Review on the Applications of Reinforcement Learning Control for Power Electronic Converters. In: 2023 IEEE International Conference on Energy Technologies for Future Grids (ETFG). [S.l.: s.n.], Dec. 2023. P. 1–6. DOI: 10.1109/ETFG55873.2023.10408685.

Available from: <https://ieeexplore-ieee-org.ez74.periodicos.capes.gov.br/document/10408685>. Visited on: 15 Apr. 2024. Cit. on p. 19.

CHENG, Chun-An et al. Design and Implementation of a Single-Stage Driver for Supplying an LED Street-Lighting Module With Power Factor Corrections. **IEEE Transactions on Power Electronics**, v. 30, n. 2, p. 956–966, 2015. DOI: 10.1109/TPEL.2014.2312024. Cit. on p. 17.

CORLETA, André et al. Data-driven control design applied to uninterruptible power supplies. In: 2016 IEEE Conference on Control Applications (CCA). [S.l.: s.n.], Sept. 2016. P. 1312–1317. DOI: 10.1109/CCA.2016.7587988. Available from: <https://ieeexplore.ieee.org/document/7587988>. Visited on: 6 Nov. 2024. Cit. on p. 29.

DÖRFLER, Florian. Data-Driven Control: Part One of Two: A Special Issue Sampling from a Vast and Dynamic Landscape. **IEEE Control Systems Magazine**, v. 43, n. 5, p. 24–27, Oct. 2023. ISSN 1941-000X. DOI: 10.1109/MCS.2023.3291624. Available from: <https://ieeexplore.ieee.org/document/10266821>. Visited on: 8 Apr. 2024. Cit. on p. 18.

DÖRFLER, Florian. Data-Driven Control: Part Two of Two: Hot Take: Why not go with Models? **IEEE Control Systems Magazine**, v. 43, n. 6, p. 27–31, Dec. 2023. ISSN 1941-000X. DOI: 10.1109/MCS.2023.3310302. Available from: <https://ieeexplore.ieee.org/document/10317633>. Visited on: 8 Apr. 2024. Cit. on p. 18.

ERICKSON, Robert W.; MAKSIMOVIC, Dragan. **Fundamentals of Power Electronics**. 3rd. Cham: Springer, Aug. 2020. ISBN 9783030438791. Cit. on pp. 17, 29, 30, 32, 35, 38, 41, 42, 48, 50.

FIORIO, L. V. et al. Virtual reference feedback tuning with robustness constraints: A swarm intelligence solution. **Engineering Applications of Artificial Intelligence 123 (2023) 106490**, Elsevier BV, v. 123, p. 106490, 3 Nov. 2021. DOI: 10.1016/j.engappai.2023.106490. arXiv: 2111.02212 [eess.SY]. Cit. on pp. 21, 31, 43, 50.

FISCHER, Guilherme da Silva; RECH, Cassiano; NOVAES, Yales Rômulo de. Extensions of Leading-Edge Modulated One-Cycle Control for Totem-Pole Bridgeless Rectifiers. **IEEE Transactions on Power Electronics**, v. 35, n. 5, p. 5447–5460, May 2020. ISSN 1941-0107. DOI: 10.1109/TPEL.2019.2946570. Available from: <https://ieeexplore.ieee.org/abstract/document/8863991>. Visited on: 18 June 2024. Cit. on pp. 33, 67.

FRIEDLI, Thomas; HARTMANN, Michael; KOLAR, Johann W. The Essence of Three-Phase PFC Rectifier Systems—Part II. **IEEE Transactions on Power Electronics**, v. 29, n. 2, p. 543–560, Feb. 2014. ISSN 1941-0107. DOI: 10.1109/TPEL.2013.2258472. Available from: <https://ieeexplore.ieee.org/abstract/document/6502727>. Visited on: 21 May 2024. Cit. on p. 16.

GEYER, Tobias. **Model Predictive Control of High Power Converters and Industrial Drives**. 1st edition. [S.l.]: Wiley, Sept. 2016. Cit. on p. 25.

GOLESTAN, Saeed; GUERRERO, Josep M.; VASQUEZ, Juan C. Single-Phase PLLs: A Review of Recent Advances. **IEEE Transactions on Power Electronics**, v. 32, n. 12, p. 9013–9030, Dec. 2017. ISSN 1941-0107. DOI: 10.1109/TPEL.2017.2653861. Available from: <https://ieeexplore.ieee.org/document/7819538>. Visited on: 22 June 2024. Cit. on pp. 36, 37, 67.

GOLESTAN, Saeed et al. Moving Average Filter Based Phase-Locked Loops: Performance Analysis and Design Guidelines. **IEEE Transactions on Power Electronics**, v. 29, n. 6, p. 2750–2763, June 2014. ISSN 1941-0107. DOI: 10.1109/TPEL.2013.2273461. Available from: <https://ieeexplore.ieee.org/document/6560420>. Visited on: 22 June 2024. Cit. on pp. 36, 37, 67.

HOU, Zhong-Sheng; WANG, Zhuo. From model-based control to data-driven control: Survey, classification and perspective. **Information Sciences**, v. 235, p. 3–35, June 2013. ISSN 0020-0255. DOI: 10.1016/j.ins.2012.07.014. Available from: <https://www.sciencedirect.com/science/article/pii/S0020025512004781>. Visited on: 15 Apr. 2024. Cit. on pp. 19, 25.

HOU, Zhongsheng; CHI, Ronghu; GAO, Huijun. An Overview of Dynamic-Linearization-Based Data-Driven Control and Applications. **IEEE Transactions on Industrial Electronics**, v. 64, n. 5, p. 4076–4090, May 2017. ISSN 1557-9948. DOI: 10.1109/TIE.2016.2636126. Available from: <https://ieeexplore.ieee.org/document/7775006>. Visited on: 15 Apr. 2024. Cit. on pp. 19, 24.

HOU, Zhongsheng; JIN, Shangtai. Model Free Adaptive Control: Theory and Applications. en. In. ISBN 9780429165474. DOI: 10.1201/b15752. Available from: <https://www.taylorfrancis.com/books/9781466594197>. Visited on: 5 July 2024. Cit. on p. 25.

HUANG, Linbin et al. Robust Data-Enabled Predictive Control: Tractable Formulations and Performance Guarantees. **IEEE Transactions on Automatic Control**, v. 68, n. 5, p. 3163–3170, May 2023. ISSN 1558-2523. DOI: 10.1109/TAC.2023.3241282. Available from: <https://ieeexplore.ieee.org/document/10034855>. Visited on: 16 Apr. 2024. Cit. on pp. 21, 25.

HUANG, Qingyun; HUANG, Alex Q. Review of GaN totem-pole bridgeless PFC. **CPSS Transactions on Power Electronics and Applications**, v. 2, n. 3, p. 187–196, Sept. 2017. ISSN 2475-742X. DOI: 10.24295/CPSSTPEA.2017.00018. Available from: <https://ieeexplore.ieee.org/document/8118374>. Visited on: 7 May 2024. Cit. on pp. 17, 33.

HUBER, Laszlo; JANG, Yungtaek; JOVANOVIC, Milan M. Performance Evaluation of Bridgeless PFC Boost Rectifiers. **IEEE Transactions on Power Electronics**, v. 23, n. 3, p. 1381–1390, 2008. DOI: 10.1109/TPEL.2008.921107. Cit. on p. 33.

IEC. **Electromagnetic compatibility (EMC)- Part 3-2: Limits- Limits for harmonic current emissions (equipment input current <=16 A per phase)**. Geneva, Switzerland: [s.n.], 2018. Standard. Cit. on pp. 32, 58.

KALAIR, A. et al. Review of harmonic analysis, modeling and mitigation techniques. **Renewable and Sustainable Energy Reviews**, Elsevier, v. 78, p. 1152–1187, 2017. Cit. on p. 33.

KAMEYA, Naoki et al. VRFT for Current-Mode Buck Converter with Anti-Windup Compensation. In: 2022 IEEE Energy Conversion Congress and Exposition (ECCE). [S.l.: s.n.], Oct. 2022. P. 1–7. ISSN: 2329-3748. DOI: 10.1109/ECCE50734.2022.9948174. Available from: <https://ieeexplore.ieee.org/document/9948174>. Visited on: 15 Apr. 2024. Cit. on pp. 16, 21, 22.

KAZIMIERCZUK, Marian K. **Pulse-Width Modulated DC-DC Power Converters**. 2nd edition. [S.l.]: Wiley, Aug. 2015. Cit. on pp. 16, 58.

KHALIL, H.K. **Nonlinear Systems**. [S.l.]: Prentice Hall, 2002. (Pearson Education). ISBN 9780130673893. Cit. on p. 30.

KUPAS, Erick. **Método de Controle baseado em dados para a Síntese de controladores proporcionais-ressonantes aplicado a inversores monofásicos**. 2022. Trabalho de conclusão de curso (Graduação em Engenharia Elétrica) – Udesc. Available from: <https://repositorio.udesc.br/entities/publication/c3f9da60-18b3-4385-a618-2db992d7d20e>. Visited on: 5 Dec. 2025. Cit. on p. 43.

LI, Haoran et al. A 300-kHz 6.6-kW SiC Bidirectional LLC Onboard Charger. **IEEE Transactions on Industrial Electronics**, v. 67, n. 2, p. 1435–1445, 2020. DOI: 10.1109/TIE.2019.2910048. Cit. on p. 16.

LI, Haoran et al. A 300-kHz 6.6-kW SiC bidirectional LLC onboard charger. **IEEE Transactions on Industrial Electronics**, IEEE, v. 67, n. 2, p. 1435–1445, 2019. Cit. on pp. 29–31.

LJUNG, L. **System Identification: Theory for the User**. [S.l.]: Prentice Hall PTR, 1999. (Prentice Hall information and system sciences series). ISBN 9780136566953. Cit. on p. 55.

MANSOURI, Mahdi et al. A review of single phase power factor correction A.C.-D.C. converters. In: 2013 IEEE Conference on Clean Energy and Technology (CEAT). [S.l.: s.n.], 2013. P. 389–394. DOI: 10.1109/CEAT.2013.6775662. Cit. on p. 33.

MARKOVSKY, Ivan; HUANG, Linbin; DÖRFLER, Florian. Data-Driven Control Based on the Behavioral Approach: From Theory to Applications in Power Systems. **IEEE Control Systems Magazine**, v. 43, n. 5, p. 28–68, Oct. 2023. ISSN 1941-000X. DOI: 10.1109/MCS.2023.3291638. Available from: <https://ieeexplore.ieee.org/document/10266847>. Visited on: 8 Apr. 2024. Cit. on pp. 16, 18.

MATLAB. **impulseest: Nonparametric impulse response estimation**. United States of America: [s.n.], 2020. Cit. on p. 60.

MATLAB. **System identification toolbox**. United States of America: [s.n.], 2021. Cit. on p. 60.

MOHAMED, Ihab S. et al. A Neural-Network-Based Model Predictive Control of Three-Phase Inverter With an Output LC Filter. **IEEE Access**, v. 7, p. 124737–124749, 2019. ISSN 2169-3536. DOI: 10.1109/ACCESS.2019.2938220. Available from: <https://ieeexplore.ieee.org/document/8819887>. Visited on: 16 Apr. 2024. Cit. on p. 25.

ORUGANTI, Ramesh; SRINIVASAN, Ramesh. Single phase power factor correction — A review. **Sadhana**, v. 22, n. 6, p. 753–780, 1997. ISSN 0973-7677. DOI: 10.1007/BF02745844. Available from: <https://doi.org/10.1007/BF02745844>. Cit. on pp. 32, 33.

PANDEY, Rahul; SINGH, Bhim. A power-factor-corrected LLC resonant converter for electric vehicle charger using Cuk converter. **IEEE Transactions on Industry Applications**, IEEE, v. 55, n. 6, p. 6278–6286, 2019. Cit. on pp. 29–31, 41.

PEREIRA, Dênis de C. et al. Improved and accurate low-frequency average modelling and control of a conventional power factor correction boost converter in continuous conduction mode. **IET Power Electronics**, v. 14, n. 2, p. 373–385, 2021. DOI: https://doi.org/10.1049/pel2.12039. eprint: https://ietresearch.onlinelibrary.wiley.com/doi/pdf/10.1049/pel2.12039. Available from: <https://ietresearch.onlinelibrary.wiley.com/doi/abs/10.1049/pel2.12039>. Cit. on p. 50.

PERSIS, Claudio de; TESI, Pietro. Formulas for Data-Driven Control: Stabilization, Optimality, and Robustness. **IEEE Transactions on Automatic Control**, v. 65, n. 3, p. 909–924, Mar. 2020. ISSN 1558-2523. DOI: 10.1109/TAC.2019.2959924. Available from: <https://ieeexplore.ieee.org/document/8933093>. Visited on: 17 Apr. 2024. Cit. on p. 23.

PRAG, Krupa; WOOLWAY, Matthew; CELIK, Turgay. Toward Data-Driven Optimal Control: A Systematic Review of the Landscape. **IEEE Access**, v. 10, p. 32190–32212, 2022. ISSN 2169-3536. DOI: 10.1109/ACCESS.2022.3160709. Available from: <https://ieeexplore.ieee.org/document/9738649>. Visited on: 8 Apr. 2024. Cit. on pp. 18–20.

QIE, Tianhao et al. A Novel Data-Driven Large Signal Stabilizer for Interleaved DC/DC Boost Converter With Constant Power Load. **IEEE Transactions on Industrial Electronics**, p. 1–10, 2024. ISSN 1557-9948. DOI: 10.1109/TIE.2024.3370957. Available from: <https://ieeexplore.ieee.org/document/10473757>. Visited on: 15 Apr. 2024. Cit. on pp. 16, 21, 23.

QIN, Shibin et al. A High-Power-Density Power Factor Correction Front End Based on Seven-Level Flying Capacitor Multilevel Converter. **IEEE Journal of Emerging and Selected Topics in Power Electronics**, v. 7, n. 3, p. 1883–1898, 2019. DOI: 10.1109/JESTPE.2018.2865597. Cit. on p. 33.

QIN, Shibin et al. A high-power-density power factor correction front end based on seven-level flying capacitor multilevel converter. **IEEE Journal of Emerging and Selected Topics in Power Electronics**, IEEE, v. 7, n. 3, p. 1883–1898, 2018. Cit. on pp. 29–31.

RAFI, Md Ahsanul Hoque; BAUMAN, Jennifer. A Comprehensive Review of DC Fast-Charging Stations With Energy Storage: Architectures, Power Converters, and Analysis. **IEEE Transactions on Transportation Electrification**, v. 7, n. 2, p. 345–368, 2021. DOI: 10.1109/TTE.2020.3015743. Cit. on p. 33.

RECHT, Benjamin. A Tour of Reinforcement Learning: The View from Continuous Control. en. **Annual Review of Control, Robotics, and Autonomous Systems**, Annual Reviews, v. 2, Volume 2, 2019, p. 253–279, May 2019. ISSN 2573-5144. DOI: 10.1146/annurev-control-053018-023825. Available from: <https://www.annualreviews.org/content/journals/10.1146/annurev-control-053018-023825>. Visited on: 8 Apr. 2024. Cit. on pp. 16, 18.

REMES, C. L. et al. Virtual reference feedback tuning applied to cascade control. en. **IET Control Theory & Applications**, v. 14, n. 20, p. 3738–3746, 2020. ISSN 1751-8652. DOI: 10.1049/iet-cta.2020.0620. Available from: <https://onlinelibrary.wiley.com/doi/abs/10.1049/iet-cta.2020.0620>. Visited on: 8 Apr. 2024. Cit. on pp. 20–22, 29, 30, 42.

REMES, C. L. et al. Virtual Reference Feedback Tuning Applied to DC–DC Converters. **IEEE Transactions on Industrial Electronics**, v. 68, n. 1, p. 544–552, Jan. 2021. ISSN 1557-9948. DOI: 10.1109/TIE.2020.2967729. Available from: <https://ieeexplore.ieee.org/document/8967239>. Visited on: 21 Nov. 2023. Cit. on pp. 19, 21, 28–31, 42, 44, 45.

RODRIGUEZ, Jose; CORTES, Patricio. **Predictive Control of Power Converters and Electrical Drives**. 1st edition. [S.l.]: Wiley-IEEE Press, Apr. 2012. Cit. on p. 25.

RUIZ-MARTINEZ, O. F. et al. Data-driven stabilizing control of DC–DC converters with unknown active loads. **Control Engineering Practice**, v. 95, p. 104266, Feb. 2020. ISSN 0967-0661. DOI: 10.1016/j.conengprac.2019.104266. Available from: <https://www.sciencedirect.com/science/article/pii/S0967066119302163>. Visited on: 9 Apr. 2024. Cit. on pp. 16, 21, 23.

SAYED, Sawsan S.; MASSOUD, Ahmed M. Review on State-of-the-Art Unidirectional Non-Isolated Power Factor Correction Converters for Short-/Long-Distance Electric Vehicles. **IEEE Access**, v. 10, p. 11308–11340, 2022. DOI: 10.1109/ACCESS.2022.3146410. Cit. on p. 33.

SCHRITTWIESER, Lukas et al. 99.3% efficient three-phase buck-type all-SiC SWISS rectifier for DC distribution systems. **IEEE Transactions on Power Electronics**, IEEE, v. 34, n. 1, p. 126–140, 2018. Cit. on pp. 29–31.

SILVA, Gustavo R. Gonçalves da et al. Data-Driven LQR Control Design. **IEEE Control Systems Letters**, v. 3, n. 1, p. 180–185, Jan. 2019. ISSN 2475-1456. DOI: 10.1109/LCSYS.2018.2868183. Available from: <https://ieeexplore.ieee.org/document/8453019>. Visited on: 8 Apr. 2024. Cit. on pp. 18, 20–22.

SKOGESTAD, Sigurd; POSTLETHWAITE, Ian. **Multivariable Feedback Control: Analysis and Design**. 2nd ed. Chichester: John Wiley & Sons, Nov. 2005. Cit. on pp. 16, 29, 31, 43, 50, 58.

VAN WAARDE, Henk J. et al. The Informativity Approach: To Data-Driven Analysis and Control. **IEEE Control Systems Magazine**, v. 43, n. 6, p. 32–66, Dec. 2023. ISSN 1941-000X. DOI: 10.1109/MCS.2023.3310305. Available from: <https://ieeexplore.ieee.org/document/10317631>. Visited on: 17 Apr. 2024. Cit. on pp. 22–24.

WANG, Minlin; REN, Xuemei; CHEN, Qiang. Cascade Optimal Control for Tracking and Synchronization of a Multimotor Driving System. **IEEE Transactions on Control Systems Technology**, v. 27, n. 3, p. 1376–1384, May 2019. ISSN 1558-0865. DOI: 10.1109/TCST.2018.2810273. Available from: <https://ieeexplore.ieee.org/document/8323381>. Visited on: 6 Nov. 2024. Cit. on p. 29.

WANG, Zhengyao et al. Model-free adaptive control for ultracapacitor based three-phase interleaved bidirectional DC–DC converter. en. **IET Power Electronics**, v. 16, n. 16, p. 2696–2707, 2023. ISSN 1755-4543. DOI: 10.1049/pel2.12594. Available from: <https://onlinelibrary.wiley.com/doi/abs/10.1049/pel2.12594>. Visited on: 16 Apr. 2024. Cit. on pp. 21, 24.

WEI, Zi-Jie et al. Data-Driven Tracking Control Design With Noisy Data and its Application in DC Microgrid Control. **IEEE Transactions on Power Electronics**, v. 40, n. 12, p. 17776–17788, 2025. DOI: 10.1109/TPEL.2025.3595863. Cit. on pp. 21, 24.

WILLEMS, Jan C. et al. A note on persistency of excitation. **Systems & Control Letters**, v. 54, n. 4, p. 325–329, Apr. 2005. ISSN 0167-6911. DOI: 10.1016/j.sysconle.2004.09.003. Available from: <https://www.sciencedirect.com/science/article/pii/S0167691104001434>. Visited on: 17 Apr. 2024. Cit. on p. 23.

YIN, Shen et al. Data-Based Techniques Focused on Modern Industry: An Overview. **IEEE Transactions on Industrial Electronics**, v. 62, n. 1, p. 657–667, Jan. 2015. ISSN 1557-9948. DOI: 10.1109/TIE.2014.2308133. Available from: <https://ieeexplore.ieee.org/document/6748057>. Visited on: 15 Apr. 2024. Cit. on p. 19.

ZHANG, Huaguang et al. Data-Driven Control for Interlinked AC/DC Microgrids Via Model-Free Adaptive Control and Dual-Droop Control. **IEEE Transactions on Smart Grid**, v. 8, n. 2, p. 557–571, Mar. 2017. ISSN 1949-3061. DOI: 10.1109/TSG.2015.2500269. Available from: <https://ieeexplore.ieee.org/document/7348696>. Visited on: 16 Apr. 2024. Cit. on pp. 21, 24.

APPENDIX A – VRFT WITH A DOWNSAMPLED EXTERNAL LOOP

Since, often, the switching frequency is much higher than the desired bandwidth for the external control loop, it may be desirable to implement it with a downsampled controller while keeping the internal current loop's sampling frequency equal to the switching one. An example of this is presented in this section, to illustrate that the proposed method also works in this case.

In other words, it's proposed to downsample the input error signal e_v in Figure 8 by a factor of M, so as the external controller coefficients are better numerically conditioned, i.e. further spaced from each other. The external controller's output signal u_v is upsampled by a zero order hold, such that it can be interfaced with the internal current loop.

Regarding modifications on the proposed method, two additional steps must be made considering that the input-output data from the external data-collection experiment is available. First, it's required that the input dataset for VRFT $\{\Delta u_e(k), \Delta y_e(k)\}_{k=1}^{N}$ is downsampled by M. Second, the normalized bandwidth must also be recalculated to correspond with the new sampling frequency f_s/M. It's remarked that the external data-collection experiment may be realized in the same way as before.

To illustrate that these steps are sufficient, the data of Figure 19 is used. In this example, an arbitrary downsample factor $M = 60$ is considered. Considering the desired bandwidth f_{be} of 10 Hz, it's necessary to determine the new normalized bandwidth Ω_{be} through the relation $\Omega_{be} = M \cdot f_{be}/(0.5 \cdot f_s) = 0.0185$. From the graph of Figure 12, this corresponds to a new pole of $p_{e1} = 0.94$, which results in the following reference model

$$T_{de}(z) = \frac{0.06}{z - 0.94}. \tag{A.1}$$

Applying VRFT with the downsampled data of Figure 19 results in the adapted controller

$$C_e(z, \rho_e) = 0.034612 \cdot \frac{z - 0.9906}{z - 1}. \tag{A.2}$$

It's worth remarking that, because of the lower sampling frequency, the controller's zero is much further from the unit circle than the one in (5.5). The MR qualitative performance for this downsampled controller is shown in Figure 36, where it's clear that the closed loop response of the system resembles the desired signal very closely.

Figure 36 – Simulated MR performance for the voltage loop when downsampled by a factor of 60

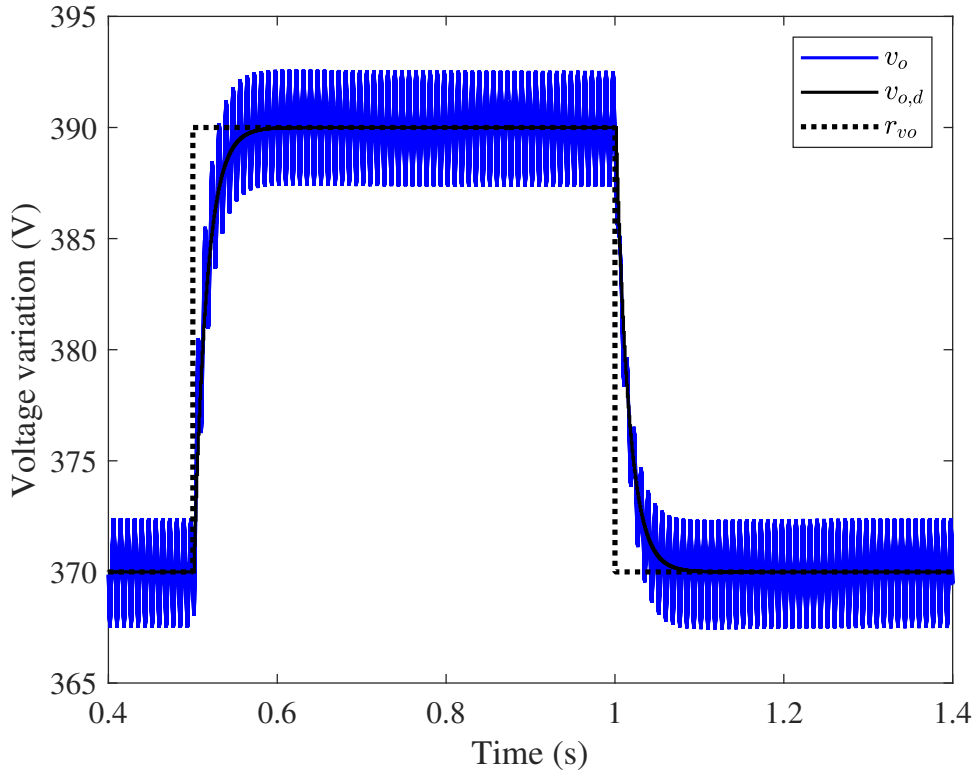

Source: the author (2025).

APPENDIX B – EXPERIMENTAL SETUP AND OSCILLOSCOPE SCREEN SAMPLES

A photo of the setup is presented in Figure 37. In addition, some relevant screenshots from the oscilloscope used in the experimental validation are shown below.

Figure 37 – Photo of the experimental setup.

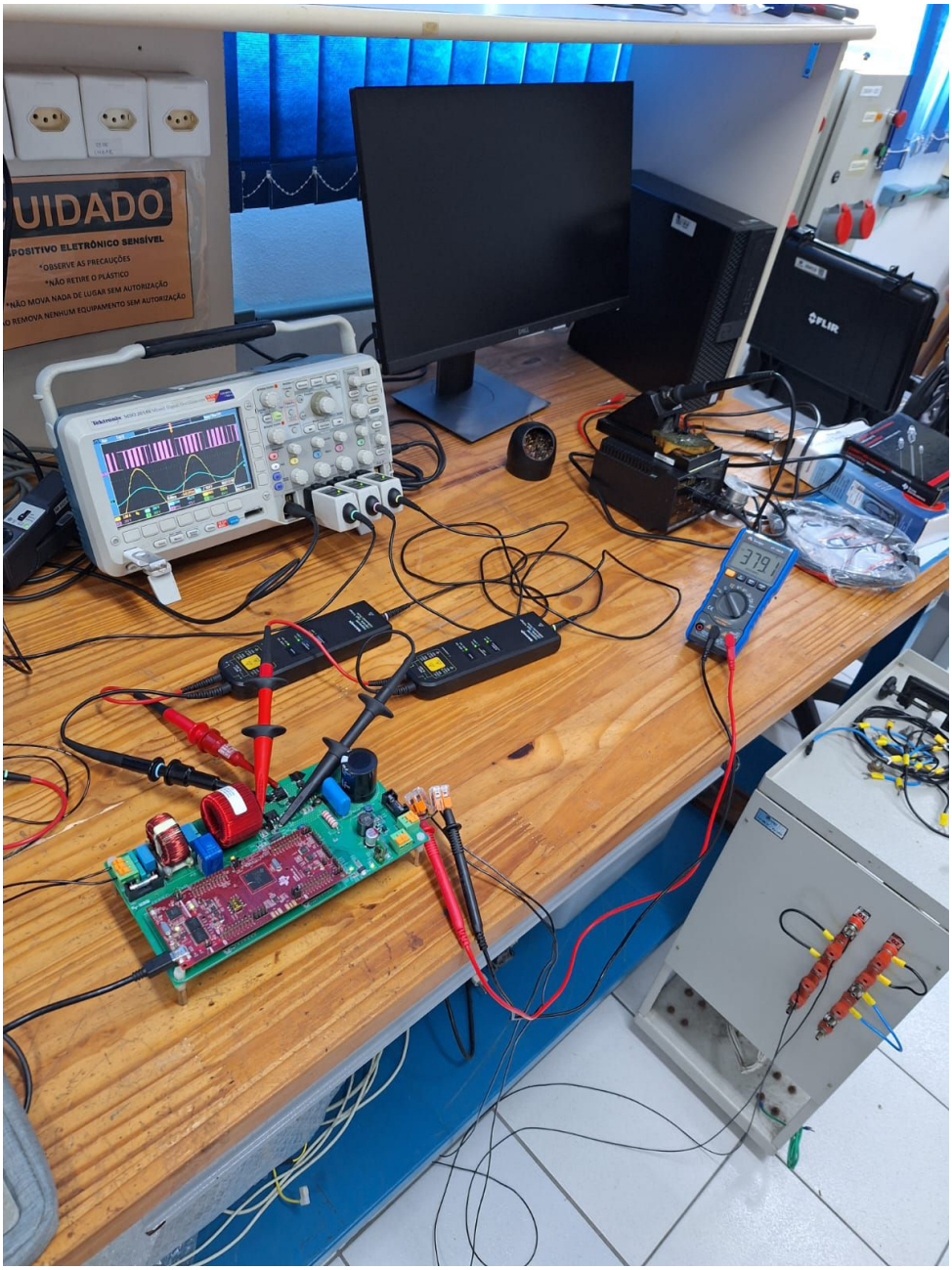

Source: the author (2025).

Figure 38 – PFC operation with MB-freq controllers.

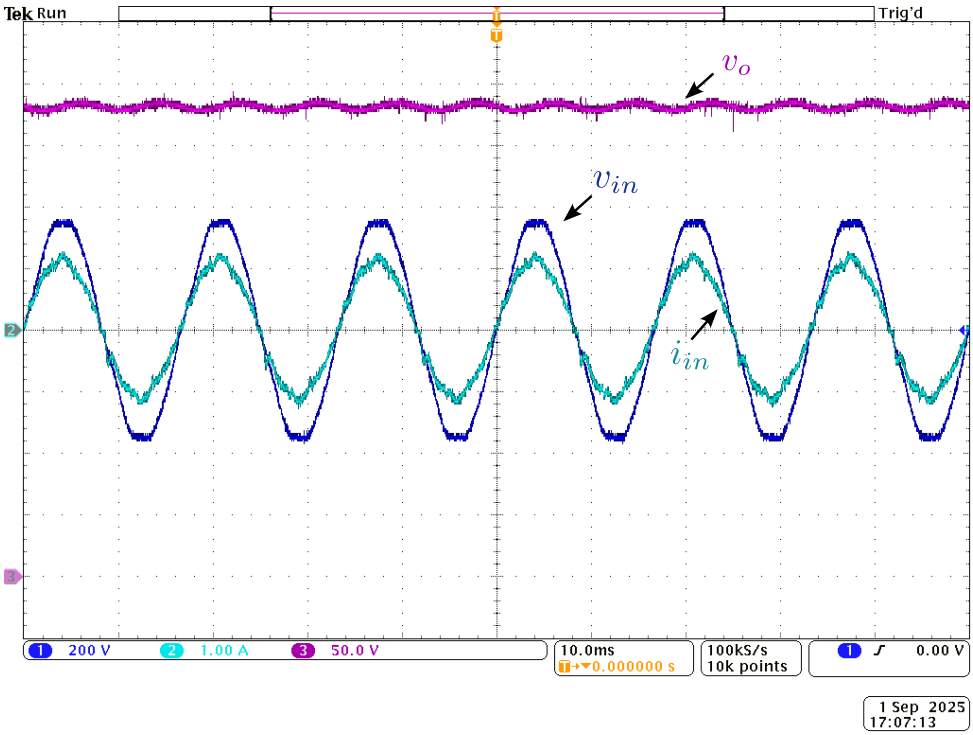

Source: the author (2025).

Figure 39 – PFC operation with MB-MR controllers.

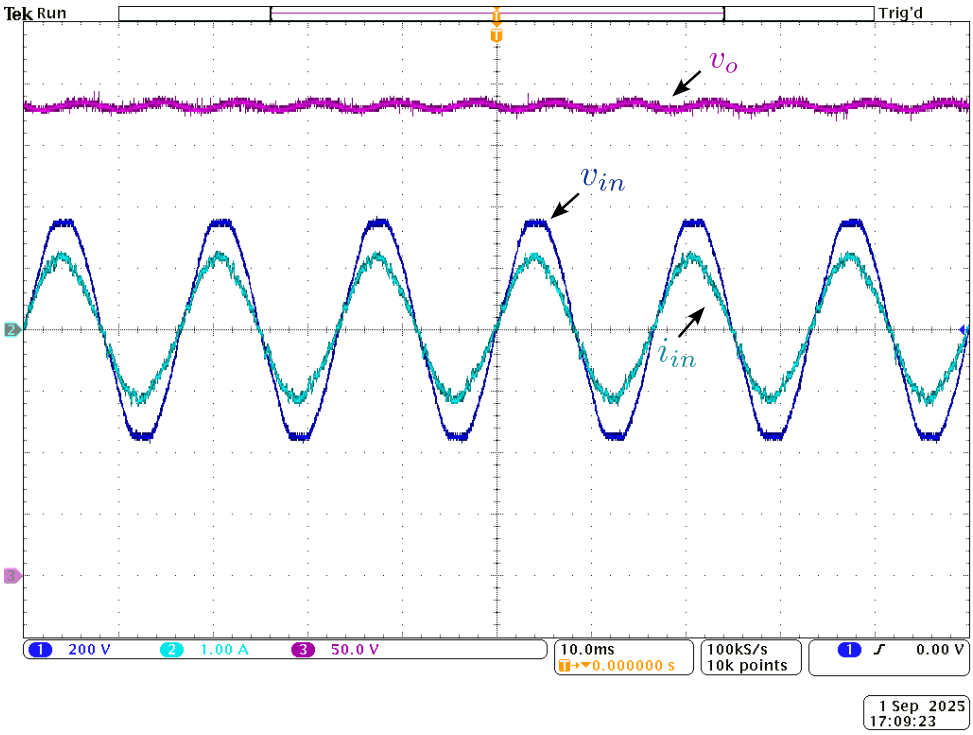

Source: the author (2025).

Figure 40 – PFC operation with VRFT controllers.

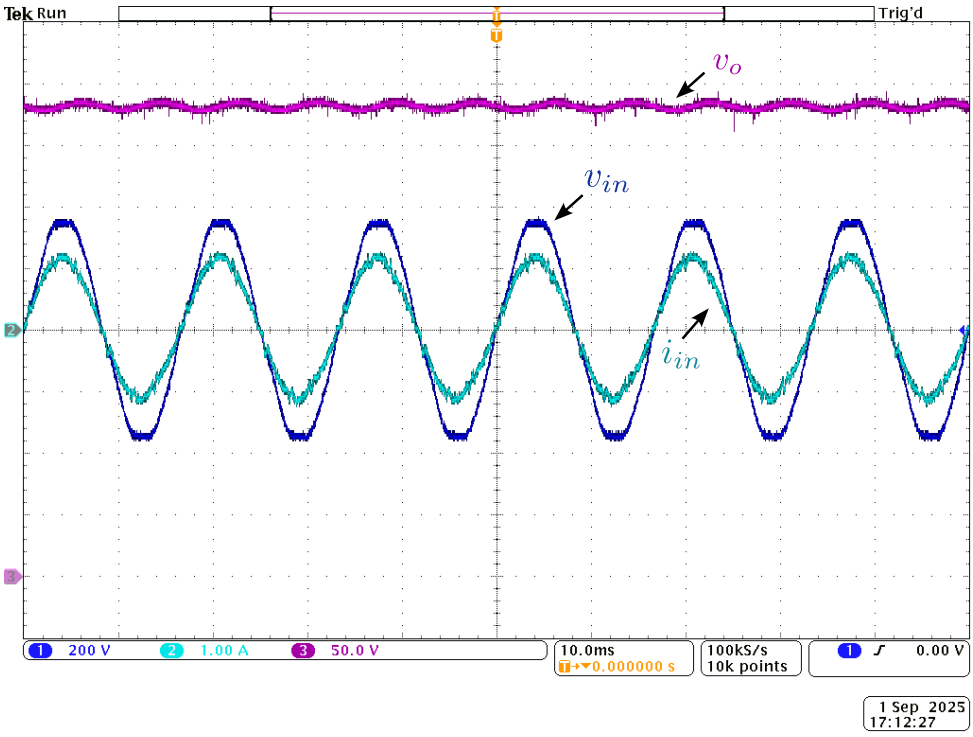

Source: the author (2025).

UDESC UNIVERSIDADE DO ESTADO DE SANTA CATARINA | JOINVILLE CENTRO DE CIÊNCIAS TECNOLÓGICAS

UNIVERSIDADE DO ESTADO DE SANTA CATARINA – UDESC
BIBLIOTECA UNIVERSITÁRIA
REPOSITÓRIO INSTITUCIONAL

CENTRO DE CIÊNCIAS TECNOLÓGICAS – CCT

ATESTADO DE VERSÃO FINAL

Eu, Yales Rômulo de Novaes, professor do curso de Mestrado Acadêmico em Engenharia Elétrica, declaro que esta é a versão final aprovada pela comissão julgadora da dissertação/tese intitulada: **"Data-Driven Control Applied to Single-Phase High Power Factor Boost Rectifiers"** de autoria do acadêmico Rafael Juliano Scholtz.

Joinville, 19 de dezembro de 2025.

Assinatura digital do orientador:

gov.br Documento assinado digitalmente
YALES ROMULO DE NOVAES
Data: 19/12/2025 12:00:25-0300
Verifique em https://validar.iti.gov.br

_____ _____

Yales Rômulo de Novaes